

INFORMATION TO USERS

This manuscript has been reproduced from the microfilm master. UMI films the text directly from the original or copy submitted. Thus, some thesis and dissertation copies are in typewriter face, while others may be from any type of computer printer.

The quality of this reproduction is dependent upon the quality of the copy submitted. Broken or indistinct print, colored or poor quality illustrations and photographs, print bleedthrough, substandard margins, and improper alignment can adversely affect reproduction.

In the unlikely event that the author did not send UMI a complete manuscript and there are missing pages, these will be noted. Also, if unauthorized copyright material had to be removed, a note will indicate the deletion.

Oversize materials (e.g., maps, drawings, charts) are reproduced by sectioning the original, beginning at the upper left-hand corner and continuing from left to right in equal sections with small overlaps. Each original is also photographed in one exposure and is included in reduced form at the back of the book.

Photographs included in the original manuscript have been reproduced xerographically in this copy. Higher quality 6" x 9" black and white photographic prints are available for any photographs or illustrations appearing in this copy for an additional charge. Contact UMI directly to order.

UMI

A Bell & Howell Information Company
300 North Zeeb Road, Ann Arbor MI 48106-1346 USA
313/761-4700 800/521-0600

NUCLEATION AND GROWTH OF AlGaP ON SILICON
BY METAL-ORGANIC MOLECULAR BEAM EPITAXY

BY

CHRISTOPHER JOSEPH SANTANA

A DISSERTATION PRESENTED TO THE GRADUATE SCHOOL
OF THE UNIVERSITY OF FLORIDA IN PARTIAL FULFILLMENT
OF THE REQUIREMENTS FOR THE DEGREE OF
DOCTOR OF PHILOSOPHY

UNIVERSITY OF FLORIDA

1996

UMI Number: 9703609

UMI Microform 9703609
Copyright 1996, by UMI Company. All rights reserved.

**This microform edition is protected against unauthorized
copying under Title 17, United States Code.**

UMI
300 North Zeeb Road
Ann Arbor, MI 48103

Dedicated to my mother and father

ACKNOWLEDGMENTS

I would like to acknowledge the many individuals that have made this work possible. Many thanks go to Dr. Kevin Jones for his guidance and support throughout the many years I've worked with him. This work could not have been possible without the direction and wisdom of Dr. Cammy Abernathy, not to mention the use of her MOMBE. I am very grateful to Dr. Steve Pearton for providing me with several opportunities for publication of AlGaP related studies, as well as his encouragement to succeed. I would also like to thank Dr. Paul Holloway and Dr. Tim Anderson who kindly agreed to serve on my dissertation committee.

Several people played an important role in assisting me with my research. Thanks go to Wish for editing my dissertation and preparing me for my defense, Maggie Puga for running SIMS analysis, Wayne Acree for microprobe analysis, and Augusto Morrone for helping me with the HRTEM.

I would also like to acknowledge my colleagues, Mike Antonell for the many times he has assisted me in my experiments and for opening my eyes to Gator sports, Mark Borek for his friendship throughout my graduate career, and John Viatella and Brent Gila, for all the good times.

I would also like to thank Chrisi Hughes for her encouragement and good ideas, and Lee for squirrel and potato procrastination. Both of them have added much joy to my life.

And finally, I would like to thank my sisters, Lynn and Lenee, and my mom and dad for their love and support.

TABLE OF CONTENTS

ACKNOWLEDGMENTS	iii
ABSTRACT	vi
CHAPTERS	
1 INTRODUCTION	1
1.1 Motivation and Objectives	1
1.2 Background	4
1.2.1 Mechanisms of Epitaxial Growth.....	5
1.2.2 III-Vs on Silicon.....	20
1.2.2.1 GaAs/Si.....	20
1.2.2.2 GaP/Si.....	24
1.2.2.3 Aluminum containing compounds on silicon	28
1.2.3 Growth of AlGaP by MOMBE	29
1.3 Summary and Scope of the Present Work.....	32
2 EXPERIMENTAL TECHNIQUES	34
2.1 Metal Organic Molecular Beam Epitaxy.....	34
2.1.1 Description of the MOMBE System.....	39
2.1.2 MOMBE Safety	44
2.1.3 AlGaP Precursor Selection	44
2.1.3.1 Aluminum precursor	45
2.1.3.2 Gallium precursor	47
2.1.3.3 Phosphine precursor	48
2.1.4 AlGaP Growth Parameters	48
2.1.5 Pyrometer Calibration.....	50
2.2 Transmission Electron Microscopy	52
2.3 Atomic Force Microscopy	54
2.4 Secondary Ion Mass Spectrometry	61
2.5 Electron Microprobe.....	62
3 SILICON WAFER PREPARATION.....	65
3.1 Wafer Cleaning Background	65
3.1.1 RCA Wafer Cleaning Process.....	67
3.1.2 Dilute HF Solutions	68
3.1.3 Plasma Cleaning	75
3.2 Epitaxial Silicon Surfaces	77
3.3 Silicon Substrate Preparation for MOMBE Growth.....	79
3.3.1 Experimental Techniques	79
3.3.2 Results and Discussion	81
3.4 Summary	87

4 NUCLEATION OF AlGaP ON SILICON.....	88
4.1 Introduction	88
4.2 AFM and TEM Analysis of AlGaP/Si Early Stages of Growth.....	89
4.3 Discussion of the Initial Stages of Growth.....	108
4.4 Conclusions	127
5 DEFECT ANALYSIS AND BUFFER LAYER GROWTH.....	129
5.1 High Resolution Transmission Electron Microscopy Analysis	129
5.1.1 AlGaP Island Results	130
5.1.2 Thick AlGaP Film Results.....	134
5.1.3 Discussion of TEM Defect Analysis.....	138
5.2 Buffer Layer and GaP Thick Film Optimization	148
5.3 Analysis of GaP/AlGaP Structures.....	151
5.4 Secondary Ion Mass Spectrometry Analysis	151
6 CONCLUSIONS AND RECOMMENDATIONS FOR FUTURE WORK	159
6.1 Conclusions	159
6.2 Recommendations for Future Work.....	160
REFERENCES.....	170
BIOGRAPHICAL SKETCH.....	175

Abstract of Dissertation Presented to the Graduate School
of the University of Florida in Partial Fulfillment of the
Requirements for the Degree of Doctor of Philosophy

NUCLEATION AND GROWTH OF AlGaP ON SILICON
BY METAL-ORGANIC MOLECULAR BEAM EPITAXY

By

Christopher Joseph Santana

May 1996

Chairman: Dr. Kevin S. Jones

Major Department: Materials Science and Engineering

We have investigated for the first time the compositional and temperature dependence of the early stages of growth of $\text{Al}_x\text{Ga}_{1-x}\text{P}$ on silicon by metal-organic molecular beam epitaxy (MOMBE). Triethylgallium (TEG) and dimethylethylamine alane (DMEAA) were used for the first time to grow $\text{Al}_x\text{Ga}_{1-x}\text{P}$ and precracked phosphine was used for the group V source. For $x=0$ to 0.45 and a nominal 50Å deposition, the growth mode of $\text{Al}_x\text{Ga}_{1-x}\text{P}$ on silicon has been identified to be island-type for the temperature range of 450-550°C. Increases in Al concentration have been shown to influence the nucleation behavior by the formation of a bimodal distribution of island heights.

The nucleation morphology of the $\text{Al}_x\text{Ga}_{1-x}\text{P}$ is believed to be influenced by the decomposition of TEG. A model has been proposed to explain the formation of the bimodal island distribution which attributes its presence to the mobility enhancement of surface aluminum by gettering of adsorbed ethyl radicals. This enhancement in surface mobility allows the deposit to reach a more equilibrium state of island formation through the ripening of large islands. Increased concentrations of Al in $\text{Al}_x\text{Ga}_{1-x}\text{P}$ were not found to induce planar growth even for $x>0.4$ at any growth temperature studied as was found in the growth of AlGaP/Si by metal-organic chemical vapor deposition (MOCVD).

TEM examination of the $\text{Al}_x\text{Ga}_{1-x}\text{P}$ structures revealed that the dominate defects in the islands and in the thick films were stacking faults and microtwins. Misfit dislocations were observed but were not common, and vertical defects, believed to be low angle grain boundaries, were found to extend from the heterointerface to the surface of the thick films.

Optimized buffer layer conditions were determined by the formation of continuous $\text{Al}_x\text{Ga}_{1-x}\text{P}$ films through the early coalescence of high densities of small islands. $\text{Al}_{0.15}\text{Ga}_{0.85}\text{P}$ buffer layers 500Å thick, grown at 450°C, were used for the growth of GaP/Si. However, $\text{Al}_x\text{Ga}_{1-x}\text{P}$ buffer layers only showed minimal improvement over GaP buffer layers in contrast with similar work using MOCVD grown material.

CHAPTER 1

INTRODUCTION

1.1 Motivation and Objectives

Silicon is the dominant material in the semiconductor industry today and its inherent properties will help ensure that it maintains its leadership position for many years to come. Silicon has the advantage of having a stable native oxide (SiO_2) which provides a high degree of protection to underlying devices and allows for definition of intricate device patterns. In addition, silicon is entirely nontoxic and in its raw form (silica), comprises approximately 60% of the minerals in the earth's crust [1], thus guaranteeing availability. Large diameter (up to 12") silicon wafers of exceptional quality can be fabricated with high purity and almost any desired doping level at low costs. However, silicon is not an optimum material choice in every respect. Many electronic and photonic applications require semiconductor properties that are not inherent in silicon such as high carrier mobilities and a direct bandgap. Thus research extends to many other semiconductor systems such as III-Vs and II-IVs to achieve the properties required for such devices. Many III-V compounds are available in bulk form; however, they are typically expensive. Some III-Vs are not available in bulk and the only means of producing them is through an epitaxial technique.

Over the past few decades, the field of heteroepitaxy has generated much interest and has seen rapid development. Heteroepitaxy allows the formation of artificial structures not available in nature and offers the exciting possibility of creating materials with electronic properties tailored for particular applications. This field has been aided by the development of epitaxial growth techniques such as metal-organic chemical vapor

deposition (MOCVD), molecular beam epitaxy (MBE) and most recently, a hybrid of these two techniques called metal-organic molecular beam epitaxy (MOMBE). Of particular interest is the use of these epitaxial techniques for the integration and growth of high performance III-V semiconductors on high quality inexpensive silicon substrates.

As a substitute for bulk III-V wafers, heteroepitaxy on silicon offers the advantage of large diameter inexpensive substrates with higher mechanical strength, higher thermal conductivity, and possible cointegration of devices in optical interconnects. Unfortunately, the quality of III-Vs grown on silicon is fairly poor because of several inherent differences in the material characteristics of the epilayers and substrate. Difficulties in achieving a high quality film arise from thermal expansion coefficient mismatch, lattice mismatch, substrate preparation and mode of growth. It generally takes a thick transition or buffer layer ($>2\mu\text{m}$) for a steady state, uniform, low defect density ($\approx 10^6/\text{cm}^2$) film to be produced. This can put the epilayer under severe tension and beyond a certain thickness (usually $>5\mu\text{m}$), the III-V layers have been found to simply crack [2]. III-V films are more susceptible to film cracking when the surface morphologies are rough due to concentration of thermal stresses around surface defects [2]. Thus it is desirable to obtain device quality material with a minimum transition layer thickness. The best routinely achievable defect densities for III-Vs on silicon are $\geq 10^6/\text{cm}^2$.

Ideally, in epitaxy, the film deposits in a manner such that it grows layer-by-layer (two-dimensional growth) producing a very smooth continuous covering of the substrate. This mode of growth occurs for many homo- and heteroepitaxial material systems including InGaP/GaAs, AlGaAs/GaAs, and AlGaP/GaP given the right growth conditions; namely proper V/III ratios, growth temperatures, surface reconstruction and precursors. However, in most cases, heteroepitaxial systems deposit in a manner such that the film material forms three-dimensional islands on the substrate surface that eventually grow together to form a continuous film. III-V materials such as GaAs and GaP grown on silicon typically display island growth. Thick films grown in this manner tend to have

rougher surface morphologies and higher defect densities than those grown under layer-by-layer conditions as will be discussed in depth in this chapter. Island growth can be minimized with (1) low lattice mismatch, (2) limited surface kinetics, and (3) wettable substrates.

Improved epilayer surface morphologies of III-Vs on silicon has been achieved by decreasing the severity of island growth. Increased concentrations of aluminum in $\text{Al}_x\text{Ga}_{1-x}\text{P}/\text{Si}$ have been shown to change the growth mode from a three-dimensional to a pseudo-two dimensional growth mode in MOCVD [3]. The term pseudo-two dimensional refers to the growth mode as described by coalescence of islands at the very early stages of growth. In other words, the addition of aluminum appears to be suppressing the severity of the island growth. The exact role that the Al plays on the nucleation of the MOCVD grown $\text{Al}_x\text{Ga}_{1-x}\text{P}$ however, is not known and has not been examined. Authors have speculated that the growth mode transition is related to the stronger bonding existing between the Al and Si as compared to that of Ga and Si [4] leading to a larger film-substrate interaction parameter. This is believed to result in either a decrease in the contact angles of the nuclei and/or an increase in the nucleation density which would lead to a continuous layer at earlier stages of growth. Because of the early island coalescence, AlGaP appears to be a good choice for a buffer layer material for the subsequent growth of III-Vs on silicon and has been demonstrated to be so in MOCVD grown material.

The focus of this dissertation has been the study and control of the initial stages of growth of $\text{Al}_x\text{Ga}_{1-x}\text{P}$ on silicon deposited by MOMBE for the purposes of fabricating a buffer layer to subsequent GaP growth. There are several reasons why the aforementioned issue is worth studying. Firstly, understanding the mechanisms and kinetic phenomena occurring during the nucleation of this material system can potentially lead to higher quality heteroepitaxial films grown on silicon by MOMBE through the minimization of transition layer thicknesses. Secondly, knowing what process parameters, including temperature, group V flow and composition, influence the early stages of growth most notably, will help

control the final properties of resulting heteroepitaxial films. And finally, the insight on nucleation and growth obtained from these studies can be carried over to similar lattice mismatched heteroepitaxial systems grown by MOMBE.

Understanding of the basic thermodynamics and kinetics of the chemical reactions and surface processes involved in MOMBE will accelerate the degree of control required for production of devices, as well as help to achieve advances and refinements in the growth technique itself. The initial stages of heteroepitaxial growth are still poorly understood and with the use of powerful techniques such as atomic force microscopy and high resolution transmission electron microscopy we can hope to obtain a picture on an atomic scale of the nucleation and growth processes.

1.2 Background

The material system chosen for this work was the $\text{Al}_x\text{Ga}_{1-x}\text{P}/\text{Si}$ system because of the noted success obtained in MOCVD studies as a buffer layer material. The lattice mismatch for this material system at room temperature is quite small as it varies from $\Delta a/a \approx 0.36\%$ for $x=0$ to $\approx 0.37\%$ for $x=1$, where $a_{\text{Si}}=5.431\text{\AA}$, $a_{\text{GaP}}=5.4505\text{\AA}$, and $a_{\text{AlP}}=5.451\text{\AA}$. MOMBE was chosen as the growth technique for these studies since it allows for low growth temperatures, growth of phosphorous containing materials, and precise control over the growth permitting depositions on the order of 50\AA in thickness. The source materials used in these experiments were triethylgallium (TEG), dimethylethylamine alane (DMEAA) and precracked phosphine.

In addition to being a buffer layer material, AlGaP has been considered to be a potential device material. Some of this interest has stemmed from the success of GaP which is a widely used material for light emitting diodes. GaP diodes can be used to produce optoelectronic displays that emit in several colors including green, yellow and red. AlGaP offers the potential to extend the light emission range of the GaP based material

system into the blue-green portion of the optical spectrum. Other applications of AlGaP include high temperature electronics [5] and GaP/AlP short period superlattices [6].

In the following chapter, a brief discussion of the epitaxial growth process is given, followed by a summary of the progress made in the growth of III-Vs on silicon. And finally, a review of AlGaP heteroepitaxy by MOCVD and MOMBE is presented.

1.2.1 Mechanisms of Epitaxial Growth

Epitaxial growth refers to the arrangement of crystallizing atoms upon a single crystal wafer such that the lattice structure of the epilayer is determined by the substrate. In order for epitaxial growth to occur there must be a "template" for the adatoms to utilize that is continuous across the entire wafer surface, i.e. a single crystal wafer that is cleaned of any surface contamination that would prevent single crystal growth of the epilayer. When the deposited material is the same as the substrate the epitaxial phenomena is called homoepitaxy, and otherwise heteroepitaxy. The most common example of heteroepitaxy in electronic thin film technology is the III-V system of AlGaAs on GaAs.

Heteroepitaxial growth can be either lattice matched or lattice mismatched. In lattice matched systems, the bulk lattice constant of the epitaxial layer is identical to the lattice constant of the substrate. Examples of this include $\text{In}_{0.49}\text{Ga}_{0.51}\text{P}/\text{GaAs}$ and $\text{Al}_{0.5}\text{In}_{0.5}\text{P}/\text{GaAs}$. In lattice mismatched systems, the lattice constant of the epitaxial layer is different from that of the substrate. For such a system, where a_e =bulk lattice constant of the epilayer material and a_s =lattice constant of the substrate, the mismatch can be described by:

$$f = \frac{(a_s - a_e)}{a_s}$$

Examples of lattice mismatched systems are numerous and include GaAs/Si, GaP/Si, Ge/Si, ZnSe/GaAs and GaN/Sapphire.

Heterostructures are often formed by growing ternary alloys or quaternary alloys on binary alloys with properly chosen composition in order to provide lattice matching and the desired bandgap and offset. Figure 1.1 shows the lattice constant as a function of composition for ternary III-V solid solutions. Lattice constants for binary alloys are also plotted. This plot assumes that the lattice constant of the ternary alloy is a linear combination of the lattice constants of the binary materials (Vegard's Law). When the lattice-constant line for a ternary solution crosses the horizontal line for a binary compound, the composition at the intersection provides lattice matching at room temperature. The area inside the boundaries denotes quaternary alloys. Note that none of the III-V compounds shown can be lattice matched to silicon and that the $\text{Al}_x\text{Ga}_{1-x}\text{P}$ alloy has the closest lattice parameter. Nitrogen containing compounds are required for III-V materials to be exactly lattice-matched to silicon.

There exist a number of ternary and quaternary III-V and II-VI systems, where the lattice parameters of the constituent binary compounds straddle the lattice parameter of silicon. These ternary and quaternary systems contain hypothetical compositions that match the lattice parameter of silicon as based on Vegard's law. This has led to predictions of exactly lattice-matched alloys for heteroepitaxial growth on silicon such as the GaAs-GaN system. However, some material systems, such as the AlN-GaN-AlP-GaP system, have wide regions of immiscibility in the solid state limiting their use. In fact nitrogen concentrations required to achieve exact lattice matching to silicon at room temperature are quite small, $y=0.0196$ and 0.0189 for the $\text{GaN}_y\text{P}_{1-y}$ and $\text{AlN}_y\text{P}_{1-y}$ alloys respectively. However, these concentrations are above the solid solubility of nitrogen in GaP as shown by Stringfellow [8]. To overcome the solid solubility problem, the use of low growth temperatures are likely to extend the range of metastable solid solutions enabling several alloy choices for lattice matching to silicon [9]. Nitrogen dilute $\text{Al}_x\text{Ga}_{1-x}\text{N}_y\text{P}_{1-y}$ represents a potential alloy candidate for an exactly lattice-matched III-V to silicon [9].

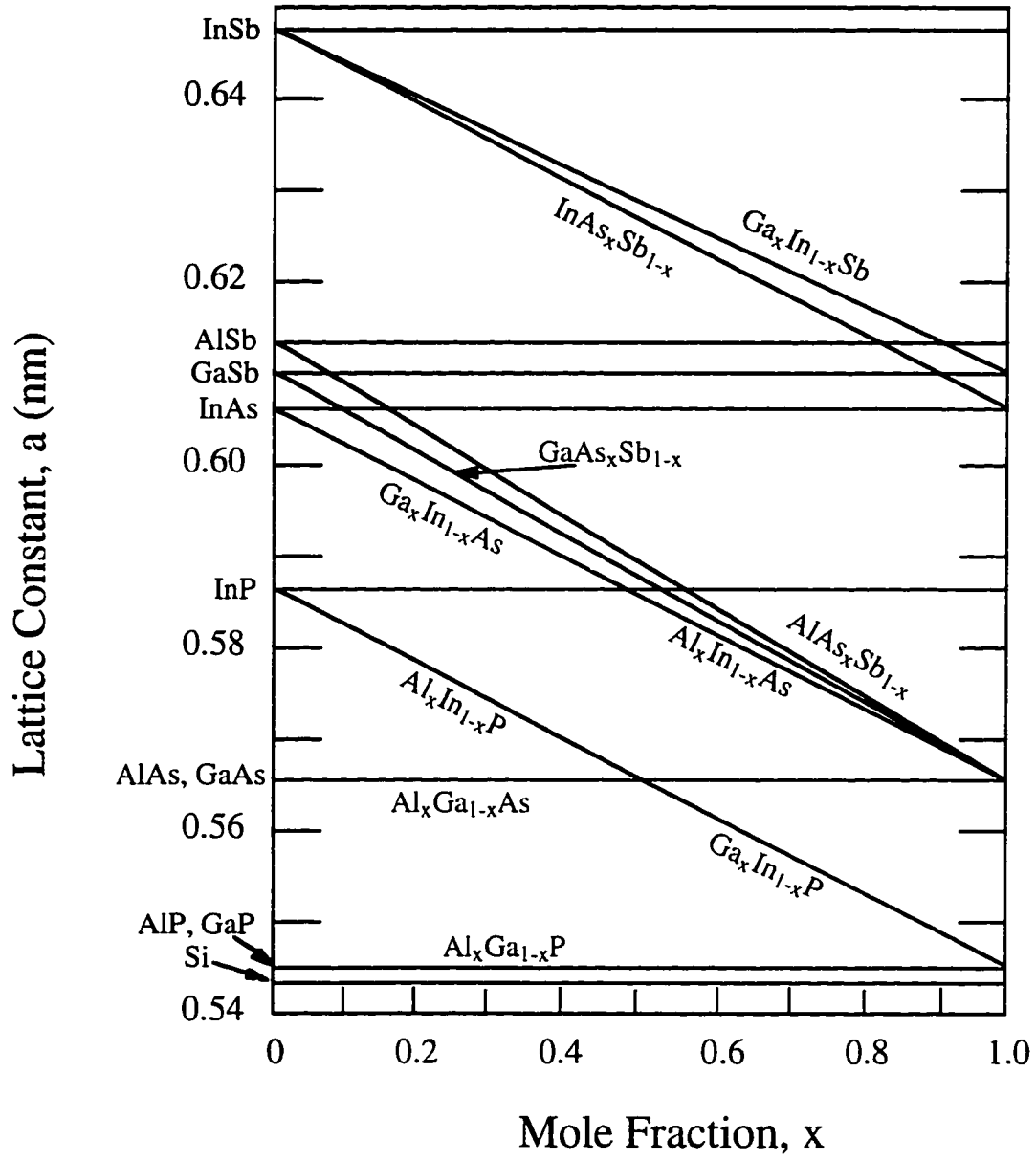


Figure 1.1 Lattice constant as a function of composition for III-V solid solutions [7].

Growth of lattice mismatched systems can lead to a variety of strain relieving mechanisms such as dislocation formation, change in growth mode, and film cracking, all of which may degrade the quality of the epilayer. There are in fact numerous factors in addition to lattice mismatch that impact the quality of both the epilayer and the initial stages of growth during the deposition of the film. Substrate orientation, surface cleanliness, local atomic reconstructions, steps, and defects can all influence the nature and quality of the epilayer. The relationship between surface kinetics and growth parameters, such as deposition rates and substrate temperature, also allow one to create metastable configurations in a film.

Epitaxial growth is realized on a substrate surface and proceeds through a sequence of steps as illustrated in figure 1.2 where the more important processes are as follows:

- 1) adsorption of the constituent atoms or molecules impinging on the substrate,
- 2) surface migration and dissociation of the adsorbed molecules,
- 3) incorporation of the constituent atoms into the crystal lattice of the substrate or the epilayer already grown,
- 4) thermal desorption of the species not incorporated into the crystal lattice.

Deposition of an epitaxial film is a fairly complex phenomenon involving many processes. Impinging beams of either atoms or molecules onto a heated substrate can lead to adsorption of the precursor species. For epitaxy to occur, molecular precursors must first undergo a decomposition process yielding an adsorbed atomic species on the substrate surface. Adatoms can migrate along the surface by jumping over activation energy barriers E_D at saddle points between neighboring adsorption sites. Any defects on the substrate surface represent fluctuations in the periodicity and are sites of preferred adsorption. The adatoms may reevaporate after a mean stay time τ_s , depending on the substrate temperature T_s and the activation energy E_a , or migrate a distance λ_s . If the surface diffusion length is large enough (depending on T_s and E_D), then during the adatom's stay it can meet another

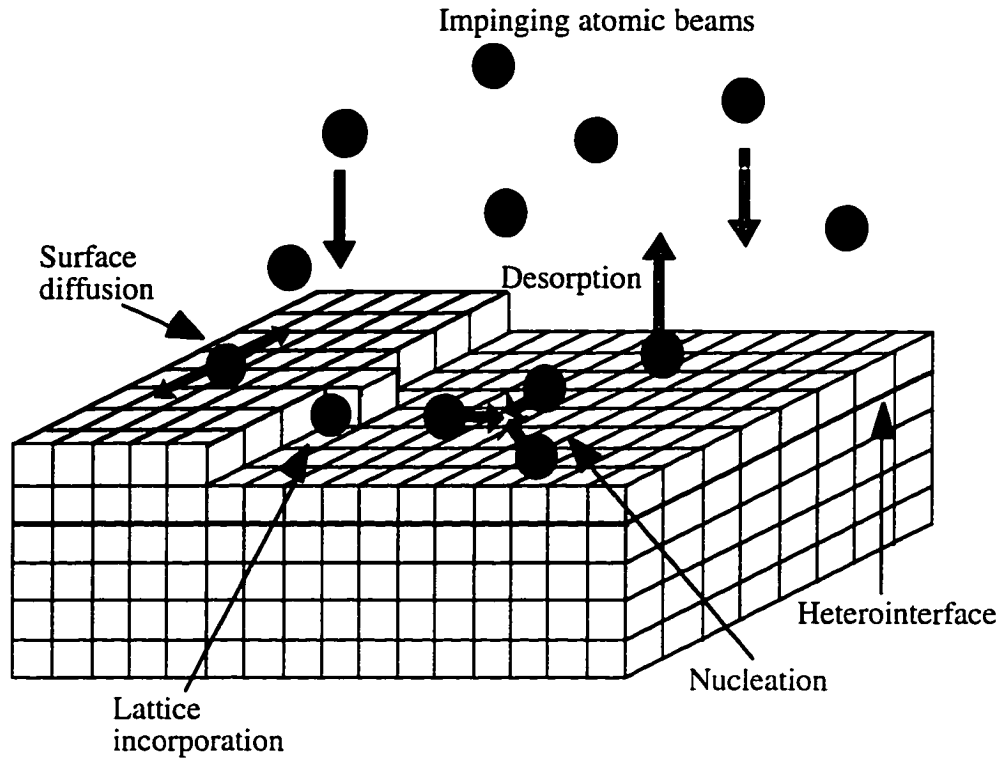


Figure 1.2 Schematic illustration of surface processes occurring during film growth.

adatom or island of adatoms. If the vapor is supersaturated, there will be a net flux towards the surface and critical nuclei will form and grow. In order for the nuclei to grow epitaxially, the arrival rate of adatoms at a island must be small enough (low supersaturation) to allow them sufficient time (high T_s) to take up appropriate positions in the epilayer lattice. Clearly, T_s is a very important deposition parameter as surface kinetics and precursor reactions are governed by it.

Adsorption and desorption can be described using mathematical equations developed using the kinetic theory of gases. Limiting ourselves to simple growth from vapor and approximating the vapor by an ideal gas satisfying the Maxwell distribution of velocities, the flux (I) of vapor molecules (molecular impingement rate) is given by

$$I = \frac{P}{\sqrt{2\pi mkT}}$$

where p =pressure, m =mass of the molecule, k =Boltzmann's constant, and T =temperature. Only a fraction α_v depending mainly on the nature of the surface is adsorbed, and thus defines the deposition rate by

$$R = \frac{\alpha_v p}{\sqrt{2\pi mkT}}$$

Kinetic equilibrium between vapor and substrate exists when the evaporation rate (R_e) equals the deposition rate given by

$$R_e = \frac{\alpha_v p_e}{\sqrt{2\pi mkT}}$$

There will be a net flux $\phi = R - R_e$ towards the surface, and consequently growth, if the vapor is supersaturated, i.e., $p > p_e$. Atoms adsorbed on the surface have a mean stay time τ_s given by

$$\tau_s = \frac{1}{\nu} \exp\left(\frac{E_a}{kT}\right)$$

where $\nu \approx 10^{13}/s$ is the vibration frequency of an atom on an adsorption site. During the residence time, an atom moves from one surface site to a neighboring site with a surface diffusivity given by

$$D_s = \lambda^2 \nu \exp\left(\frac{-E_D}{kT}\right)$$

where λ is the jump distance between two neighboring surface sites. In surface diffusion, the sites are available, whereas in bulk diffusion a site must be generated by formation of a vacancy, assuming substitutional diffusion. Desorption is much less likely than surface diffusion due to the differences in activation energy. Desorption involves breaking bonds while surface diffusion consists of motion only with no net change in the number of paired bonds.

There are preferred sites for adsorption on the substrate surface. Deposited atoms on the surface seek atomic sites that minimize the total energy of the system. An isolated atom on a surface adds dangling bonds (unsatisfied) to the system and raises the total energy. The number of free bonds can be reduced by adsorption at surface defects such as steps, kinks, and screw dislocations. In addition, islands themselves can be thought of as surface defects providing high-energy binding sites for further atom attachment during deposition.

Several models for nucleation identify surface energy as the parameter determining the mode of growth. Surface energy is defined as the energy spent to create a surface and is a positive quantity because energy is added. The effects of surface energy are seen in nature as a liquid tends to ball-up to reduce its surface area, and crystals tend to facet in order to expose those surfaces of lowest energy. When a solid is split in two, new surfaces are created and bonds are broken. Surface energy is related to the bond energy and to the number of bonds broken in creating the surface which in turn is related to the binding energy of the material. Metals tend to have high surface energies and oxides have low surface energies. Surface energy determines whether one material wets another and forms a uniform adherent layer. A material with a very low surface energy will tend to wet a material with a higher surface energy. On the other hand, if the deposited material has a higher surface energy it tends to form islands or ball-up on the low surface energy substrate.

Surface energy and surface tension have an interrelationship and are often used interchangeably. The connection of these quantities arises because solids can change their "surface energy" in two ways; either by increasing the physical area, as may occur from a cleave, or by changing the arrangement of atoms on a surface as in a surface reconstruction. The former case involves creating more surface area and the latter involves the detailed arrangements of atoms within a solid surface area which may be thought of as the work involved in stretching a surface. The different processes are related through a surface stress defined as $S = \gamma + d\gamma/d\varepsilon$ where the first quantity is the surface energy and the second quantity is the change in the surface energy with a variation in strain. In liquids no elastic deformation is possible and $d\gamma/d\varepsilon = 0$. The total surface energy is defined as $E_S = \gamma \times \text{area}$. Surface energies can be measured in a liquid state by capillary effect or in a solid state by zero creep experiments. Figure 1.3 shows the surface tension values of liquid materials at their melting point for several elements. The surface energies at room temperature can be estimated from these values and are found to be very similar.

Formation of heterostructures is always difficult, particularly if the heterostructure involves a superlattice of different types of materials. A superlattice requires forming the structure twice (i.e., first material B on material A, and then A on B). For one interface the surface energy balance will be unfavorable. It is easier to grow superlattices if both materials are semiconductors with similar surface energies.

Epilayers develop according to one of three distinct thermodynamically derived growth modes as illustrated in figure 1.3a; layer-by-layer (Frank-van der Merwe or 2D); nucleation of three-dimensional islands on a bare substrate (Volmer-Weber or 3D); and formation of three-dimensional islands on a microscopically thin uniform layer (Stranski-Krastanov). Since Bauer [10] first suggested criteria for the three growth modes, several improvements have been proposed. Bauer's criteria are based on equilibrium considerations and follow most easily from minimum free energy principles. In figure 1.3b each step is supposed to be of monatomic height and σ_e , σ_s , and σ_i are the specific

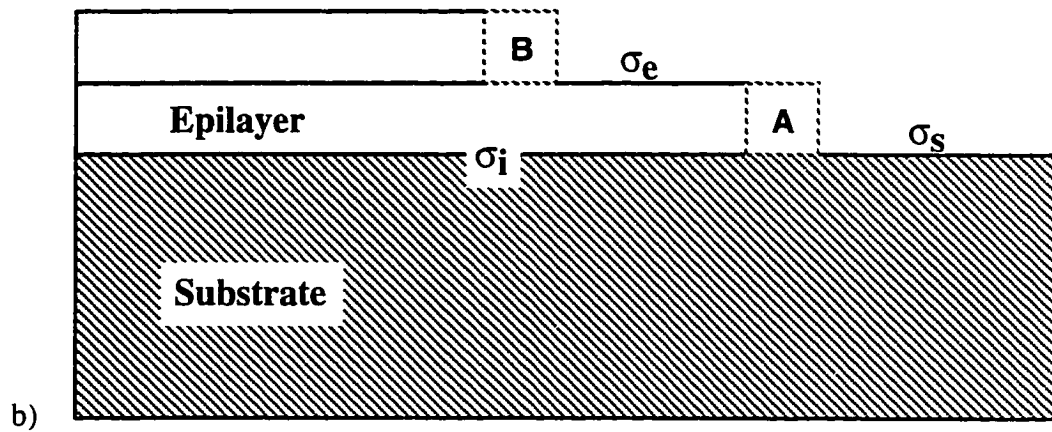
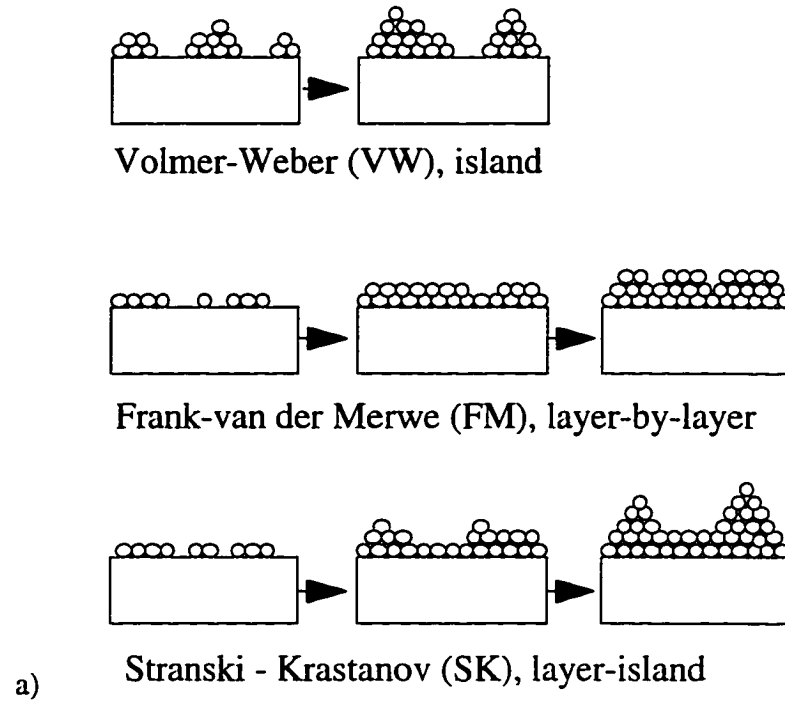


Figure 1.3 a) General growth modes for epitaxial films and b) substrate and two growing monolayers terminating at A and B [15]

surface free energies of the epilayer, the substrate and the epilayer-substrate interface. If the free energy of the epilayer-substrate system is less when an additional adatom is added at A rather than at B, then 2D growth is preferred. Bauer [10] reported that relative surface energies play a central role in determining which growth mode will occur at thermodynamic equilibrium: if the deposited material has larger surface energy than the substrate, it will tend to form islands; otherwise layer-by-layer growth is favored. These considerations are only valid if no chemical reactions, alloying or other changes of the surfaces occur during film growth. In systems for which surface energies are known, experimental studies support this predicted trend [11]. Bauer's criteria may be summarized by

$$\Delta\sigma = \sigma_e + \sigma_i - \sigma_s \leq 0 ; \text{layer-by-layer} \\ > 0 ; \text{island growth}$$

where σ_e and σ_s are the surface energies of the epilayer and substrate respectively and σ_i is the interfacial energy. It follows that if the temperature changes of the surface energies or the kinetic factors of the process are negligible only one mode of growth is possible for a given substrate-deposit system. Comparatively, if the chemical potential, $\mu(n)$, of the second monolayer of heteroepitaxial growth, $\mu(2)$, is greater than $\mu(1)$ then layer-by-layer growth is favored and when $\mu(1) > \mu(2)$, island growth should occur [12].

The mode of growth has also been shown to be sensitive to the supersaturation, ζ , which is defined by [13]

$$\zeta = \frac{P}{P_e} = \frac{R}{R_e} = \frac{N_l}{N_{le}}$$

where P is the vapor pressure of the supersaturated molecular beam impinging on the substrate and P_e is the equilibrium vapor pressure at the substrate temperature. The R 's are

the deposition rates and N 's refer to the adsorbed concentration of cation species. Markov and Kaischew [14] showed that Bauer's criteria could be rewritten as

$$\sigma_s \geq \sigma_{hkl} + \sigma_i - \frac{\Delta\mu}{2k_{hkl}b^2}, \text{ layer growth}$$

$$\sigma_s < \sigma_{hkl} + \sigma_i - \frac{\Delta\mu}{2k_{hkl}b^2}, \text{ island growth}$$

where σ_{hkl} is the specific surface energy of the contact plane of the overgrowth. The constant k_{hkl} depends on the orientation; b is the nearest-neighbor distance for the substrate and $k_{hkl}b^2$ is the area of an atom in the contact plane. And finally, $\Delta\mu$ is given by $\Delta\mu = kT_s \ln \zeta$, where k is Boltzmann's constant, and T_s is the substrate temperature. It is shown in these equations that increasing the supersaturation favors layer growth over island growth. Therefore, there exists a critical supersaturation at which the growth mode will change from island to layer-by-layer.

The ideal mechanism of growth of device films is by layer-by-layer deposition of the film atoms. Films grown in this fashion are planar and the thicknesses of the films are more easily controlled. Many materials, however, do not deposit on the substrate in the layer-by-layer mode and it is in fact more common to observe deposition occurring by the formation of islands at the very early stages of growth followed by their coalescence resulting in a continuous film having a rough surface morphology.

More recently, the effect of epitaxial strain on the growth mode has been examined. Phenomenological analysis based on continuum elasticity predicts that layer-by-layer growth is never the equilibrium morphology in the presence of lattice misfit [16], but rather, is metastable with respect to island formation on a thin wetting layer. Recent atomistic simulations support this conclusion [17] and confirm that layer-by-layer growth is the ground state only for zero misfit. The misfit between the epilayer and substrate leads to a strain energy that serves as the driving force for island generation in most heteroepitaxial

systems. The only driving force for uniform films is a strong interaction between the film and substrate. It is only when the film atoms interact directly with the substrate that there will be a driving force for layer-by-layer growth as shown in figure 1.4. In addition, island formation will be independent of the film-substrate interaction beyond the deposition of a few monolayers because the island will be outside the range of that interaction [17].

Although uniform films are not the equilibrium state for most heteroepitaxial systems, an activation barrier to forming islands must be overcome due to the formation of surface area. Thus, temperature effects will play a large role in the determination of the film morphology. As a crystal growth process, MOMB is, by definition, a dynamic phenomenon. A consideration of thermodynamics as well as kinetics is therefore essential. While thermodynamics embodies the essence of the behavior of the physical system at equilibrium, the kinetics controls the ability of the system to move towards the equilibrium state within the given conditions. Surface transport from high to low chemical potential regions can thus be suppressed (enhanced) by growth conditions that kinetically limit (support) the mobility of the surface species. Surface kinetics decide the morphology of the surface and different growth conditions will lead to different observed morphologies at the same thickness. To form a smooth strained film, one should slow the transportation rate of surface species from high to low chemical potential regions. Kinetic control is the basis of the two-step growth technique.

Orr et al. [19] studied the morphological evolution of strained films during growth and observed that the morphology of the film is clearly a function of overlayer strains according to Monte Carlo simulation. For a fixed strain, it was possible to impede island formation by reducing the system's ability to reach equilibrium through the use of low substrate temperatures and/or rapid deposition. The degree to which a system can reach equilibrium is decided by the diffusion length $l = \sqrt{D\tau}$, where D is the surface diffusion coefficient and τ is the time to deposit a monolayer. At low growth temperatures and high nuclei density, surface species can only diffuse a short distance before they are

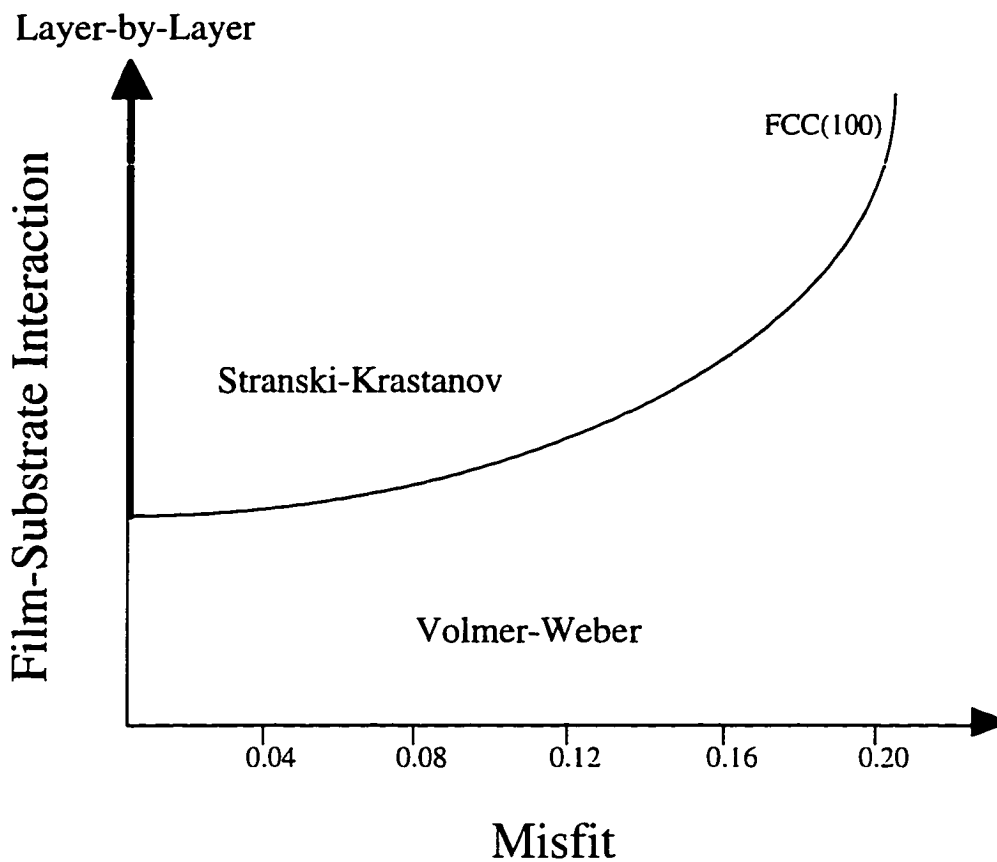


Figure 1.4 Equilibrium growth modes as a function of misfit and strength of film-substrate interaction assuming Leonard-Jones interatomic potential [18].

incorporated into lattice sites. At high impingement fluxes, the time needed to deposit one monolayer is short; therefore, island formation is kinetically delayed or frozen out. However, changes in growth rate were not found to play a large role in other work [20].

Snyder, Mansfield, and Orr [20] investigated the surface diffusion kinetics further and developed a mathematical model for the prediction of a critical thickness for the transition from the 2D to the 3D growth mode. They found that the surface diffusion of the adatoms was the major factor in determining the growth mode and were able to grow highly strained pseudomorphic layers at low temperatures. These planar films grown at low temperatures were unstable to the formation of islands upon high-temperature

annealing which supports the view that an island is a lower energy configuration than a flat, uniformly strained film. This is understood by considering that a strain-relieved island reduces the elastic energy over its volume at a proportionally smaller cost of additional surface energy. Snyder showed that the thickness at which a system favors island growth is determined by the critical thickness given by

$$h_c = \frac{\gamma_{FV}^2}{\kappa^2 \epsilon^4 l}$$

where l =surface diffusion length, κ =the bulk modulus, γ =surface tension, and ϵ =the lattice misfit. For $t < t_c$ metastable elastically strained films will grow in a layer-by-layer fashion; for $t > t_c$, coherent island formation should occur. This equation applies to a kinetically limited system and as the system approaches equilibrium conditions h_c essentially approaches zero. Also predicted from the analysis was the minimum temperature for island suppression given by

$$T_{min} = \left[\frac{k_B}{E_A} \ln \left[\frac{1.44 D_0 \tau \kappa^2 \epsilon^4}{\gamma_{FV}^2} \right] \right]^{-1}$$

where k_B =Boltzmann's constant, E_A =activation energy, D_0 =surface diffusion coefficient, and τ =time to deposit a monolayer.

It has been shown that beyond a certain thickness threshold, elastic relaxation through free surfaces induces the formation of coherent islands in strained semiconducting systems. Several research groups have used this to intentionally grow 3D structures. In InGaAs/GaAs, island growth has been used to directly produce quantum dots and nanostructures [21]. However, the control of the dot sizes and size homogeneity is a technological challenge for the fabrication of devices.

The main tendencies in the mode of growth for one material system on another have been summarized by Markov and Stoyanov [12], and are as follows:

- when the interfacial bonding is weaker than the bonding in the film material itself, the formation and growth of isolated 3D islands rather than monolayers is favored;
- lower growth temperatures favor layer-by-layer growth;
- higher deposition rates favor layer-like growth;
- the lattice misfit plays an important role in determining the mode of growth and larger misfits increase the tendency towards island-like growth;
- the crystallographic orientation of the substrate affects the mechanism of growth and a more densely packed substrate plane favors layer-like growth.

Despite the fact that layer-by-layer growth is never the equilibrium morphology in strained-layer heteroepitaxy, kinetic constraints on mass transport often permit this growth mode. Relaxation of accumulated misfit induced strain then become important. Three fundamental concepts introduced by Frank and van der Merwe [22,23] have dominated most treatments of strain-layer epitaxy. Their theoretical analysis of the equilibrium ground state showed that (1) a thin overlayer will strain elastically into coherence with its substrate if the misfit, f , does not exceed a critical value ϵ_c ; (2) even if $|f| > \epsilon_c$, the overlayer will still strain into registry with the substrate except for a periodic array of localized regions called misfit dislocations where registry is disrupted; and (3) ϵ_c is a function of the overlayer thickness h_c as misfit dislocations occur at the interface to relieve the mismatch strain.

With respect to 3D island growth, the morphology of the initial stage of growth will depend on various growing conditions. Researchers have shown that significant differences in dislocation distributions exist in these materials depending on the growth mode [24]. ZnSe has been shown to grow on GaAs three-dimensionally (Ga-stabilized) and two dimensionally (As stabilized) depending on the GaAs surface treatment. Guha et al. [24] have shown that the threading dislocation densities are an order of magnitude

higher in the 3D grown materials. This has been attributed to the coalescence of islands which act as an additional dislocation generation mechanism.

Kitahara et al. [25] compared the MOCVD growth of III-Vs on Si substrates with that on III-V substrates to distinguish the effects of the lattice mismatch and those originating from Si substrates. The growth modes of heteroepitaxy depositions of GaAs/GaP, GaP/GaAs, GaP/Si, GaAs/Si, and AlAs/Si were examined using RHEED. From their data, as shown in table 1.1., they concluded that there appeared to be no clear correlation between the lattice mismatch and the occurrence of 3D growth. For example, the AlAs/Si, GaAs/Si, GaP/GaAs systems all have similar lattice mismatches but each grow with a different growth mode. Also note that GaP deposits on GaAs in a layer-by-layer fashion, whereas in the opposite case the deposition is layer-island. The 3D growth in this experiment was said to be influenced by residual oxide on the silicon surface and/or the unintentional adsorption of intrinsic atoms from the growth chamber. They also found that covering the Si surface with As or P atoms protected the silicon surface from the uncontrolled adsorption of the intrinsic atoms. But regardless of the exact details of the growth of these material systems, the growth modes have been shown to be vastly different even in systems with similar lattice mismatches. These experiments have shown that there are more factors than one that must be considered in uncovering the growth mode of one material on another.

1.2.2 III-Vs on Silicon

1.2.2.1 GaAs/Si

The utilization of silicon substrates for the heteroepitaxial growth of III-V materials has been an area of research for many years. GaAs on silicon was under immense study in the mid to late 1980's in hopes of combining the high speed and optoelectronic properties of III-V devices with the high-density circuit capacity of silicon. There were several difficulties, however, in the heteroepitaxial growth of GaAs/Si as well as with other III-Vs

Table 1.1 Growth modes of various semiconductor pairs for heteroepitaxy at a growth temperature of 500°C.

Epi./sub.	$\Delta a/a \cdot 100$ (%)	Growth mode
GaAs/Si	4.1	3D (VW)
GaP/Si	0.4	3D (VW)
AlAs/Si	4.3	2D (SK)
GaAs/GaP	3.7	2D (SK)
GaP/GaAs	3.7	2D (FM)

on silicon that made it hard to achieve defect densities below $10^6/\text{cm}^2$. These difficulties included thermal expansion mismatch, antiphase domains, silicon surface preparation, mode of growth, and lattice mismatch (4.1%). Such differences between Si and GaAs gave rise to antiphase domains (APDs), tensile stresses, and dislocations in the epilayer. APDs can be controlled in two ways; (1) use a wafer orientation where the APD does not occur such as (211), and (2) establish a double-step surface (100) using miscut wafers and a high temperature pregrowth desorption process.

Much less success has been achieved in controlling the built-in thermal stresses that are generated when the epilayer is cooled from the growth temperature to room temperature. Addressing the problem of thermal stresses, Tachikawa [26] examined the defect densities of both GaAs/Si and GaP/Si at the growth temperature using an in situ etching technique (HCl vapor phase etching) and compared these values to the defect densities of the materials after cooling. The results of the etching experiments revealed that the dislocation densities at the growth temperature for GaAs and GaP were nearly identical with $4 \times 10^4/\text{cm}^2$ for GaAs and $5 \times 10^4/\text{cm}^2$ for GaP. Upon cooling, the dislocation densities rose to $8 \times 10^6/\text{cm}^2$ and $2 \times 10^7/\text{cm}^2$ for GaAs ($\alpha = 5.4 \times 10^{-6}/\text{K}$) and GaP ($\alpha = 5.3 \times 10^{-6}/\text{K}$)

respectively. Note that the dislocation densities of GaAs and GaP at the growth temperature were very similar even though the lattice mismatches are quite different. These results show that high dislocation densities are caused by thermal stresses and possibly by the 3D growth mode of both GaAs and GaP. Growth of GaAs on silicon at reduced temperatures can minimize the thermal expansion problem, and minimizing the severity of island growth can possibly reduce defects generated from three-dimensional growth.

Many studies have demonstrated that three-dimensional GaAs islands are present on the Si surface during the early stages of growth. TEM studies suggest that the origin of threading dislocations in GaAs on silicon can be traced to coalescence of these islands during growth [27]. Most GaAs grown on silicon utilizes a two-step growth procedure to encourage the early coalescence of the three-dimensional islands and to terminate threading dislocations in the vicinity of the heterointerface.

Biegelsen et al. [28] made direct observations of the early stages of growth of MBE grown GaAs (18nm) on misoriented (100) silicon substrates by using cross-sectional TEM. They found that the island spacing and stacking fault spacing was a function of temperature as shown in figure 1.5.

The increasing distance between islands with increasing temperature was explained to be a result of a decreasing nucleation density, and/or increasing coalescence of growing supercritical nuclei. As the temperature was lowered the greater deviation from equilibrium was manifested into the characteristics of the grown layer. At lower temperatures, three-dimensional growth and short diffusion lengths resulted in coalescence when the islands were still relatively small. Epitaxial crystallization still occurred at the lower temperatures, but atomic mobilities were insufficient for surface energy minimization to occur. There was also a rough proportionality between the defect density and island density. This effect was explained by the formation of stacking faults during the coalescence of islands. The decrease in stacking fault density with increasing temperature demonstrates that defect creation is not a result of thermal expansion differences.

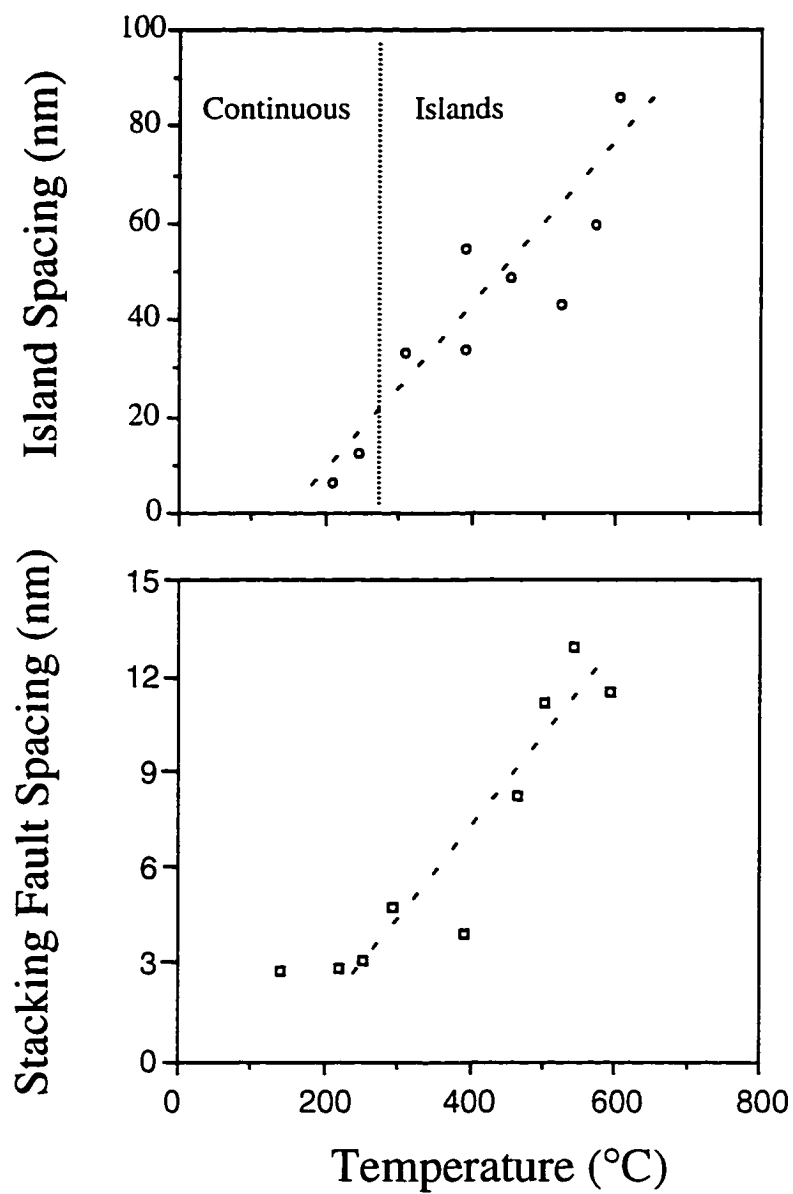


Figure 1.5 Island spacing as a function of temperature for 18nm thick GaAs films. The dotted line is to guide the eye [28].

The success of the two-step growth technique in the deposition of GaAs/Si and other III-Vs on silicon is a result of limiting the surface kinetics. Other forms of surface kinetic limitations have also been explored including prelayers that change the substrate surface reconstruction, addition of atoms that have high binding energies, and overcrowding of the surface with group V adatoms.

Soga et al. [29] studied the initial growth mechanism of GaAs on silicon by MOCVD. Si(100) substrates, 2° off toward [011], were used and the GaAs epilayers were grown at 950°C. The V/III ratio was varied from 10→800 to study the changes in nucleation of the GaAs. They found that the island density increased from 10^7 to $10^8/\text{cm}^2$ as the V/III ratio increased from 10 to 40. For ratios >40 there was no change in the island density, and this is believed to be due to the efficient dissociation of AsH_3 . The increased nucleation was attributed to the large amount of absorbed arsenic which was effective in capturing the group III migrating species, thus decreasing the effective group III surface diffusion length. The higher density of islands resulted in the coalescence of the film at a thinner layer thickness.

Several recipes for dislocation confinement have been developed and utilized in the GaAs/Si material system including strained-layer superlattices (SLS) [30], rapid thermal annealing (RTA) [31], and buffer layers [4,32,33]. These techniques for dislocation reduction are very effective in reducing the typical $10^8/\text{cm}^2$ dislocation densities found in III-V/Si materials down to the $10^6/\text{cm}^2$ range. The research done in this dissertation has utilized the two-step growth technique in combination with the use of a AlGaP buffer layer to minimize defects in the main epilayer.

1.2.2.2 GaP/Si

One of the major problems of the growth of GaP on silicon, like GaAs on silicon, is the 3D growth mode in the early stages of growth. The main difference between the two systems is that GaP has a much smaller lattice mismatch to silicon (0.37%) than does GaAs

(4.1%). As previously mentioned, lattice mismatch between the epilayer and substrate is one of the driving forces for 3D growth. In the GaP on silicon system, however, the primary factors leading to 3D growth are believed to be the high mobility of the Ga adatoms on silicon and the surface energy differences between the GaP and silicon. Many aspects of GaP/Si research are similar to GaAs/Si work and in fact many of the same arguments for experimental observations are applied as well. Because of the difficulties in growing phosphorous containing compounds in MBE, the majority of the GaP/Si work has been done using MOCVD. The following is a brief review of some of the more relevant work done on this material system.

GaP layers grown directly on silicon without any special treatments by MOCVD typically have dislocation densities on the order of $10^8/\text{cm}^2$. Surface morphologies are found to be improved when a two-step growth process is used [34] and defect densities can be reduced using SLS and buffer layers as well as post-growth techniques. Techniques to minimize the severity of island growth include the use of low temperatures, prelayers, and high group V flows.

Low temperatures can be utilized to limit the effects of thermal expansion difference between GaP and silicon as they were used in the GaAs/Si material system. Unfortunately, many structural defects exist in the low-temperature GaP/Si layers with defects such as dislocations and/or stacking faults propagating towards the upper GaP layer. In MOCVD, the migration of the GaP precursor species is enhanced by high growth temperatures (900°C) and formation of GaP islands occurs more easily. On the contrary, for low T_G (500°C), the migration is not sufficient and the whole substrate may get coated with polycrystals uniformly.

Pretreatment of the silicon wafer surface in MOCVD prior to GaP deposition has been studied. Depositing a group V prelayer has been found to improve the crystalline quality of subsequent GaP epilayers [35]. Preflows of AsH_3 and PH_3 have been explored with results indicating that As atoms are absorbed more easily on to the silicon surface than

P atoms [35]. It is believed that the Ga atoms will bond with the As-terminated surface and become stable. Kohama et al. [35] used TEM to examine the initial stages of GaP epitaxial growth on silicon substrates with and without AsH₃ preflow and confirmed that AsH₃ preflow suppressed the severity of island growth which allowed GaP epilayers to grow in a more planar fashion. The area between the GaP islands was found to decrease with AsH₃ preflow and appeared to improve the wetting between GaP and silicon [35]. Young's model was used to explain the decrease in contact angles of the GaP islands as shown in figure 1.6.

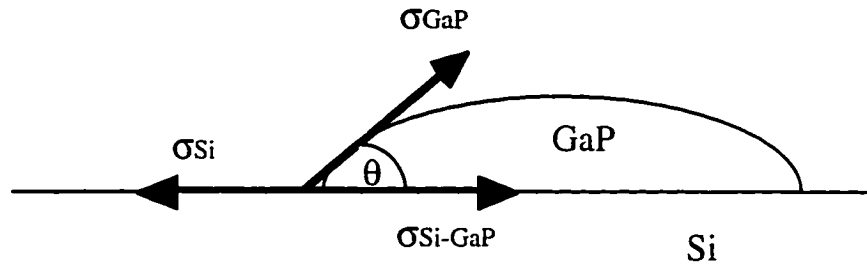


Figure 1.6 Schematic diagram of surface t of a GaP

$$\sigma_{\text{Si}} = \sigma_{\text{Si-GaP}} + \sigma_{\text{GaP}} \cos\theta$$

where

σ_{Si} = surface energy of the silicon substrate to air

$\sigma_{\text{Si-GaP}}$ = interfacial energy between Si and GaP

σ_{GaP} = surface energy of GaP

θ = wetting angle

From this model, the decrease in contact angles of the GaP islands was attributed to a reduction in Si-GaP interfacial energy.

The effect of prelayers on the growth of GaP on silicon has been further studied by Bi et al. [36] using gas-source molecular beam epitaxy (GSMBE). They investigated the effect of using different prelayers (As₂, P₂, Al (elemental), Ga (elemental), and Ga+Al) on

the quality of the GaP films grown on silicon using the two-step growth technique. The prelayers were introduced to the substrate at 400°C for 10s followed by the growth of the low temperature GaP layer. The temperature was then raised to the growth temperature of 750°C and the main GaP film of 2.5µm was grown. X-ray FWHM for the various samples revealed that the best layer quality was obtained from the Ga prelayer as shown in table 1.2. Similar results were found upon measuring surface roughness using atomic force microscope. The variations in film quality were attributed to the differences in bond energies of each of the prelayer species to the silicon substrate. Ga prelayers have also been successfully used in the growth of GaAs/Si [37] and GaAs/Ge [38].

Table 1.2 X-ray FWHM of 2.5µm thick GaP on silicon grown using different prelayers

Prelayer Species	FWHM (arcsec)
PH ₃	628
AsH ₃	394
Al	469
Al+Ga	437
Ga	221

The island density of GaP is also found to increase with increasing V/III ratios and the growth mode in turn, changes from 3D to pseudo-2D. A study conducted by Soga et al. [29] examined the initial growth mechanism of MOCVD grown GaP at 900°C with V/III ratios varying from 40-800 (sources are TMG and PH₃). They found that the island density increased gradually with increasing V/III ratios from zero to 600 and when the ratio

was increased to 800, the GaP layer became flat. For the case of a high V/III ratio, the Ga atoms will bond with more than two P atoms in the vapor because of the high concentration of P. The P atoms are easily adsorbed on the substrate as they have many dangling bonds. They migrate little and become stable on the substrate because of bonding between a few Si and P atoms. Thus, the growth of extremely thin and 2D layers is realized.

1.2.2.3 Aluminum containing compounds on silicon

The growth of Al-containing III-V compound semiconductor layers on silicon has been investigated by several authors primarily with the intentions of using the material as a buffer layer for GaAs growth [3,39] however, the nucleation of AlGaP on silicon has not been reported. It has been reported for MOCVD that the layer roughness of Al-containing compounds i.e., AlGaP and AlGaAs, is better than that of GaP and GaAs [40]. Similar findings were found in research conducted by Kitahara et al. [25], in the growth of AlAs on Si by atomic layer epitaxy (ALE) as compared to GaAs on Si. These results indicate that Al contributes to improving the flatness of epilayers on silicon and appears to be independent of growth technique.

Noto et al. [3] used MOCVD to grow GaAs on misoriented Si(100) substrates using 1 μm thick $\text{Al}_x\text{Ga}_{1-x}\text{P}$ buffer layers and studied the effect of the buffer layer on the crystallinity of the GaAs top layers. They found that the growth mode of the AlGaP layers changed from 3D growth to pseudo-2D growth with increasing Al composition. TEM experiments revealed that the surface morphology of the GaAs layer corresponded to the changes in the growth mode. When $x > 0.45$, the surface morphology became smooth. When the Al composition was close to 0.5, the crystallinity of the GaAs was best with a defect density of $2.5 \times 10^7/\text{cm}^2$ in the GaAs layer. The initial stages of nucleation of the AlGaP were hypothesized to consist of a very large number of nucleation sites on silicon which covered the Si surface rapidly.

Kitahara et al. [41] grew GaAs and AlAs on misoriented Si(100) substrates using atomic layer epitaxy. Although the difference in lattice constants between GaAs and AlAs is only about 0.15%, their growth behavior on silicon is quite different. AlAs achieved a continuous layer at a much thinner layer thickness than the GaAs and had a better crystal quality. This was explained by comparing the bond strengths of Al-Si (stronger bond strength) and Ga-Si. However, no data on the bond strengths were given.

Egawa et al. [39,42] showed that the use of $\text{Al}_{0.5}\text{Ga}_{0.5}\text{As}/\text{Al}_{0.55}\text{Ga}_{0.45}\text{P}$ intermediate layers in the growth of $3\mu\text{m}$ GaAs on Si resulted in better quality material than GaAs grown by the two-step growth technique. Room-temperature continuous wave AlGaAs/GaAs single quantum well lasers fabricated with the GaAs grown on the buffer layers had lower threshold current densities, higher internal quantum efficiencies, and smoother surface morphologies than the GaAs grown by the two-step growth process. Optical and transport properties of these types of devices are thought to be affected by the microroughness of the surface and heterointerface.

Soga et al. [40] grew $3\mu\text{m}$ thick GaAs and AlGaAs films on misoriented Si(100) substrates by MOCVD. Both GaAs and AlGaAs were found to grow three-dimensionally on silicon, however, the AlGaAs islands became contiguous at a nominal thickness of 22.5nm whereas the GaAs appeared as separated islands at the same thickness. There was also a high density of dislocations, stacking faults and microtwins in the $3\mu\text{m}$ thick GaAs layer, but drastic reduction of such defects was observed in the planar AlGaAs layer. It was speculated that the AlGaAs nucleation behavior could be attributed to the highly reactive nature of the Al. This could contribute to increased wetting of the Si substrate by the AlGaAs layer through the formation of Al-Si bonds.

1.2.3 Growth of AlGaP by MOMBE

The growth of AlGaP by MOMBE has been limited thus far to deposition on GaP substrates. The advantage of this is that AlGaP is essentially lattice matched to GaP for all

mole fractions, similar to AlGaAs on GaAs. This material system is therefore essentially free of the associated lattice matching concerns that hinder the development of many semiconductor systems. All studies of AlGaP grown by MOMBE have utilized (100) oriented GaP substrates and precracked phosphine as the group V source. The work previously conducted on AlGaP/GaP was reviewed by the author prior to selecting the appropriate conditions for growth of AlGaP/Si for this dissertation. However, because DMEAA had not yet been used as an Al source for the growth of AlGaP/Si, several calibration experiments were required. The following is a brief review AlGaP/GaP experiments grown by MOMBE conducted by other authors.

Ozasa et al. [43] studied the growth rate and composition of $\text{Al}_x\text{Ga}_{1-x}\text{P}$ as a function of temperature, using TEG and triethylaluminum (TEAl) as group III precursors. The growth rate of the ternary was found to be limited by source decomposition at lower growth temperatures ($<350^\circ\text{C}$) and remained fairly constant up to the maximum growth temperature studied (620°C). In addition, for a given flow of sources, the composition of the ternary was fairly constant over the temperature range of 400°C - 620°C .

Yoshimoto et al. [44] studied the epitaxial growth of GaP and AlGaP on GaP(100). AlGaP epilayers were grown at substrate temperatures ranging from 420 to 500°C and were found to have smooth surfaces and interfaces as well as streaky RHEED patterns. This is a result of the layer-by-layer growth mode believed to occur for AlGaP on GaP. The decomposition of the group III sources TEG and TEAl were found to limit the growth rate of AlGaP at lower substrate temperatures ($<390^\circ\text{C}$). To enhance the decomposition of the precursors at low temperatures ($<390^\circ\text{C}$), irradiation with photons was used. As will be discussed in Chapter 4, the growth mode of AlGaP on silicon is not layer-by-layer as found for AlGaP/GaP leading to very different film morphologies.

Baillargeon et al. [45] grew $\text{Al}_x\text{Ga}_{1-x}\text{P}$ epilayers on (100) GaP with x ranging from 0 to 1. Elemental Al and Ga were used as the group III sources and growth rates ranged from 1.3 - $1.9\mu\text{m/h}$ with growth temperatures of nominally 700°C . Very low defect

epilayers with featureless surface morphologies and correspondingly indicative RHEED patterns were achieved for the growth of AlGaP for $x=0$ to 1. Notable work in this publication included the investigation of doping the AlGaP with elemental silicon to achieve n-type material with carrier concentrations as high as $6 \times 10^{18}/\text{cm}^3$. In addition, the effects of changing the GaP chemical cleaning solution were studied so as to minimize surface damage prior to growth. A cleaning solution of 4 HCl: 4 HNO₃: 5 H₂O was found to leave the GaP surface featureless with a thin native oxide protective layer. This solution was chosen as the technique for GaP wafer preparation for this author's experiments as will be discussed in Chapter 5.

A novel approach at improving the luminescence of LEDs has recently been explored with the growth of AlP/GaP superlattice layers. AlGaP with a high luminescence efficiency would provide the realization of optical devices operating at the shortest wavelength range (506-550nm) available from the III-V semiconductors with a zinc-blend lattice structure. Unfortunately, AlGaP has an indirect bandgap (2.26-2.45eV) throughout its composition range which leads to low luminescence efficiencies. In order to improve these efficiencies, AlP/GaP short-period superlattices have been grown by several deposition techniques including MOMBE [46] for the purposes of fabricating a material that behaves as a direct bandgap material. All studies thus far have utilized GaP(100) substrates for deposition. In the short-period superlattice, the conduction band minimum of the host material is brought into the center of the Brillouin zone in the k space by the zone-folding effect. Therefore, a direct bandgap structure can be expected leading to an optical transition probability that is 10-100 times stronger than that of the indirect optical transition [47]. The zone-folding effect however is considered to occur only in high quality superlattices with importance on abrupt and flat interfaces between the GaP and AlP layers. For this material system to be grown on silicon substrates and to work, the importance of establishing a smooth AlGaP buffer layer becomes clear.

Although it has been shown that AlGaP can be successfully grown by MOMBE on GaP, more work is needed in the area of AlGaP heteroepitaxy, especially AlGaP-on-Si, to gain a better understanding of the material and its nucleation and growth mechanisms.

1.3 Summary and Scope of the Present Work

The growth of high quality III-V materials on silicon is a very challenging task for any grower. Growth difficulties are many and current technology requires that growth "tricks" and kinetics be the tools by which these difficulties are overcome. The use of aluminum containing compounds for improvement in epitaxial growth appears to be a promising area of research considering the existing MOCVD work.

A detailed review of published literature on the $\text{Al}_x\text{Ga}_{1-x}\text{P}/\text{Si}$ system suggests that current understanding of the effects of additions of Al to this ternary on the mode of nucleation is vague. In addition, a detailed examination of III-V/Si nucleation by MOMBE has not yet been published nor has AlGaP been grown on Si by MOMBE.

The present work is detailed in the following five chapters. In chapter 2, the growth techniques employed in the fabrication of the $\text{Al}_x\text{Ga}_{1-x}\text{P}$ deposits on silicon are discussed along with the analytical techniques used to characterize the various films.

Chapter 3 details the procedures used to prepare the epitaxial silicon substrates for $\text{Al}_x\text{Ga}_{1-x}\text{P}$ deposition. Wafer preparation consists of removing the native oxide on the silicon wafers by a wet etching technique. The effects of varying the ex-situ etch solution volume ratios and substrate exposure times are discussed and correlated with the resulting substrate surface roughnesses. In addition, results of the quantification of heterointerfacial oxygen concentration of subsequently grown GaP/Si structures are presented and related to the wafer preparation conditions.

In Chapter 4, the initial stages of growth of the $\text{Al}_x\text{Ga}_{1-x}\text{P}/\text{Si}$ system grown by MOMBE are presented and discussed. The severity of the three-dimensional island nucleation of the ternaries is shown to be controlled by growth temperature as well as

composition and group V flow. Precursor decomposition and gettering mechanisms are used to explain the change in island sizes from a single island size distribution to a bimodal one.

Chapter 5 details the procedures used to obtain the optimum conditions of the $\text{Al}_x\text{Ga}_{1-x}\text{P}$ buffer layer. The defects in the islands, thick $\text{Al}_x\text{Ga}_{1-x}\text{P}$ films and the buffer layer/GaP films are discussed. The dominant defects in all of the structures grown were found to be planar defects believed to result from stacking errors on the $\{111\}$ facets of the growing islands. And finally, the SIMS analysis of oxygen and carbon contamination in the thick films is discussed.

In chapter 6, a summary of the important conclusions is drawn from this study is provided along with recommendations for future research in this area.

CHAPTER 2

EXPERIMENTAL TECHNIQUES

The $\text{Al}_x\text{Ga}_{1-x}\text{P}$ in these experiments was grown using a metal-organic molecular beam epitaxy (MOMBE) system located in the Microfabritech facility at the University of Florida. The deposits were analyzed by several characterization techniques including cross-sectional transmission electron microscopy (XTEM), atomic force microscopy (AFM), secondary ion mass spectrometry (SIMS) and electron probe microanalysis. The MOMBE growth conditions employed as well as the important considerations and procedures pertaining to this growth technique and to the various characterization techniques mentioned above are outlined in the following chapter.

2.1 Metal Organic Molecular Beam Epitaxy

Metal-organic molecular beam epitaxy has become a powerful growth technique that has been instrumental in making possible several advances in electronic and photonic materials technology. Such examples include very high p-type doping capabilities of GaAs through the use of strongly bonded alkyls [48] and extremely high quality $\text{Ga}_{0.47}\text{In}_{0.53}\text{As}/\text{InP}$ quantum wells [49]. Growth using MOMBE has many advantages including: (i) ability to grow uniform ultrathin layers in a controllable and reproducible fashion, (ii) excellent control over thickness, selectivity and compositions, (iii) reduced oval defect densities, (iv) availability of in situ characterization equipment such as RHEED and modulated mass spectroscopy, (v) ease of source replenishment [43] and (vi) potential for scale-up.

MOMBE is a hybrid deposition technique that utilizes key components found in molecular beam epitaxy (MBE) and metal-organic chemical vapor deposition (MOCVD) systems. A comparison of some of the features in MOCVD, MOMBE and MBE deposition techniques are shown in Table 2.1.

Table 2.1. Relationship between various epitaxial techniques

<u>Technique</u>	<u>Sources</u>	<u>Pressure (Torr)</u>	<u>Flow Regime</u>
MOCVD	↑	760	↑ viscous flow
LPMOCVD	gas sources	$100-10^{-2}$	↓ ↑ 10^{-3} Torr
MOMBE	↓	$\leq 10^{-5}$	molecular flow
MBE	solid sources	$\leq 10^{-9}$	↓

Because of the variation in growth pressure regimes and precursor species, the kinetics of growth for each deposition technique are quite different. Deposition in MOMBE and MBE occurs in a high-vacuum environment such that the sources arrive at the heated substrate as molecular beams and thus do not react or collide before arrival. Under pressures of $\leq 10^{-3}$ Torr, the mean-free paths between molecular collisions become longer than the source inlet and substrate distance (≈ 14 cm for MOMBE), and source transport becomes collision-free. MOMBE has excellent controllability in epilayer thickness and composition through the use of mass flow controllers to control beam fluxes, while the use of gas sources increases precursor options for difficult to grow compounds.

The chemistry in MOMBE is more complex than in MBE, but the situation is simpler than in MOCVD where the presence of a boundary layer and the simultaneous involvement of gas- and adsorbed-phase reactions introduces additional complexities. In atmospheric MOCVD, the group III alkyls in a gas stream of H_2 undergo partial dissociation. They then diffuse through a stagnant boundary layer above a heated substrate and further dissociate into atomic group III elements as illustrated in Figure 2.1. The group III adatoms migrate to the appropriate lattice sites and deposit epitaxially by combining with a group V atom on the heated substrate surface. The growth rate is found to be limited by the diffusion rate of the group III alkyls through the boundary layer at normal growth temperatures and at low temperatures it is limited kinetically by the rate of pyrolysis of the precursors as shown in Figure 2.2. The growth mechanisms in MOCVD however, make it difficult to grow abrupt doped layers and to accurately deposit very thin films. In MOCVD, gas-phase (parasitic) reactions between some selected reactants can also occur and while beneficial to aid in the removal of unwanted impurities, can lead to poor incorporation efficiency and nonuniform growth.

In MBE, the group III atomic beams impinge on the heated substrate surface, migrate into the appropriate lattice sites, and deposit epitaxially in the presence of excess group V species. The growth rate is determined by the arrival rate of the group III atomic beams, since the sticking coefficient of the group III atoms on the substrate surface at typical growth temperatures is practically unity. Since the group III atoms at the substrate surface are generated by thermal evaporation from solid elemental sources, there are no chemical reactions involved in their derivation. The group V elements are normally in excess, which still gives stoichiometric material at normal growth temperatures for As- and P-containing materials since the group V elements are volatile, so the excess evaporates from the surface. MBE allows for the growth of abrupt junctions and well defined superlattice layers; however, there is still some difficulty with the growth of phosphorus

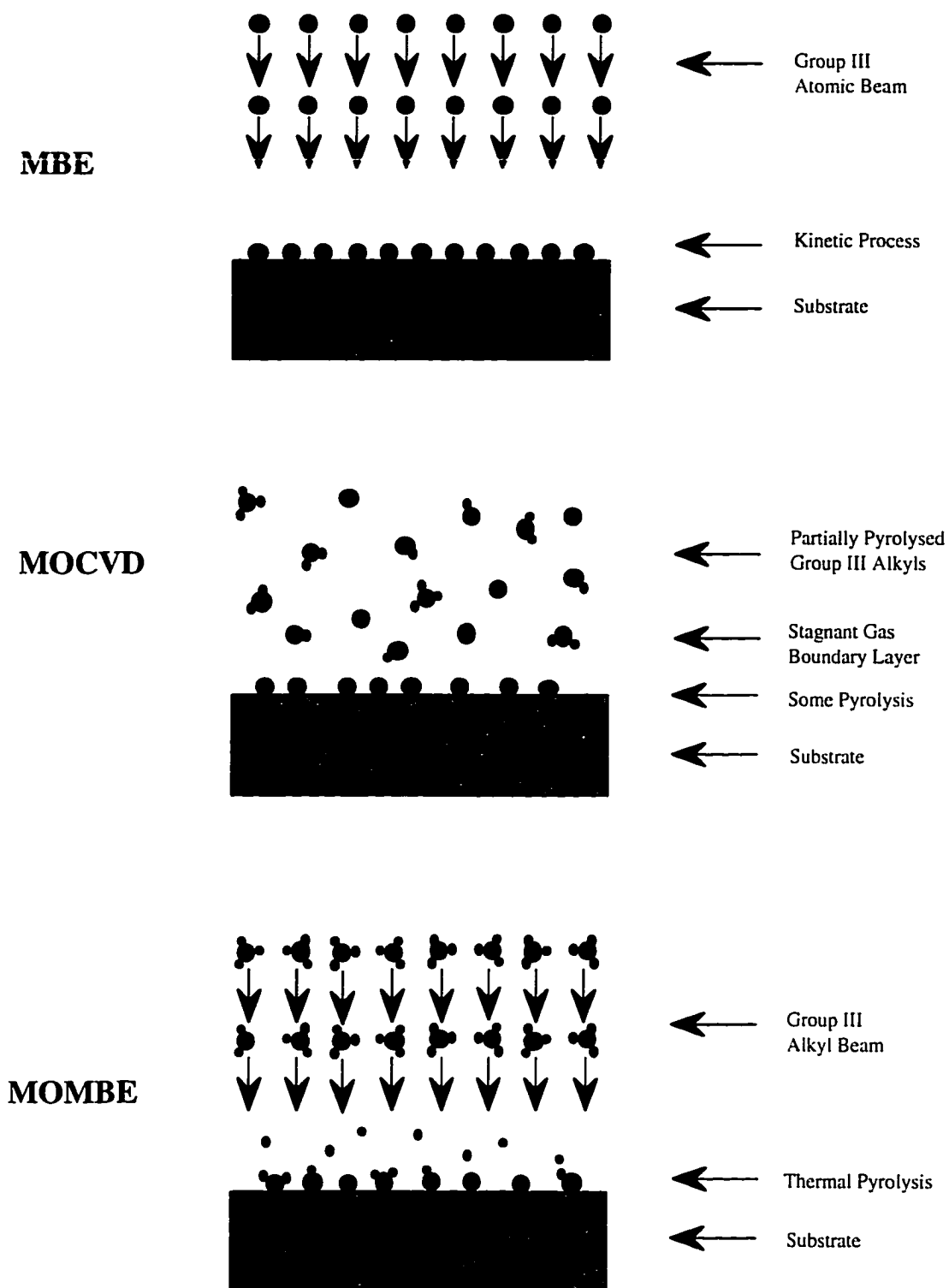


Figure 2.1 Precursor arrival and reactions depend on deposition technique.

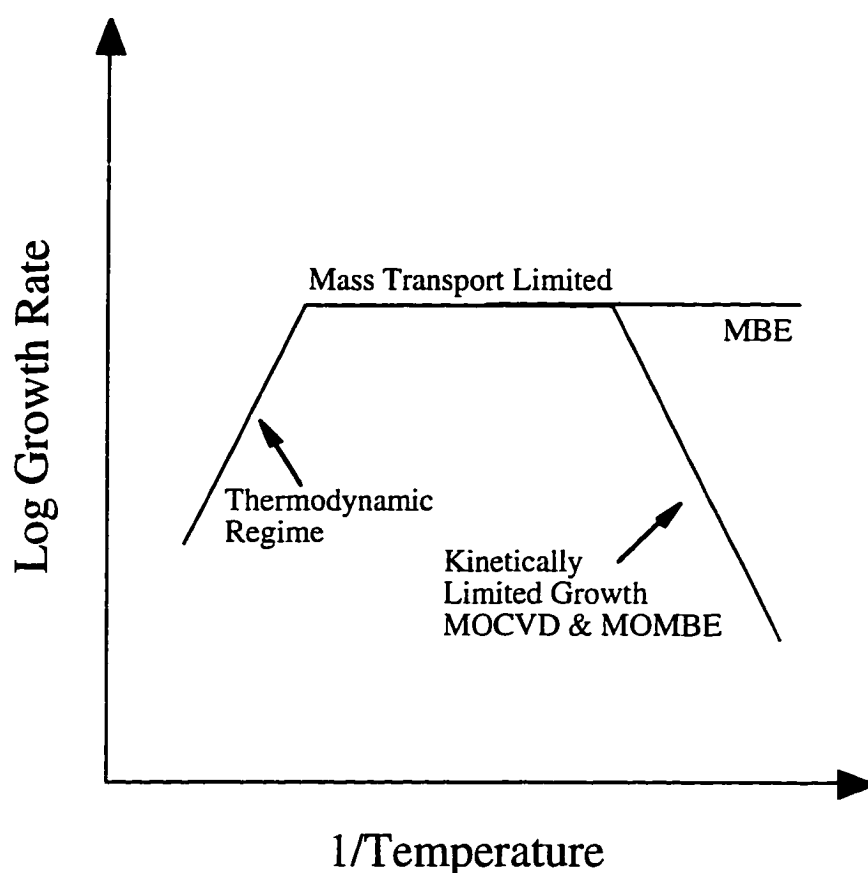


Figure 2.2 Schematic Arrhenius plot of growth rate versus temperature for MBE, MOCVD and MOMBE.

containing compounds and with film defects associated with using elemental group III sources [50].

In MOMBE, the group III molecular beam impinges directly onto the heated substrate surface as in MBE. However, there are no boundary layers for the group III source to diffuse through to get to the substrate surface, nor are there molecular collisions because of the long mean-free path of the molecules. Thus, after a group III metal-organic (MO) molecule strikes the substrate surface, it can either acquire enough thermal energy from the heated substrate to completely dissociate leaving the elemental group III atom on

the surface, or re-evaporate undissociated or partially dissociated. The particular dissociation process that occurs depends on the substrate temperature and the chemistry of the MO molecules. Therefore, the growth rate is dependent on the substrate temperature and reflects the physical and chemical conditions on the substrate surface. There is no definitive model available for an understanding of MOMBE growth kinetics at this stage. However, simple models have been proposed by several groups for GaAs MOMBE growth using triethylgallium (TEG) as a source material [51,52] as will be discussed in Chapter 4.2. These models provide a useful physical insight into the nucleation and growth process in MOMBE.

MOMBE source replenishment and switch-out is facilitated by the use of MO sources that are external to the main chamber and are introduced into the growth chamber via injectors as shown in Figure 2.3. Elemental sources can also be added to the system but require that the chamber be brought up to atmospheric pressure similar to procedures for source replenishment on MBE systems. Because of the high vacuum environment, in situ characterization equipment such as RHEED is often used in the growth chamber of MOMBE or is incorporated into a cluster tool system.

2.1.1 Description of the MOMBE System

The system used to grow the $\text{Al}_x\text{Ga}_{1-x}\text{P}/\text{Si}$ samples was a Varian Gas-Source Gen II MOMBE. The group III stainless steel bubblers were housed in a gas manifold cabinet and maintained at or below room temperature using temperature controlled recirculating baths. The baths were used to regulate the partial pressure of the source vapor and to control the temperature within $\pm 2^\circ\text{C}$. The precursors used for the growth of the $\text{Al}_x\text{Ga}_{1-x}\text{P}$ were triethylgallium (TEG), dimethylethylamine-alane (DMEAA) and precracked phosphine (PH_3). Properties of these precursors are shown in figure 2.4 and justification for their usage is explained in section 2.1.3. The TEG and DMEAA bubblers were maintained at 11.9 and 9.4°C respectively. Typical group III precursors have low room-

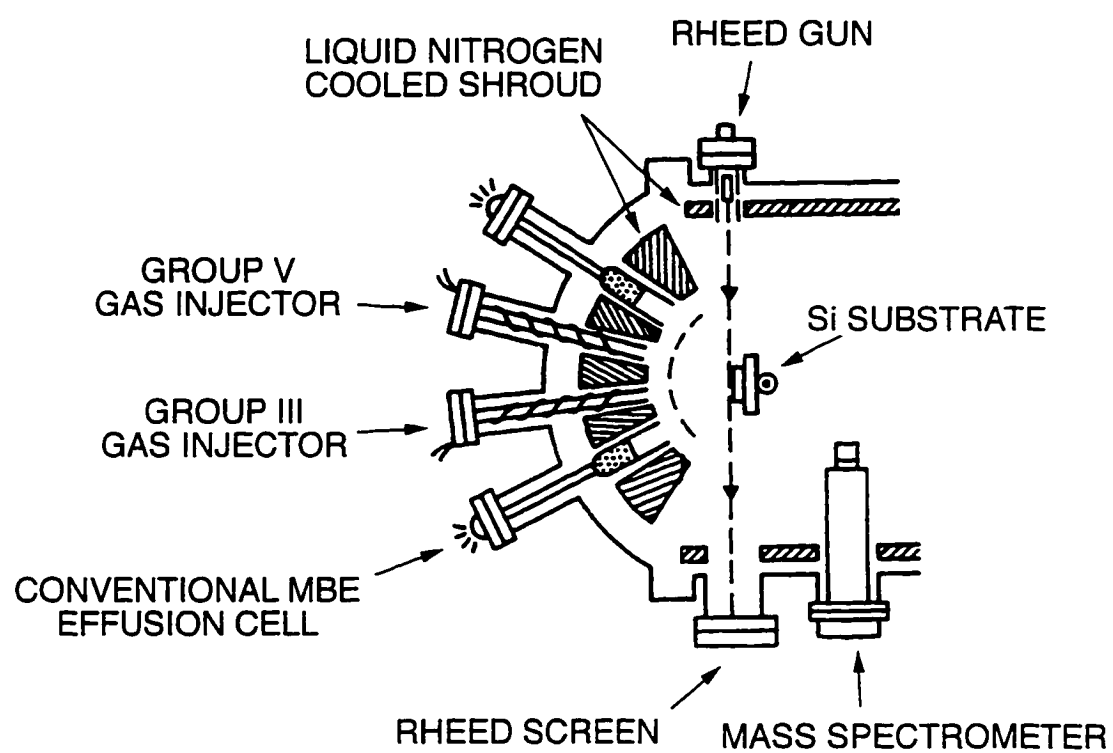
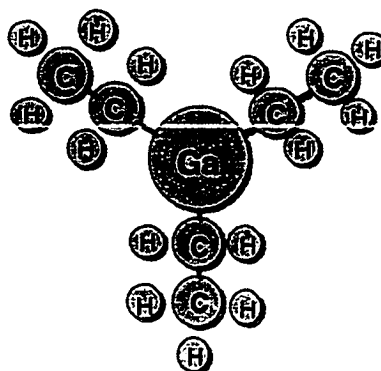


Figure 2.3 Schematic diagram of a typical MOMBE growth chamber.

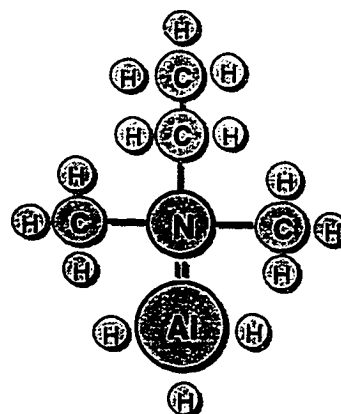
TEG

- VP@11.9°C=3.12Torr
- less C & O than TMG



DMEAA

- VP@T_{rm}=1.5Torr
- liquid
- no Al-C bond



PH₃

- catalytically cracked at 1000°C



Figure 2.4 AlGaP precursors and their properties.

temperature vapor pressures so that a carrier gas, such as H_2 , is used to extract the reagent from the bubblers. Mass flow controllers (MFCs) were used in conjunction with purified hydrogen carrier gas to regulate the transport of the group IIIs to the injector in the main growth chamber. The composition of the AlGaP was varied by changing the flow rates of the group III beams. The MFCs were placed upstream from the source bubblers to avoid decomposition and subsequent clogging in the mass flow sensor as shown below.

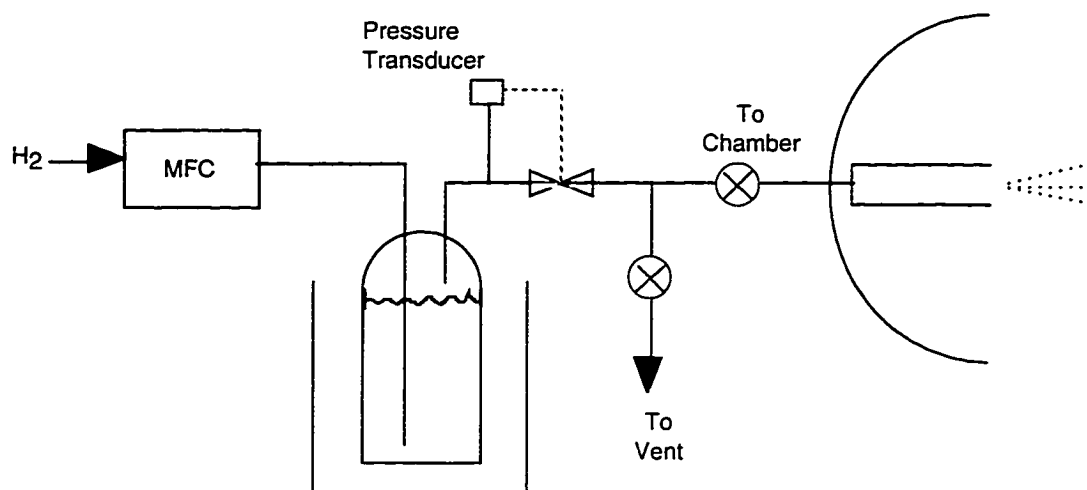


Figure 2.5 Mass-flow controlled manifold with MFC located upstream of MO source.

While the chillers provided a constant group III vapor pressure, a pressure controller maintained a constant group III-to- H_2 ratio under different H_2 flow rates. The flux of group III MOs arriving at the substrate surface was determined by the total pressure according to the following reaction [50]:

$$F_{MO} = \frac{F_{CG} P_{MO}}{P_T - P_{MO}}$$

where F_{MO} and F_{CG} are the flow rates of the MO and carrier gas respectively, P_{MO} is the vapor pressure of the MO, and P_T is the bubbler pressure.

In MOMBE, the MOs do not undergo decomposition until they interact with the heated substrate. Therefore, a single low-temperature (65°C) group III injector is all that is needed for the injection of the precursors into the growth chamber. A temperature of 65°C is used to minimize the condensing of any MOs on the inside of the injector as a higher temperature might decompose the weakly bonded sources such as the alanes.

For the high-pressure phosphine, the mass-flow control manifold consists of a source cylinder, located outside the Microfabritech building in an exhausted enclosure, a source regulator and a mass-flow control unit. The source regulator was used to regulate the phosphine and pressurize the line to a pressure of 8psi. Because of the low group V flows used in MOMBE, the phosphine bottle had to be opened only once at the beginning of the day. The pressurized phosphine in the line was sufficient for an entire day of growth. A mass flow control unit was used to regulate the flow of phosphine into the chamber where the precursor was catalytically cracked at 1000°C. A low pressure cracker ($\approx 10^{-3}$ Torr) as shown in figure 2.6, was used to decompose the phosphine to provide a beam of primarily P_2 molecules that would interact at the heated substrate surface. Tantalum aided decomposition in the cracker has been reported to aid in the efficiency of the cracker for PH_3 at 900 to 1000°C [53] leading to predominantly dimers.

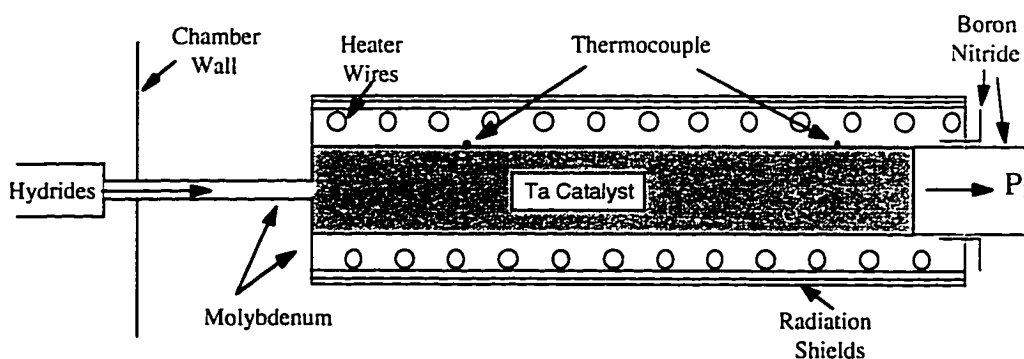


Figure 2.6 Schematic of a low pressure thermal cracker [53].

2.1.2 MOMBE Safety

Safety precautions are necessary in the use of highly toxic reactive materials found in MOMBE technology. Most of the MOs are pyrophoric compounds. Fumes resulting from the MO decomposition may cause skin and eye irritation and should not be inhaled. MOs are not a major risk to people provided that sensible precaution is taken in their handling and use. However, group V hydrides such as phosphine (PH_3) are very toxic and require that strict safety precautions be used. PH_3 affects the nervous system at a level of 300ppb [54] requiring that it be stored in isolated, exhausted cabinets. The exhaust from the main growth chamber contains many toxic chemical species that are potentially harmful to the environment. MOMBE exhaust is therefore decontaminated in a scrubber system before it is vented into the atmosphere. To protect the safety of the individuals working with and around the growth system, the entire Microfabritech building that houses the MOMBE is constantly monitored for toxic gas leaks by an MDA detector. If any leaks are detected, an audible/visual alarm will notify the occupants to immediately evacuate the building and all pneumatic valves on the growth system will be automatically switched to the off position to minimize any further escape of the gases.

2.1.3 AlGaP Precursor Selection

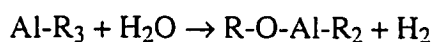
The selection of precursors for semiconductor growth by MOMBE is not a trivial task. Because MOMBE is a fairly new deposition technique, few source materials have been thoroughly researched. It was originally thought that the precursors used in MOCVD could be used in MOMBE. However, the high vacuum environment of MOMBE leads to very different precursor decomposition reactions leading to the development of specially designed precursors for MOMBE. Of the group III sources, some of the more widely used precursors include trimethylindium (TMI), triethylgallium (TEG) and trimethylamine alane (TMAAl). The most common group V sources are arsine (AsH_3) and phosphine (PH_3), although popular alternatives such as the tris-dimethylamino compounds (TDMAA and

TDMAP) are being researched to replace the extremely toxic group V hydrides. The ideal characteristics of a MOMBE precursor include: a vapor pressure of about 1 Torr at room temperature, high decomposition efficiency (low thermal stability), long shelf life, high purity, clean decomposition, low toxicity, and controllable kinetics.

2.1.3.1 Aluminum precursor

Dimethylethylamine alane (DMEAA) was used as the aluminum precursor for the deposition of $\text{Al}_x\text{Ga}_{1-x}\text{P}$ in these experiments as it has been shown to fulfill many of the requirements for MOMBE as well as having low impurity incorporation characteristics [55].

The first aluminum precursors explored for the growth of aluminum containing compounds in MOMBE were alkyls, i.e. trimethylaluminum (TMAI) and triethylaluminum (TEAI). These sources, although successful in MOCVD, proved to be unsatisfactory in the growth of AlGaAs and AlAs due to the high background concentrations of carbon and oxygen in the films [56]. It was shown that the strong Al-C bonds in the alkyls were responsible for the high carbon incorporation and ways to reduce the strength of the Al-C bond or eliminate it altogether were explored. One way to decrease the strength of a bond is to attach a large ligand to one side of the bond. For example, with the replacement of the methyl ligands (CH_3) in TMAI for ethyl ligands (C_2H_5) as in TEAI, the Al-C bond is weakened and the amount of carbon in the Al containing films is found to decrease. In addition to carbon, oxygen is a common impurity associated with the use of aluminum alkyls. Aluminum is a very reactive element and when exposed to oxygen it rapidly reacts. Both TMAI and TEAI can form volatile Al-O species upon exposure to water vapor or other sources of oxygen. The oxygen atom inserts between the alkyl group and Al as shown the following chemical reaction:



where R is an alkyl ligand such as CH_3 or C_2H_5 and R-O-Al-R_2 is an alkoxide [50]. It is virtually impossible to remove the alkoxide from the source once this occurs as the molecules appear and behave very similar to the metalorganics themselves resulting in oxygen incorporation into the film.

In an attempt to obtain lower impurity concentrations in semiconductor thin films, a variety of new aluminum containing precursors have been developed [57]. The most successful of which are the alanes. Both TMAA and DMEAA have been shown to be excellent replacements for the alkyl aluminum sources [55]. With the alane sources, the Al-C bond has been eliminated and replaced with a hydrogen bonded source which is coordinately saturated with an amine. This has lead to a dramatic decrease (up to three orders of magnitude) in the carbon concentration in AlGaAs films [50]. Additionally, the alanes do not form volatile Al-O species resulting in a marked reduction in the oxygen background in AlGaAs ($10^{21}/\text{cm}^3$ for TEAl versus $10^{16}/\text{cm}^3$ for TMAA).

The technological disadvantage of TMAA precursor is that it is a solid. The problem with solid sources is that they must be synthesized with ether which leads to oxygen contamination of the source. Solids also suffer from having two forms, bis and mono, making the vapor pressure of the solid variable. By increasing the size of a ligand in a molecule such as TMAA the source can be made a liquid. In DMEAA, a methyl group is replaced by an ethyl group making it a liquid. In principle, DMEAA should not alter the reaction kinetics or impurity background because of its similarity to TMAA, which has been verified by Abernathy et. al [55]. DMEAA can give less oxygen depending upon the TMAA source and Al mole fraction.

The DMEAA used for these experiments was obtained from Air Products and Chemicals Incorporated, and was a high purity grade. DMEAA has a vapor pressure of 1-2 Torr at room temperature. Decomposition of DMEAA on the heated substrate occurs by

the breaking of the Al:N bond followed by the rapid decomposition of the AlH_3 to an Al adatom.

2.1.3.2 Gallium precursor

TEG was used as the gallium precursor for the deposition of $\text{Al}_x\text{Ga}_{1-x}\text{P}$ in these experiments as it has been shown to help lower carbon levels in resulting films and allow for lower growth temperatures to be employed as compared to TMG. An empirical rule for metal organic compounds is that the metal-carbon bond strength decreases as the number of carbons bonded to the central carbon increases [27]. Thus, the bond strength decreases in the order methyl > ethyl > propyl > butyl. For MOMBE growth of device quality films, a major concern is the amount of residual impurity, especially carbon, resulting from the decomposition of the MO source materials. Since there are no gas phase reactions in MOMBE to reduce impurity incorporation, as in MOCVD, precursors must have lower metal-carbon bond strengths. The problem of carbon contamination from TMG can be avoided by using a less stable TEG thus leading to carbon background levels as low as $10^{14}/\text{cm}^3$ in GaAs [58]. Carbon has been observed to be a predominantly p-type contaminant in GaAs and GaP incorporated into the group V lattice site and has been found to be strongly affected by the growth temperature [54] and the V/III ratio [59]. Abernathy et al. [59] postulated that the reduction in carbon incorporation in GaAs with increased V/III was due to the increase of $(\text{C}_2\text{H}_5)_x\text{As}$ formation and subsequent removal from the surface.

The decomposition of TEG has been studied by Robertson et al. [51] in the growth of GaAs and will be discussed in detail in Chapter 4. Growth studies of GaP using TEG and PH_3 [60] in a CBE system show that the overall behavior of the GaP growth rate as a function of substrate temperature is qualitatively similar to that of the growth of GaAs using TEG and AsH_3 . The growth rate is typically linearly dependent on the TEG flux for

normal growth conditions. TEG pyrolysis begins at approximately 380°C and significant desorption of Ga species occurs at temperatures >550°C.

2.1.3.3 Phosphine precursor

Hydrides such as phosphine are commonly used as group V precursors. They are available in standard high-pressure gas cylinders with megabit purity and are fairly reasonably priced. Due to the low group V flows used in MOMBE, a 100g cylinder should last several years. The toxicity of phosphine however, is very high and the need to use high-temperature catalytic crackers has spurred the search for alternative phosphorous sources. Several choices are now available such as TDMAP and tertiarybutylphosphine [61], however these have not been explored in these experiments.

2.1.4 AlGaP Growth Parameters

One of the advantages of MOMBE is the ability to grow device structures that require monolayer precision control. This is achieved by using a vent/run gas-switching system that eliminates any flow transients allowing for very fast switching speeds. The success of this technique relies on the establishment of a stabilized gas flow into a low pressure vent line prior to switching into the run line. Growth is initiated by introduction of the stabilized gas flow in and out of the growth chamber rather than opening and closing the source containers. Control over the gas flow to this precision was needed for repeated deposition of the $\text{Al}_x\text{Ga}_{1-x}\text{P}$. In order to study the early stages of growth in the $\text{Al}_x\text{Ga}_{1-x}\text{P}/\text{Si}$ system, approximately 50Å of material was deposited on the epitaxial silicon substrates for each composition and growth temperature.

On-axis epitaxial silicon (001) substrates (ESS) were used in these experiments. Prior to MOMBE growth, the silicon wafers had to be prepared for deposition. Substrate preparation consisted of a native oxide removal step through the use of a wet chemical solution. The nucleation studies were all performed on wafers treated in diluted DI:HF

(50:1 volume) solutions for 15s, followed by a DI rinse for 15s and a nitrogen dry. Variations of DI:HF volume ratio, etch and rinse times were studied to examine their impact on carbon and oxygen contamination at the III-V/Si heterointerface. In addition, buffered oxide etch (BOE) with and without surfactant was used to compare the interfacial impurity removal efficiency. The HF acid used was 48% purchased from Fisher. Detailed analysis of the silicon substrate cleaning efficiencies for each etch solution is presented in Chapter 3.

The wafers were In-free mounted onto Mo-block substrate holders and loaded onto a trolley system that could be transported from the loadlock chamber to the buffer chamber through the use of magnets. Transfer rods were used to move the substrate holders onto the substrate heater in the main growth chamber. Individual wafers were loaded one at a time into the growth chamber for deposition. Wafer rotation was utilized to maintain film thickness uniformity (15rpm) and a calibrated optical pyrometer was used to monitor substrate temperature. During wafer heat-up the wafers were exposed to a P_2 beam.

The composition of the $Al_xGa_{1-x}P$ was varied from $x=0$ to 0.7 to study the effect of Al on the characteristics of nucleation. In addition, three different growth temperatures were explored (450°, 500°, and 550°C) to establish the effect of temperature on the initial stages of $Al_xGa_{1-x}P/Si$ growth. The composition of the $Al_xGa_{1-x}P$ was determined by electron microprobe analysis from thick films $\geq 1\mu m$. The growth rates of the ternaries were kept constant for each growth temperature and are shown for each composition in table 2.2.

The growth rates were found to increase almost linearly with increased flows of DMEAA at a constant flow of TEG (0.5sccm) as shown in figure 2.7. At growth temperatures of 500 and 550°C, the aluminum flows needed for growth of the ternaries was greater than those at 450°C due to desorption effects. Therefore the TEG flow was decreased slightly in order to keep the V/III ratios fairly constant.

The pressure during growth was on the order of 5×10^{-5} Torr and 1×10^{-5} Torr for the deposition of $Al_xGa_{1-x}P$ and GaP respectively. Pressure in the growth chamber was

Table 2.2 Growth rates for selected $\text{Al}_x\text{Ga}_{1-x}\text{P}$ compositions.

Composition (%Al)	Growth Rate ($\mu\text{m/hr}$)
0	1.14
15	0.9
30	1.18
45	1.43

maintained through the use of a Balzers turbo pump and a C778 cryopump. Conventional ion pumps used in MBE cannot be used to handle the gas load from a MOMBE because the of the excess hydrogen produced by the hydride decomposition and the use of carrier gas for the group IIIs.

Bakeouts of the MOMBE were performed to remove oxygen that accumulated during system repairs when the growth chamber is brought up to atmospheric pressure. The bakeout of the entire system lasts for 72 hours at a temperature of approximately 150°C .

2.1.5 Pyrometer Calibration

In MOMBE growth it is essential to know the substrate temperature to a high degree of accuracy as the kinetic processes that lead to growth strongly depend on temperature. Thermocouple temperature measurements from the indium-free mounted wafers do not truly represent the temperature of the substrate [62]. Thus, optical pyrometers are often used to monitor the substrate temperature. However, pyrometers need to be calibrated for a particular operating temperature regime for best results. In these experiments, the melting

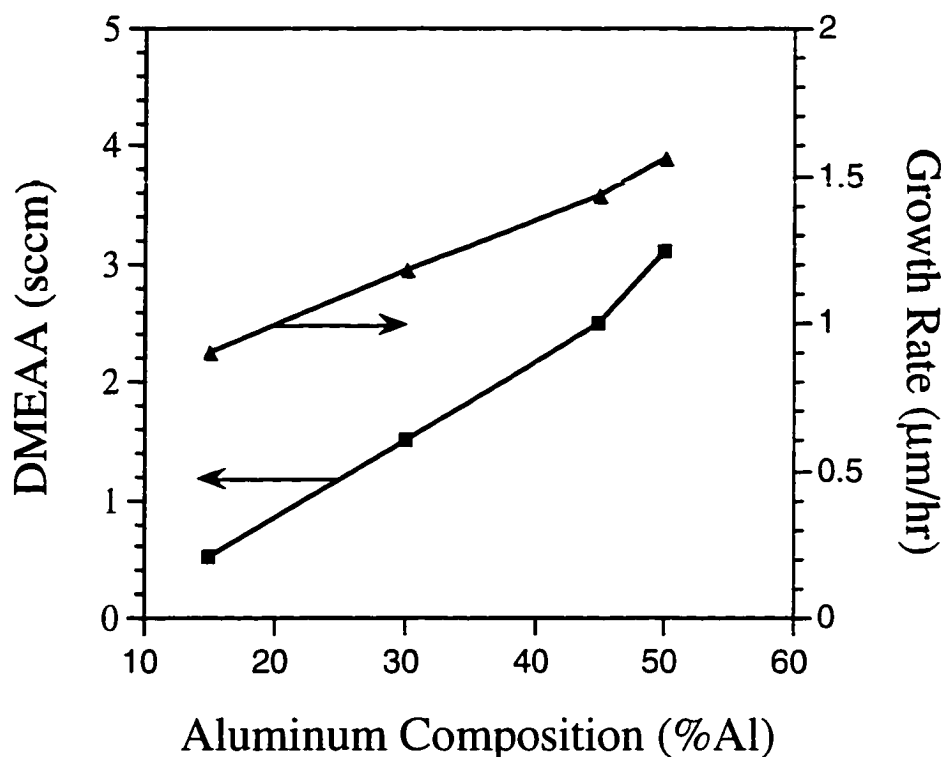


Figure 2.7 Flows of DMEAA needed for various $\text{Al}_x\text{Ga}_{1-x}\text{P}$ ternaries and their respective growth rates under constant flows of TEG (0.5sccm) and PH_3 (2sccm).

point of a piece of InSb was used as a reference temperature. The InSb was visually monitored through a view port on the growth chamber as the substrate temperature was raised to the melting point of the binary ($520 \pm 5^\circ\text{C}$). When InSb became a liquid, the pyrometer was calibrated to read 520°C .

Optical pyrometer measurements were made using a Inficon pyrometer. Light was collected through a shuttered pyrometer port window and the measured spot size on the sample was $\approx 2.5\text{cm}$ in diameter with the pyrometer to substrate distance being $\approx 14\text{cm}$. Pyrometer readings are very dependable as long as care is taken to minimize pyrometer errors including stray light and the coating of pyrometer windows [62,63]. Using an

optical pyrometer, the substrate temperature can be accurately estimated to within $\pm 10^{\circ}\text{C}$ [64].

2.2 Transmission Electron Microscopy

The majority of the TEM analysis in this work was done using a JEOL 4000FX high resolution transmission electron microscope (HRTEM). A schematic of the microscope is shown in figure 2.8. The electron source for the HRTEM is a LaB_6 filament that emits an electron beam which is focused on the sample using a set of condenser lenses. The sample is held in a double tilt stage that is just above the objective lens system. This lens system collects the transmitted beam exiting from the sample and forms an image at the objective image plane and a diffraction pattern at the objective back focal plane. The image and the diffraction pattern can then be suitably magnified and projected onto the viewing screen by means of an intermediate and projector lens. Objective apertures at the objective back focal plane can be used to select particular diffracted beams for imaging, such as a two-beam condition. Diffraction from selected small areas may be observed using the selected area aperture located at the objective image plane.

Contrast in high resolution images arises through phase differences in the electron beams as they pass through the thin sample. For phase contrast to be important, some or all of the electrons scattered by the specimen must pass through the objective aperture and be recombined with the unscattered electrons to produce intensity differences from point to point in the image. The detail resolvable in a high-resolution phase contrast image will depend upon the phase changes introduced into the scattered electrons by the specimen.

The instrument has a point-to-point resolution of about 1.9\AA . The microscope can be operated at voltages between 100–400kV and was operated exclusively at 400kV for this work.

A small part of the work was done using a JEOL 200CX tungsten filament 200kV TEM with a point-to-point resolution of 2.3\AA . This microscope was used to image thick

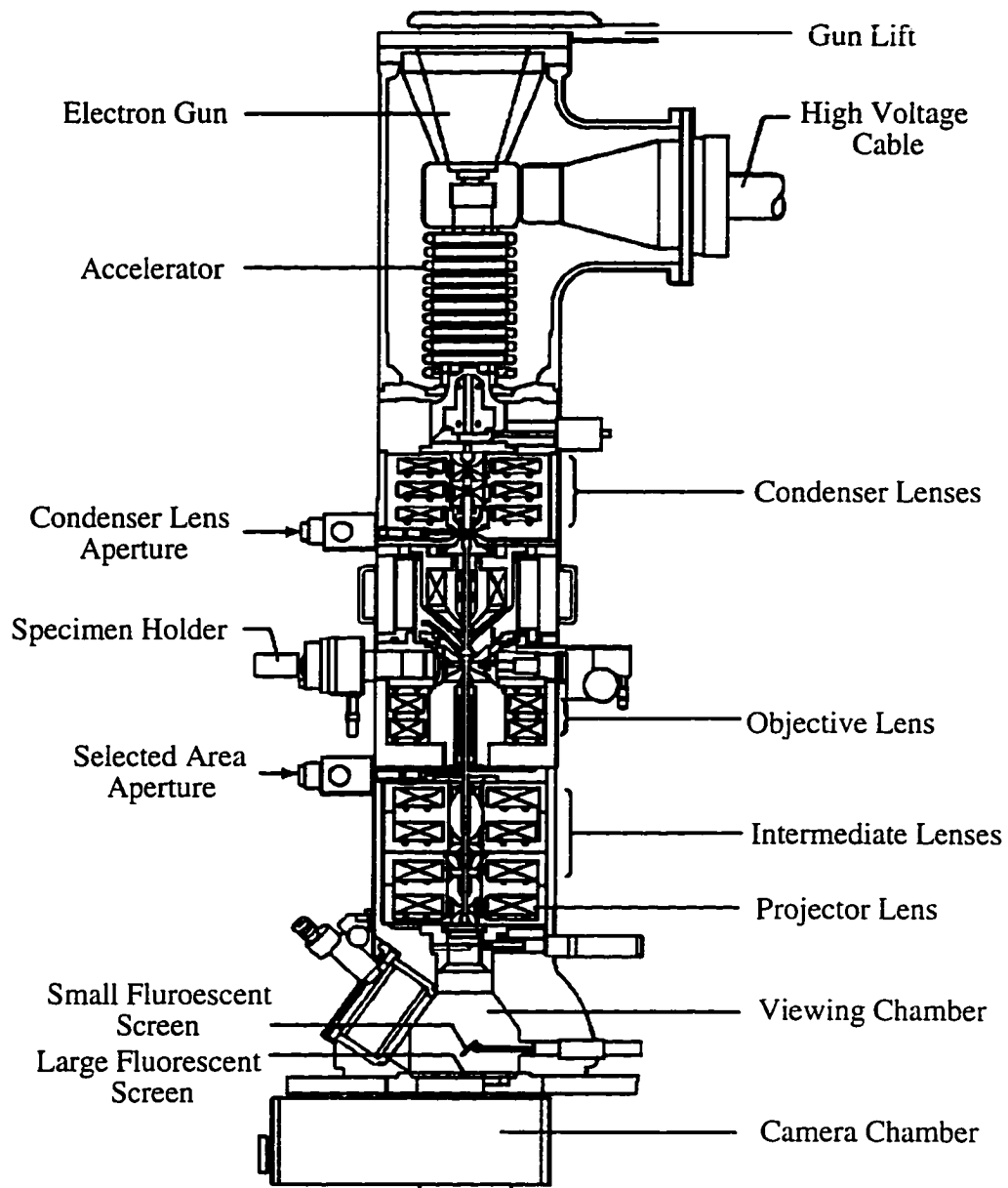


Figure 2.8 Cross-sectional schematic of a JEOL 4000 HRTEM.

GaP and $\text{Al}_x\text{Ga}_{1-x}\text{P}$ films using g_{220} and g_{400} two-beam conditions for enhanced contrast of film defects. In addition, the thickness of the films was determined from TEM using on-axis conditions.

Specimen preparation for TEM is a complicated and delicate procedure that tends to be categorized as an art rather than a science. For thin films studies, there have been two popular geometries of sample observation; the plan view and the cross-sectional view. In the cross-sectional geometry, the interface is parallel to the direction of the electron beam so that the sample is viewed edge-on, and in plan view the beam is perpendicular to the interface. For these experiments, the view of most interest was cross-sectional as AFM acquired most of the information relative to the plan view. XTEM was used to study the island evolution, geometry and interfacial characteristics at the initial stages of growth as well as defect formation in both the islands and thick films.

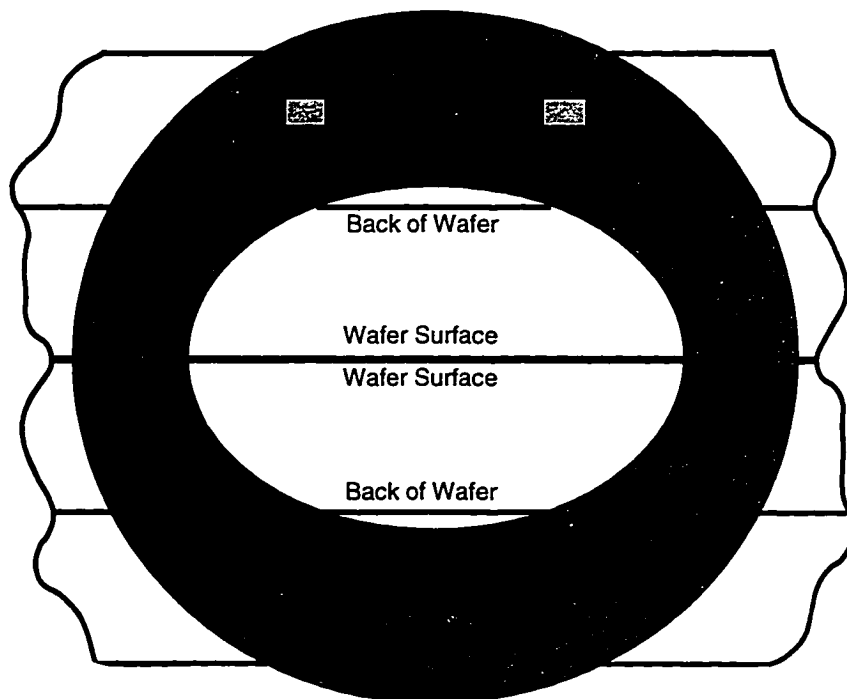
XTEM sample preparation consisted of cutting the as-grown wafers into 10 mil thick strips using a Micro Automation Inc. dicing saw, and glueing the strips together with G1 Epoxy in the order as shown in figure 2.9.a. The epoxied strips were then mechanically polished to a thickness of $\leq 50\mu\text{m}$ using a $5\mu\text{m}$ Al_2O_3 powder slurry and copper rings were mounted onto thinned specimens to provide mechanical support as shown in figure 2.9.b. The final thinning process was done using a Gatan ion mill via the sputtering action of two Ar^+ ion guns until the specimens were electron transparent. The optimum ion mill operating conditions were found to be a gun voltage of 4kV, a milling angle of 13-15°, and a gun current of 1mA.

2.3 Atomic Force Microscopy

Topographic information of the $\text{Al}_x\text{Ga}_{1-x}\text{P}$ deposits was obtained using an AFM. Specimens grown to study the early stages of growth of the $\text{Al}_x\text{Ga}_{1-x}\text{P}$ on silicon as well as thick $\text{Al}_x\text{Ga}_{1-x}\text{P}$ films were analyzed in order to obtain feature densities, geometries and surface roughness.

Strip 1	Back of Wafer
	Wafer Surface
Strip 2	Back of Wafer
	Wafer Surface
Strip 3	Wafer Surface
	Back of Wafer
Strip 4	Wafer Surface
	Back of Wafer

a)



b)

Figure 2.9 XTEM Preparation Schematics a) 10mil strip configuration, and b) placement of copper ring for mechanical support.

The atomic force microscope was introduced in the mid 1980's by Binnig et al. [65] in response to the limitations of the scanning tunneling microscope (STM). Because STM requires the establishment of tunneling current between the STM tip and sample for operation, the only materials that can be imaged are those that conduct. However, AFM is capable of scanning insulating materials such as polymers and ceramics, and has become widely accepted since the first commercial AFM was introduced in early 1990. Many of the components found on a STM are also found on an AFM. This has been utilized by scanning probe microscope (SPM) manufacturers in the development of multimode SPMs that can be operated as STMs or AFMs. The differences between the microscopes are found in the probe and sensing systems.

An AFM uses a very sharp tip located very close to the specimen surface to measure the changes in cantilever deflection due to variations in topography. The tip, typically a couple of microns long and less than 100Å in diameter, is mounted to the free end of a cantilever 100-200µm in length. The cantilever is flexible with a spring constant less than that of the specimen in order to allow for cantilever deflection. Tip proximity to the specimen is such that it responds to weak attractive and repulsive forces dominated by van der Waals forces. When the tip is brought close to the sample surface, it experiences an attractive force. As the tip is moved closer to the specimen the attraction increases until the electron clouds of the tip and specimen begin to overlap and repel each other electrostatically. The van der Waals force goes to zero when the repulsive and attractive forces are balance. Beyond this point, the van der Waals force becomes repulsive and the atoms are considered to be in contact. In addition to the van der Waals force, the tip encounters two other forces: a capillary force exerted by a thin water layer often present in an ambient environment, and a force exerted by the cantilever itself. Cantilever deflection is typically monitored by way of a laser/photodiode detection system as shown in figure 2.10. The information obtained from the position-sensitive photodiode is used as feedback to maintain the vertical position of the tip by piezoelectric components. A system can detect

sub-angstrom vertical movement of the cantilever tip and is limited by vibrations and detector sensitivity. Vibration isolation was achieved by mounting the AFM on a pressurized air damping table. Piezoelectric scanners are also used to perform the high resolution raster scans in the X-Y plane parallel to the specimen surface in order to obtain the images. The data acquired from the AFM is quantitative and three-dimensional, and is commonly displayed in a surface plot with features shaded according to their height.

A Digital Instruments Nanoscope III Multimode SPM was used for these experiments. The microscope has the capability of operating in several common scanning modes including STM and AFM (both contact and tapping modes). Tapping mode AFM was used exclusively for this work as it does not lend itself to any alterations of the sample surface as is often found in contact mode AFM, and tapping mode AFM is capable of penetrating the inherent water layer on the specimen surface. The AFM cantilevers were made from etched silicon and had resonant frequencies of 60-400kHz. Typical settings for the *drive voltage*, drive amplitude, and drive frequency were 3-6V, 100-1500mV, and 300-400kHz respectively depending on the tip characteristics.

Scan sizes of 100, 25 and 1 μm^2 were taken to get a conclusive overview of the surfaces using scan rates of 1.5, 3, and 6 Hz respectively. The scan rate defines the number of fast scans (x-direction) made per second and should be set according to the expected specimen surface roughness. Image distortion can occur when the scan rate is too high as the tip does not have time to accurately scan the surface. A useful equation used to limit the scan rate is as follows:

$$\text{Scan Rate} \times \text{Scan Size} \times 2 \leq 30$$

Aspect ratios (island width/height) from the $\text{Al}_x\text{Ga}_{1-x}\text{P}$ islands were measured in XTEM as well as with AFM. The AFM sectional analysis software allowed for the examination of selected cross sections of height data from the scans where the island

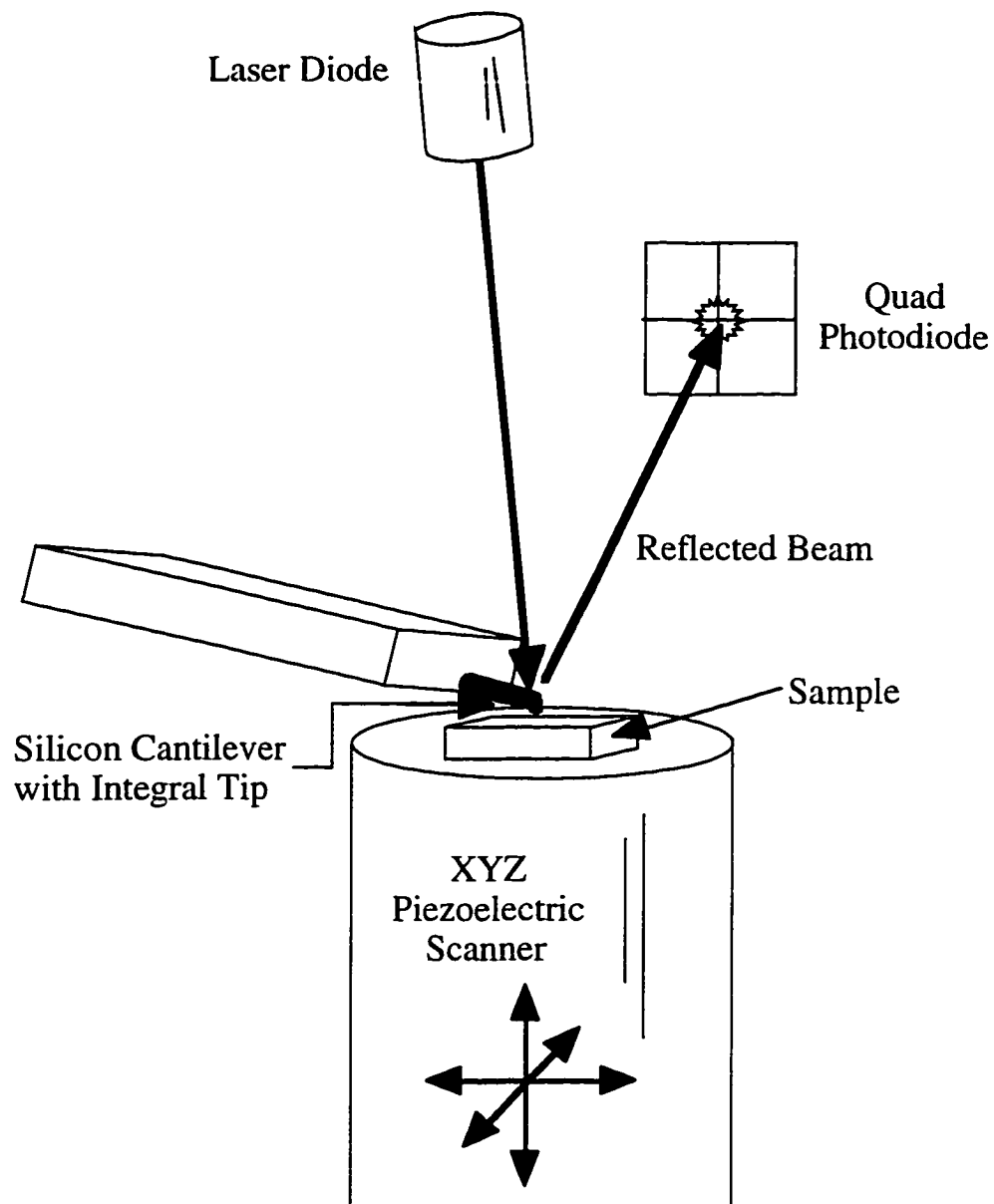


Figure 2.10 AFM scanning setup. Small vertical displacements of the specimen surface cause deflections in the laser reflection.

heights and widths could be read and an aspect ratio calculated. Surface roughness was calculated by the AFM software. The roughness values reported in this work are RMS values i.e. standard deviation of the height values, that was calculated using the following formula:

$$\text{RMS} = \sqrt{\frac{\sum (Z_i - Z_{\text{ave}})^2}{N}}$$

where Z_i is the current height value, Z_{ave} is the average of the height values, and N is the number of data points. In addition, the number of islands in a scan was calculated using the grain size analysis software. This data was obtained by defining a height threshold for a plane that sections the three-dimensional data at the defined height resulting in a plane of sectioned features (islands). The number and mean area of the sectioned islands within the plane were calculated by the computer for each height threshold.

For all scans, a planefit data filter (3rd order) and a flatten filter (zero order) were applied to the collected data using the AFM software prior to quantitative analysis. These filters remove scanning artifacts such as image bow by applying mathematical equations to the digital data and are used primarily to improve the quality of the image for display purposes. The data distortion using these two filters is minimal as shown in table 2.3 and 2.4 for planefit and flatten filters respectively. However, additional filters supplied with the software, such as high pass and low pass filters, can cause severe data distortion and should be used only when deemed necessary. Once these filters are used on a sample they should, in general, be used on every subsequent specimen for fair data comparisons.

An often observed phenomenon in an AFM image are tip artifacts. This is recognizable in scanned images by a feature pattern that is repeated over and over again in the scan. Most often this is due to a tip that has lost its atomically sharp shape and is subsequently scanning with a blunt end. This makes its difficult to image specimen

Table 2.3 Applied AFM software filter effects on data for a) plane fit filter and b) flatten filter.

Plane fit Order	Number of Islands	RMS	Maximum Feature Height (nm)
none	2541	1.880	12.01
1	2544	1.880	12.01
2	2538	1.875	12.17
3 (max)	2542	1.875	12.17

a)

Flatten Order	Number of islands	RMS	Maximum Feature Height (nm)
none	2538	1.875	12.17
0	2537	1.875	12.17
1	2548	1.871	12.81
2	2548	1.862	12.93
3 (max)	2536	1.853	13.09

b)

features that are smaller than the blunt tip typically resulting in an image that contains the shape of the tip defect repeated every time the tip encounters these small specimen features. The data collected in this manner is erroneous and should not be used. If there is question as to what the surface really looks like, a new AFM tip should be tried or a different analytical technique such as SEM or XTEM should be applied for comparison.

2.4 Secondary Ion Mass Spectrometry

The background and interfacial concentrations of carbon and oxygen were analyzed by SIMS. This sensitive technique for chemical analysis allows for quantification of selected chemical species that are distributed within the sample. Depth profiling of the chemical species in the sample is accomplished through the use of ions such as Cs^+ and O^+ that sputter the specimen by bombardment in a high vacuum. Ion probing of a solid with a 1-10keV beam sputters off surface layers of the sample, producing a variety of secondary species including neutral atoms and molecules, secondary electrons, photons, and positive and negative ions. Chemical information about the sample is obtained through mass spectroscopy of both the positive and negative secondary ions. Mass spectrometry offers full elemental coverage from hydrogen to uranium with detectabilities as low as the ppb (atomic) range. SIMS is a destructive analytical technique such that in the process of gathering data the primary ion beam produces a crater in the sample. To prevent the collection of chemical information from the side walls of a crater, the primary beam is rastered over a selected area of the sample and mechanical aperturing of the secondary ion beam is used. This allows the analysis of only those ions from the bottom flat area of the crater to be analyzed and not those from the side walls.

In these experiments, a PHI 6600 Perkin Elmer SIMS was used to detect the carbon ($^{12}\text{C}^-$) and oxygen ($^{18}\text{O}^-$) in the thick GaP and $\text{Al}_x\text{Ga}_{1-x}\text{P}$ films. A focused energetic primary Cs^+ beam of energy 5keV was rastered over a square area of $300 \times 300 \mu\text{m}^2$ and

negative secondary ions were collected from an centered image area of about 30% of the original area ($90 \times 90 \mu\text{m}^2$).

The majority of the data presented in this work is in units of intensity (counts/second) because of the difficulty in creating standards for each composition of $\text{Al}_x\text{Ga}_{1-x}\text{P}$ grown. Thus the relative amounts of both carbon and oxygen are compared throughout the studies. Quantification of carbon and oxygen was carried out however in the GaP/Si and GaP/GaP samples using standard ion implants of C and O in GaP. Quantification of the SIMS profiles was accomplished by processing the raw data into concentration versus depth using PHI-Matlab data processing software. The relative sensitivity factors (RSFs) of C and O in GaP were calculated by using the concentration values of these species in the same GaP matrix as determined by Evan's East. The RSFs were calculated with reference to the $^{62}\text{P}^{2-}$ matrix ion. The depth of the craters sputtered into the samples was measured with a Dektak IIA profilometer after the SIMS analysis. An average of 5 measurements along the x and y directions were taken for each crater. The crater depth and sputter rate for each GaP/GaP sample are listed in table 2.3a. The relative sensitivity factors calculated with reference to a matrix ion are listed in table 2.3b.

The accuracy of the concentrations are expected to be within a factor of two except near the sample surface due to oxidation. Additionally, the accuracy in the concentration data near the heterointerface may be more uncertain due to the rapidly changing matrix composition resulting in interfacial areal densities with an uncertainty of a factor of three or four. Areal densities of the impurities at the interface have been estimated by numerical integration of the area in the concentration profiles.

2.5 Electron Microprobe

A JEOL 733 electron probe x-ray microanalyzer was used to determine the composition, x, of the $\text{Al}_x\text{Ga}_{1-x}\text{P/Si}$ samples (film thickness $\geq 1 \mu\text{m}$). Microprobe is a nondestructive quantitative and qualitative elemental analysis technique that measures

Table 2.4 a) Sputter rates for GaP/GaP sample quantification b) relative sensitivity factors calculated with reference to a matrix ion.

Sample File#	Sputter Time (min)	Crater Depth (Å)	Sputter Rate (Å/s)
Raster: 300µm			
CSGAP_10	4.6	4,708	17.07
CSGAP_3	12.8	12,832	16.71
CSGAP_4	11.7	11,805	116.82
Raster: 250µm			
CSGAP_9	3.3	4,724	23.87
CSGAP_2	8.8	12,611	23.88
CSGAP_5	8.8	12,824	24.29

a)

Reference Matrix 62P ₂ ⁻	CSGAP_10	CSGAP_9
H1 (H ⁻ /P ₂ ⁻)	4.59x10 ²⁰	3.83x10 ²⁰
C12 (C ⁻ /P ₂ ⁻)	1.03x10 ²¹	9.30x10 ²⁰
O16 (O ⁻ /P ₂ ⁻)	3.18x10 ¹⁸	3.30x10 ¹⁸

b)

characteristic x-rays emitted from a target. The physical basis of electron probe microanalysis is the generation of characteristic x-rays through the bombardment of a sample with energetic electrons. The x-rays are produced by way of ejection of core level electrons (inelastic scattering) followed by the de-excitation of higher level electrons in the films. The microprobe was operated in the wavelength-dispersive X-ray spectrometry (WDS) mode using an electron beam of 6kV. The detection limit for this system is on the order of 100ppm, with an error of $\approx \Delta x \leq 0.005$, and elements with atomic numbers >5 can be detected. Quantitative analysis is achieved by relating the concentration of a constituent in the unknown to the concentration in a standard in terms of the ratio of x-ray intensities generated in the target. GaP semiconductor wafers and Al metal were used as the standards for quantification. Values of concentration can be given in atomic or weight percent.

CHAPTER 3

SILICON WAFER PREPARATION

Preparation of native oxide free silicon surfaces for epitaxial deposition is a critical step in the growth process. It is imperative that the native oxide be removed prior to the deposition of the film material in order for single crystal growth to occur. A very thin oxide layer on the substrate surface can result in polycrystalline films and pockets of residual oxide on the substrate surface can lead to the formation of planar defects in the epilayer. The variations in silicon substrate preparation techniques are manifold. Some techniques utilize wet chemical etches to remove oxides and metals, while others may use plasmas for impurity removal. Certain methods are more efficient than others in removing specific surface impurities and minimizing substrate surface microroughness. However, due to the high reactivity of silicon, it is difficult to produce clean surfaces and to preserve them from unwanted contaminations. In this chapter some of the more common silicon substrate preparation techniques are reviewed and the results of the substrate cleaning techniques utilized in these experiments are discussed.

3.1 Wafer Cleaning Background

The objective in wafer cleaning is the removal of contamination from the wafer surface while maintaining substrate surface integrity. Contaminants on silicon wafer surfaces occur as films such as oxides or solvent residues, particles, adsorbed gases, metals and ionic materials. The sources for these impurities are abundant and include chemicals and their containers, production processes, and handling. These contaminants can cause a variety of adverse effects during subsequent processing that depend on the

nature of the impurity. For example, metallic impurities can increase current diode leakage, decrease oxide breakdown voltage and decrease minority carrier lifetime. The most tenacious of these metallic contaminants are Fe, Cu, Zn, Cr, and Ni, all of which show very fast diffusion even at low temperatures and can be detrimental to device performance in concentrations $>10^{10}/\text{cm}^2$ [66]. Particles on the surfaces of silicon wafers can also present problems during processing by blocking or masking areas in etching, deposition and photolithography steps.

For the fabrication of devices, it is essential to remove contaminants from the silicon surface that may reduce the final device performance, reliability and yield. It has been estimated that over fifty percent of yield losses in integrated circuit manufacturing are caused by contamination remaining on the silicon surface after cleaning [67]. A widespread approach for silicon preparation is the use of a thermal oxide desorption step to achieve a clean starting Si surface for deposition. The drawback to this approach lies in the requirement of high desorption temperatures which can lead to many deleterious effects such as doping profile redistribution, wafer warpage, and impurity diffusion and segregation. Therefore, low temperature silicon cleaning techniques are being developed. Substrate cleaning will continue to be an important step both in research and in device manufacturing especially as device geometries approach the sub-half micron dimensions [67]. For these studies however, the importance of removing surface impurities and particles was overshadowed by the requirement for the removal of the native oxide and establishing a suitable surface for epitaxial growth of AlGaP buffer layers.

Minimization of microroughness of the silicon surface as a result of wafer preparation and passivation of the wafer surface to enable it to remain clean for extended periods of time was also of interest. The effectiveness of surface preparation techniques can be characterized by several techniques including: X-ray photoemission spectroscopy (XPS), total reflection x-ray fluorescence (TXRF), secondary ion mass spectrometry (SIMS), high resolution electron microscopy (HRTEM), atomic force microscopy (AFM)

and high resolution electron energy loss spectroscopy (HREELS). The silicon surfaces and heterointerfaces in these experiments were examined by AFM, SIMS and HRTEM.

3.1.1 RCA Wafer Cleaning Process

The industry standard for silicon wafer cleaning is the RCA process [68]. Kern developed this process at RCA in 1965 for silicon device fabrication and in 1970 the cleaning process was published in the RCA Review [68]. The wafer cleaning chemistry developed by Kern has remained essentially unchanged in the past 30 years and is based on hot alkaline and acidic hydrogen peroxide solutions. The first of the two cleaning solutions is known as the RCA standard clean 1 (SC1) and the typical volume ratio is 5 H₂O:1 H₂O₂:1 NH₄OH. The SC1 hydrogen peroxide solution of high pH is effective at removing organic contaminants by the solvating action of the ammonium hydroxide and the powerful oxidizing action of the peroxide. The ammonium hydroxide also serves to complex some group I and II metals such as Cu, Ag, Ni, Co and Cd. Standard clean 2 (SC2) is effective at desorbing metal contaminants primarily by forming soluble complexes with the resulting ions using a typical solution volume ratio of 6 H₂O:1 H₂O₂:1 HCl. The silicon wafers are immersed in each solution for 10 minutes at solution temperatures of 75-80°C followed by a quench and rinse in running DI water. RCA cleaned wafers are terminated with a thin oxide layer (\approx 1nm thick) which helps prevent against further oxidation or hydrocarbon uptake. Excellent quality of subsequent high temperature silicon oxides and Si/SiO₂ interfaces are obtained using the RCA clean. However, for epitaxial growth to occur on RCA treated wafers, this oxide must be removed. Typically this is done using a dilute HF dip etch or exposure to high temperatures for oxide desorption. In many state-of-the-art devices however, these high temperature processing steps may be undesirable either because of adverse materials interactions or loss of impurity profile due to diffusion.

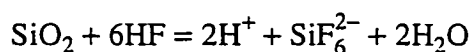
The effectiveness of the RCA cleaning process was first explored by Kern by fabricating metal-oxide-semiconductor (MOS) capacitors on cleaned and deliberately

contaminated silicon wafers and used capacitance voltage (CV) to measure the characteristics of the capacitors. Over the years there have been many published reports detailing the effectiveness of the RCA clean and there have also been many modifications of the RCA process reported (for a review see Kern [69]). Most of the changes to the process have been minor and include: adding a preliminary wafer clean-up treatment with a hot $\text{H}_2\text{SO}_4\text{-H}_2\text{O}_2$ mixture (2:1 volume), using an dilute HF dip etch prior to the SC2 process, and using centrifugal spray cleaning. Surface roughening from both the SC1 and SC2 processes has been found to be minimal, however abundant process repetitions tend to lead to increased surface microroughness. Due to the effectiveness of the RCA cleaning process, it is frequently used to prepare silicon wafers for oxidation and high temperature epitaxial deposition.

3.1.2 Dilute HF Solutions

In recent years, much attention has been given to a method that utilizes a final HF treatment which creates a hydrogen terminated hydrophobic silicon surface. This technique can be used after a cleaning process such as the RCA clean or it may be used on a previously untreated wafer with similar success. No further in situ cleaning of the wafer is required as long as the deposition is started below about 550°C in order to preserve the hydrogen passivation at all times prior to epitaxy [70]. HF etches silicon oxide, removes many metal impurities and completely terminates the silicon surface with hydrogen. Iyer et al. [71] showed that hydrogen terminated silicon surfaces are stable in air for several tens of minutes and in UHV for several hours whereas Mori et al. [72] has reported that the passivated surfaces can remain stable in air for hours. The benefits of this wafer preparation technique are that it is very simple, effective and creates a passive surface.

Removal of the SiO_2 from the silicon surface is accomplished according to the following chemical reaction [73]:



When the oxide has been removed the reaction stops at the silicon surface leaving the surface hydrogen terminated. Surface passivation resulting from HF solutions was first thought to be due to F termination because of the fact that the Si-F bond strength is much greater than the Si-H bond strength (≈ 6.0 versus ≈ 3.5 eV) [74]. However, a wide variety of experimental techniques have recently shown that the chemical stability of the HF treated silicon surfaces is due to surface passivation by hydrogen [9,75,76]. Trucks et al. [74] has studied the mechanism for hydrogen terminated silicon surfaces using dilute HF solutions and has shown that kinetic rather than thermodynamic considerations are responsible for the hydrogen passivation. Upon oxide removal by HF the silicon surface dangling bonds are F-terminated. However, subsequent chemical attack leads to the hydrogen-terminated surface as shown in figure 3.1. The reason for the preferential attack of HF at F-Si-Si sites is due to the polarization of the Si-Si bonds. The F atom weakens the silicon surface back bonds, and H attaches to the underlying silicon leaving behind an H-terminated surface. Since the electronegativity difference is much smaller for Si-H bonds, the hydrogen terminated surface is stable due to the lack of polarization of adjacent Si-Si bonds [74]. However a small amount of fluorine remains on the silicon surface as can be detected by XPS and identified to be Si-F species [66]. Water rinsing produces the loss of fluorine termination and the completion of hydrogen termination [77].

HF treated wafers have been found, using HREELS, to be essentially free of oxide and hydrocarbon contamination [75]. One method used to gauge the effectiveness of oxide removal by dilute HF solutions is to measure the contact angle of water droplets on hydrophobic hydrogen terminated silicon surfaces. The contact angles have been shown to relate directly to the oxygen coverage on the silicon surfaces [70] as shown in figure 3.2. Complete passivation of the silicon surface produces a contact angle of 71° which takes about 30s of immersion in a 0.5% HF solution [70]. During subsequent DI-water rinsing the surface partially re-oxidizes and the contact angle drops by some degrees. Wafer reoxidation in water can be minimized with short rinse times. It has been shown that the

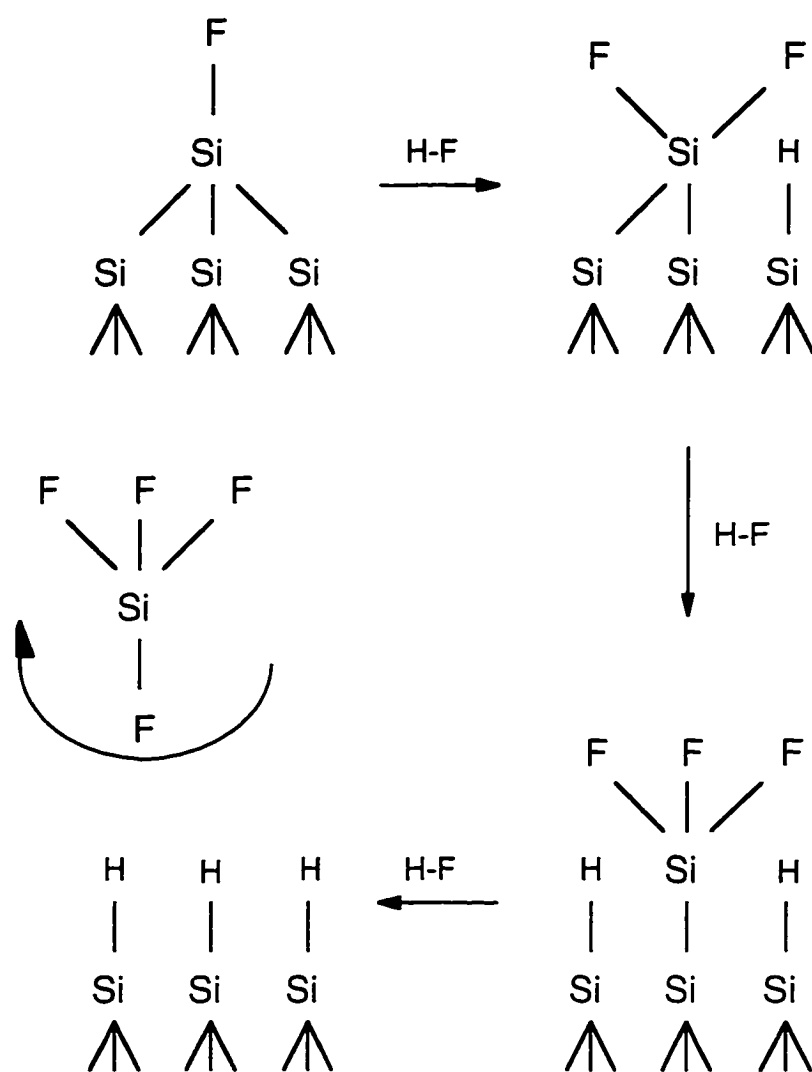


Figure 3.1. Schematic representation of the mechanism of hydrogen passivation proposed by Trucks et al. [74].

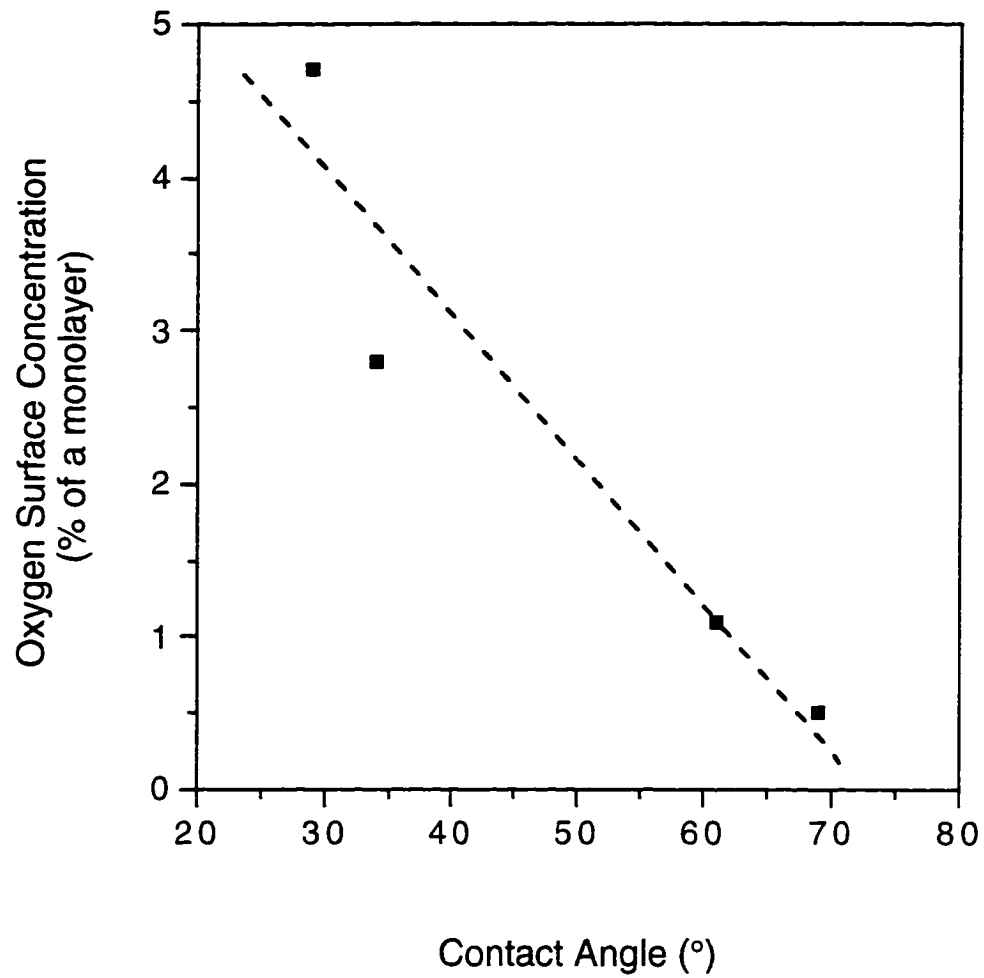
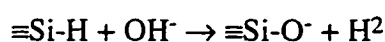


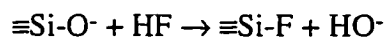
Figure 3.2. Oxygen surface concentration as a function of water droplet contact angle [70].

water rinse removes most of the residual fluorine contamination from 3 to 0.7 atomic percent in as little 3s without adding any measurable amount of oxygen [78]. The contact angle has also been found to gradually decrease as a function of time after HF-dipping.

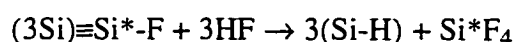
The passivated surfaces can be slowly and selectively etched in dilute or buffered HF solutions, and even in water [79]. Additionally, increasing the pH of the HF solution increases the etch rate of the hydrogen terminated silicon surfaces as evidenced by the increasing formation of small H₂ bubbles. These bubbles are believed to be formed during oxidation of the silicon surface by OH⁻ according to the following reaction [79]:



HF can again attack the silicon surface due to reoxidation. This occurs through HF insertion into the Si-O bond according to the following reaction:



with the subsequent removal of the surface Si atom (labeled Si* to distinguish it from the underlying bulk Si atoms), and passivation of the second layer silicon atoms by hydrogen:



In the proceeding processes, the last two steps are fast compared to the initial oxidation of the hydrogen passivated surface. As a result, the surface is always hydrogen terminated. Oxygen recontamination of the hydrogen terminated silicon surface can occur by a oxidative attack in water or moist air at the Si-F surface sites as well[66]. Reaction with water molecules creates Si-OF surface species, via an insertion reaction. However, the surface is comparatively stable in ambient air against re-oxidation. For low pH solutions

(pH=2) the surface is rough on an atomic scale and for higher pH values (pH \geq 5) there is evidence of (111) microfacet formation on the silicon (001) surface [79]. Rinsing in DI water is important in all stages of the preparation, including after the final etching in the HF solution as it removes species that are weakly bound to the surface (physisorbed or H bonded).

Hydrogen passivation against oxidation can be removed by hydrogen desorption at low temperatures (450-510°C) to create a clean Si surface [80]. Prior to hydrogen desorption, the silicon surface exhibits a (1x1) bulk-like surface structure as determined by RHEED. Upon H-desorption, the surface typically reconstructs to a (2x1) pattern (depending on wafer off-cut and temperature). It was shown by Chiang et al. [31] that for GaAs grown on hydrogen terminated Si substrates, the surface morphology, PL intensity and DCXRD-FWHM improved with increasing pre-growth desorption temperature. These results are consistent with those of Fang et al. [80]. It was also observed by Chiang et al. [31] that excess HF dip during the spin-etch could lead to condensation of moisture and roughening of the Si surface. Thus there appears to be an optimum time period for the HF treatment step. A comparison of the silicon wafer cleans is illustrated in figure 3.3. showing the ideal uses for each clean.

Dilution of HF using ammonium fluoride (NH₄F) is used extensively in the wet chemical processing of devices. The main difference between aqueous HF and buffered HF is the solution pH. The typical volume ratios used in the buffered hydrogen fluoride (BHF) extend from 5:1 to 30:1. Etch rates of the oxide increases with HF concentration but is almost independent of NH₄F concentration. High concentrations of NH₄F are considered to buffer the reaction rate of SiO₂ and to prevent the attack of HF on any photoresist.

Water-insoluble organic compounds tend to make semiconductor surfaces hydrophobic, thus preventing the effective removal of adsorbed impurities. Therefore, surfactants have been introduced to BHF to help in the wafer cleaning by increasing the

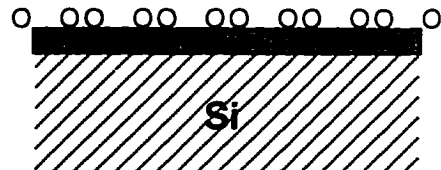
HF Clean

hydrogen passivated

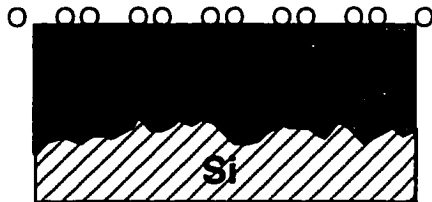


RCA Clean

oxide passivated



Oxidation



Epitaxy

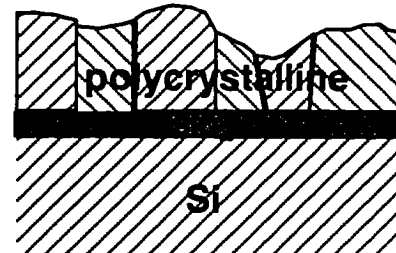


Figure 3.3. Comparison of silicon wafer cleans. An HF clean can be used as a pre-epitaxial clean but leads interfacial microroughness prior to thermal oxidation. The RCA clean is most appropriate prior to a thermal oxidation however during epitaxial growth an RCA cleaned wafer without any additional high-temperature anneal will lead to polycrystalline deposition.

wettability and by reducing surface microroughness. Hydrocarbon surfactants on the order of ≥ 10 ppm are very effective in suppressing the amount of microroughness resulting from BHF solution cleans [81]. Surfactants work by suppressing the reoxidation process of the silicon by the adsorption of the surfactant molecules on the wafer surface which prevents the OH^- from attacking the wafer surface.

A comparison of the effectiveness in cleaning techniques for metallic impurity removal is shown in table 3.1. After an HF clean the metallic contamination on the Si surface is on average lower than after a RCA clean for the typical metals [70].

Table 3.1. Typical metallic contamination on silicon wafers after wet chemical treatment and DI rinsing (units of $10^{10}/\text{cm}^2$).

	K	Ca	Cr	Fe	Ni	Cu	Zn
RCA	0.3	8.6	0.2	5.1	3.3	0.3	0.4
HF	0.1	3.8	0.05	0.3	0.1	0.06	1.2
BHF	0.2	1.4	0.4	2.6	0.3	3.7	0.7

3.1.3 Plasma Cleaning

Ion sputtering and plasma exposure are additional examples of these new low-temperature cleaning techniques. The techniques that employ ions or plasma can be divided into two major process categories: those that use inert gases such as Ar or Ne as the ion/plasma source, and those that use hydrogen.

Plasma processing utilizing discharges has emerged as a promising technique for vacuum chamber cleaning processes owing to the high ion densities at low plasma potential produced by ECR sources for both etching with high etch rates, and thin film deposition

with low surface damage. Argon plasma cleaning is a sputtering process, which has low selectivity and removes oxides and carbon contamination from the silicon surface and has also been used for GaAs surface cleaning [82]. The principal limitation of an argon-based process is the inherent substrate damage from energetic ion bombardment. Previous work has indicated that the optimal argon sputter cleaning process removes the oxide at room temperature, but because of the extensive crystallographic damage after cleaning, a vacuum anneal is required to recrystallize the Si and remove the implanted argon at temperatures of 550-800°C [83]. However Hu et al. [83] cleaned silicon substrates at elevated temperatures to clean and anneal the sample simultaneously. They varied the ion energy as they found these two variables crucial for obtaining the optimal cleaning process. They also found that increasing the ion energy increased the amorphous Si layer thickness due to Ar bombardment but did not seem to increase the surface roughness. In addition, the damage to the Si surface is dominated by ion dose, and is primarily responsible for the roughening of the Si surface.

A study by Yew et al. [84] used argon as well as a mixture of Ar and H₂ to clean silicon substrates. They found that the damaged argon treated surface could repair itself under the appropriate conditions of T and bias, ex. 700°C and -50V. However, if the temperature was decreased or the bias was increased the damaged surface could not self-anneal. The Ar/H₂ plasma cleaning at 0V dc bias was favorable for low temperature treatment. In this case, almost no ion bombardment energy was provided during cleaning so that the damage could be avoided. The Ar/H₂ was also found to remove the UV-ozone-created-oxide better than the argon treatment. This may be attributed to the chemical reaction between the hydrogen plasma and the UV-ozone oxide.

Due to the extreme damage resulting from Ar cleaning and the fact that impurities at the grown-layer/cleaned-Si interface sometimes cannot be entirely eliminated with this technique, it is believed that Ar and Ar/H₂ are not well suited for silicon wafer surface preparation.

The cleaning mechanism for H plasma has been a controversial topic. Some workers have found that the hydrogen ions clean the silicon surface via bombardment [85] while others found that hydrogen radicals rather than ions are the main contributors to surface cleaning [86]. Although the cleaning mechanism is questioned, the fact that a quality impurity free surface can be developed is not. The most convincing work to date that ECR-H plasma cleaning is a viable low-temperature technique is that of Delfino et al. [87,88] They have shown that a silicon surface (001) can be rid of oxides and other contaminants in 3-4 minutes of exposure and result in a passivated monohydride terminated silicon surface. They used in situ XPS and SIMS to eliminate any contaminants from ex situ processing. The ECR module used consisted of a 1.5-kW microwave power supply operating at 2.45 GHz. The operating base pressure was 10^{-8} Torr and no heat was applied to the substrate. It was shown that a peak in the oxygen removal rate corresponded to a maximum in ion density and that the effect of ion energy on the oxide removal was negligible. Thus providing evidence to suggest that the plasma cleaning is activated with hydrogen ions with a removal rate that is proportional to the hydrogen ion density at the substrate. Physical sputtering is considered a less likely mechanism in view of both the light mass of hydrogen and the observed invariance of the oxygen removal rate to ion energy.

3.2 Epitaxial Silicon Surfaces (ESS)

Recently, single-domain GaAs on epitaxial Si surface (ESS) substrates has been reported [72]. The ESS substrates, with a 0.5° off-cut and $5\mu\text{m}$ layer of epi-Si, were found to have a single domain structure without high-temperature treatment. Typically, an anneal of the substrate prior to growth is required in order to form a single domain double-step surface. AFM was used to examine the ESS substrates (as-received) which revealed a single domain double step surface. The wafers were obtained commercially and were first chemically oxidized in $\text{H}_2\text{SO}_4+\text{H}_2\text{O}_2+\text{H}_2\text{O}$, rinsed in DI and then etched in a 7% aqueous

HF solution for about 30s to passivate them by hydrogen termination. The wafers were then loaded into a loadlock chamber and filled with H₂ at atmospheric pressure. The HF-treated ESS were very stable in air (8hr air exposure).

Mori [72] compared the growth of GaAs on ESS to that on traditional polished wafers and found that the GaAs layer grown on the ESS substrate had a flat and mirror surface, but the one grown on the polished substrate was rough. These differences may result from the flatness of ESS. A rough surface is more easily oxidized than a flat one and may contain impurities and a double domain (2x2). Grunthaner et al. [89] reported that oxide desorption at high temperatures leads to an increase in Si surface roughness, and that Si surfaces with large undulations can be smoothed by the growth of Si. ESS flatness was confirmed by Mori [90] using AFM with a double step height of 0.22nm, and an average terrace width of 25.6nm of the 0.5° off-cut wafers. In addition, Si diffusion into GaAs could not be found in the GaAs/ESS, but found to be remarkable in the GaAs on the high temperature treated Si (820°C) as found by SIMS.

The AFM is an ideal instrument for measuring the surface roughness resulting from wet chemical etching used to prepare silicon substrates for epilayer growth. Polished (001) silicon surfaces as-received from the wafer manufacturer have maximum peak to valley distances of 8.6Å and RMS roughnesses of 1Å [91]. Epi-silicon wafers with >1µm of deposited silicon have RMS roughnesses of ≤0.9Å. After a surface has been exposed to a wet chemical cleaning solution, the roughness of the surface typically changes. Variations in chemical ratios (pH) in cleaning solutions result in different roughness changes. For example, a change in NH₄OH:H₂O₂:H₂O ratio from 2:11:27 to 11:20:4 results in a change in RMS roughness from 1.5 to 1.2Å. Although the difference seems small, it has been shown that even small scale increases in surface roughness can lead to reduced reliability of gate dielectrics.

3.3 Silicon Substrate Preparation for MOMBE Growth

Proper preparation of silicon substrates before deposition is a necessary step for the growth of high quality epitaxial films. Native oxides, surface impurities and surface defects can influence the nucleation behavior of epilayers and are often found to be sources for epitaxial film defects. Traditional methods for removing the surface impurities utilize repetitive oxidation/etch steps which are effective in minimizing residual surface impurities [68]. As previously mentioned, a commonly used approach in the last step of substrate preparation involves the use of a HF dip-etch [80,92,93]. This step removes the oxide and leaves the silicon surface passivated with virtually no surface dangling bonds and a very low surface-recombination velocity [94]. Chemical analysis of HF treated Si surfaces reveals almost complete hydride coverage with a predominately occurring dihydride termination for smooth surfaces and monohydride and trihydride coverages for increasingly rough surfaces [95,96]. Wet chemical treatments, however, can also influence the surface morphology [97]. The coexistence of oxidation/etch steps has a roughening effect on the resulting Si surface [96]. Many variations of HF dip-etch conditions exist including variations of etch time, etchant concentration and etch temperature. In the following experiments the effect of different HF:DI concentrations and dip-etch times on the surface roughness of etched Si substrates, GaP/Si interfacial oxygen concentration, and epilayer microstructure was studied.

3.3.1 Experimental Techniques

Experiments were performed on epitaxial silicon substrates (ESS) with 1 μ m of deposited silicon obtained commercially from Silicon Quest International. The p-type wafers were 2" in diameter with (001) on-axis orientation and a resistivity of 1-10 Ω cm. p-type wafers were used because they have been shown to be more resistant to surface microroughness as a result of exposure to HF solutions [81]. Prior to deposition of the GaP, the ESS wafers were dip-etched using HF:DI processes listed in Table 3.2.

Variations in etch solution concentrations and etch times were studied as they had not been previously researched for ESS wafers.

Table 3.2. HF:DI dip-etch conditions for the preparation of ES substrates prior to growth.

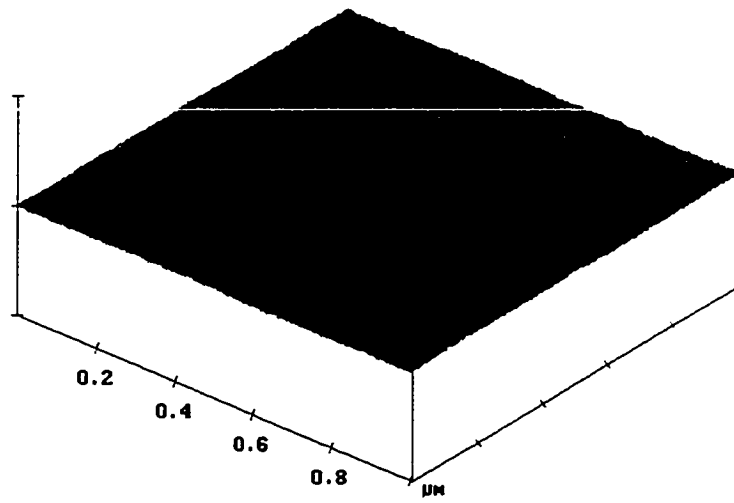
<u>Process #</u>	<u>HF:DI Volume Ratio</u>	<u>Dip-etch Time</u>	<u>Rinse Time</u>	<u>Conc. Ratio x Time</u>
1	1:50	15s	15s	0.3
2	1:50	30s	15s	0.6
3	1:10	15s	15s	1.5
4	1:10	30s	15s	3.0

The effect of time and etch concentration on the surface roughness of the ESS wafers was examined by etching four wafers using each one of the etch processes. In addition, the effectiveness of buffered HF solutions both with and without surfactant were studied (10 NH_4F : 1 HF). The wafers were dipped in each BHF solution for 15s. A Nanoscope III (Digital) atomic force microscope (AFM) was used for imaging and to obtain root-mean-square (RMS) values for surface roughness as calculated by accompanying computer analysis software. A Varian Gen II metal-organic molecular beam epitaxy (MOMBE) system was used to grow $0.3\mu\text{m}$ thick GaP epilayers on etched ESS wafers at a growth temperature of 450°C . Flow rates for the precursors triethylgallium (TEG) and phosphine (PH_3) were 0.94sccm and 2sccm respectively and the chamber pressure during growth was $\approx 8.7 \times 10^{-6}$ Torr. The etched ESS wafers were exposed to ordinary laboratory air for ≤ 15 minutes before entry into the MOMBE loadlock chamber. HRTEM was used to examine the microstructure and heterointerfaces of the GaP epilayers and SIMS was used to determine the impurity concentrations at the GaP/Si interface.

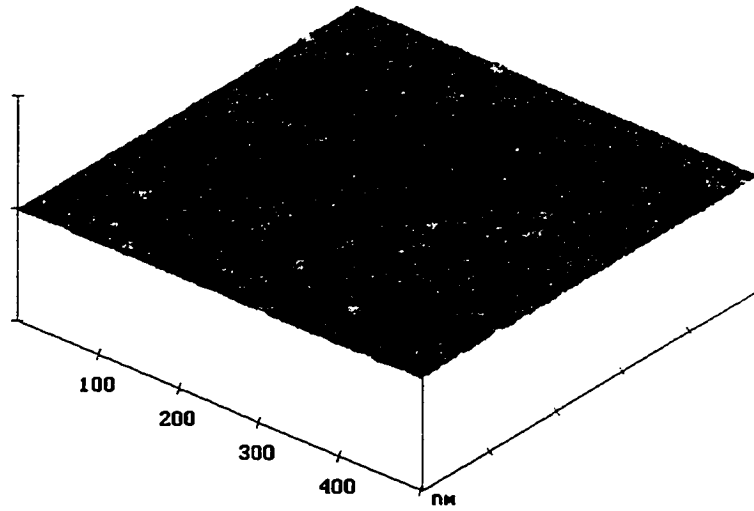
3.3.2 Results and Discussion

The smoothness of as-received bulk grown silicon wafers is generally defined by polishing. Epitaxial silicon wafers were used in these experiments because they were shown to provide a smoother starting surface both before and after wet chemical etching due to surface planarization during CVD growth [72,90]. AFM measurements of the as-received ESS wafers found the RMS to be $\approx 0.9\text{\AA}$ and practically featureless as shown in figure 3.4a. Upon exposure to HF:DI solutions and removal of the native oxide, the surfaces became hydrophobic and the surface roughness increased as shown in figure 3.4b.. To compare the surface roughening effect for each etch concentration and time, RMS values were measured for each process and plotted in figure 3.5. The horizontal axis is defined as the etch time multiplied by the HF:DI ratio and the error bars represent the standard deviation in the roughness data. Surface roughness of the ESS wafers was found to increase with both increases in etch time and HF etch concentrations. Surface roughening has been shown to be a side effect of diluted HF treatments and a function of etchant pH and exposure time.

SIMS analysis of the oxygen concentration at the GaP/Si heterointerface showed a similar trend in the data as compared to the ESS wafer surface roughness as seen in figure 3.5. The SIMS data is presented in area under the oxygen curve at the heterointerface as calculated by SIMS analysis software. Each of the SIMS data points is reported in units of counts/second. The correlation in the SIMS and AFM data can be explained by increases in incorporation sites due to the increase in surface area associated with surface roughness. Additionally, it has been reported that increased HF concentrations lead to slight increase in oxygen contamination on the Si surface [98]. Takahagi et al.. investigated this by using XPS to observe the fluorine content on HF treated silicon surfaces and found that fluorine contamination increased with HF concentration. Upon rinsing the HF treated wafer in DI water the Si-F bonds were mostly replaced by hydroxyls (Si-OH) through hydrolysis, thus increasing the oxygen on the surface. In Takahagi's studies, however, it was found that



a)



b)

Figure 3.4. AFM $5\mu\text{m}^2$ scans of a) as-received ESS wafer and b) etched ESS wafer using process #2 (1:50 for 30s). Z scale = 20nm/div .

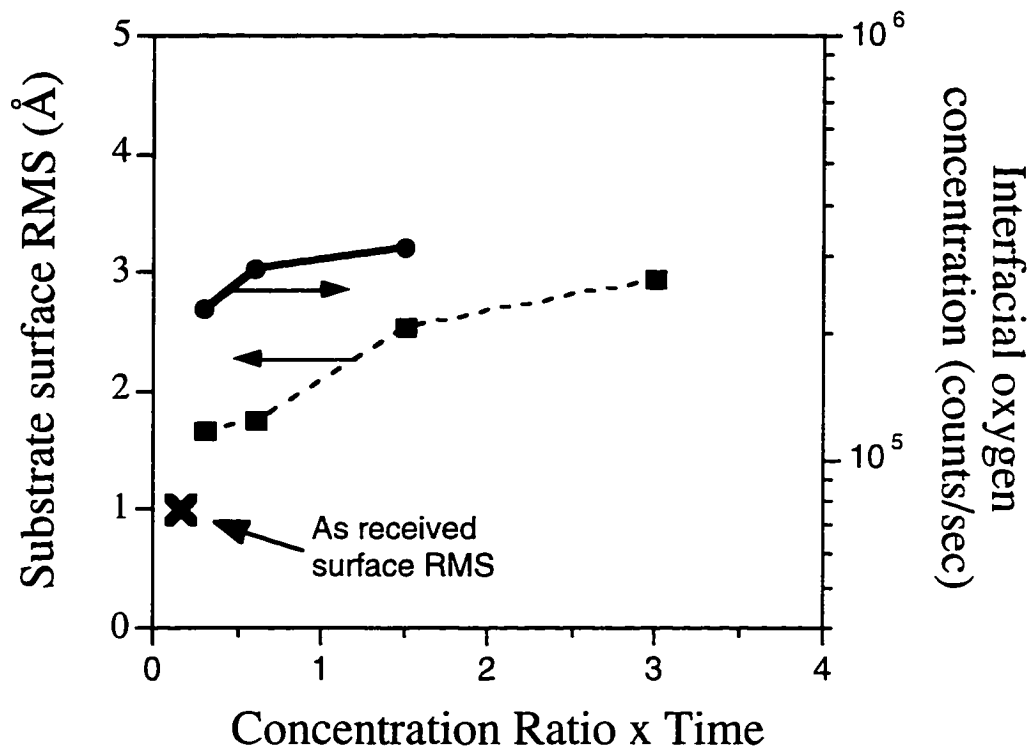


Figure 3.5. Comparison of AFM RMS data from etched ES wafers (left side) and SIMS interfacial oxygen concentration data (right side). Graph shows a trend in the data corresponding to increases in oxygen contamination as substrate surface roughness increases.

the oxygen concentration of the silicon wafer remained the same with varying etchant immersion time in contrast to our results.

Additional SIMS analysis was conducted on one sample by Charles Evans & Associates using standards to quantify the oxygen at the interface. The sample grown on a Si wafer cleaned with process #1 (1:50 for 15s) was found to have a peak oxygen concentration of $\approx 5.5 \times 10^{19}$ atoms/cm³ at the interface and an areal density of $\approx 1.2 \times 10^{14}$ oxygen atoms/cm² ($\approx 17\%$ of a monolayer). Further, SIMS analysis of oxygen, fluorine and carbon in the GaP epilayer showed background concentrations of 3×10^{17} atoms/cm³, $< 1 \times 10^{16}$ atoms/cm³ (below delectability) and 9.8×10^{19} atoms/cm³ respectively. The high carbon background can be attributed to the low growth temperature, and a nonoptimized V/III ratio.

AFM analysis of the BHF treated wafers revealed that the roughening effect for both solutions with and without surfactant was comparable to HF:DI treatment #1(1:10) as shown in figure 3.6. Surfactant additions did not appear to significantly suppress the roughening of the silicon surface as expected when compared to the surface roughness of the wafer subjected to the BHF without surfactant solution. This is due in part to the short etch time of 15s as longer etch times should show a more dramatic effect. However the effectiveness of substrate reoxidation suppression is apparent as the oxygen concentration at the heterointerface is lower than the HF:DI etched wafer. The decrease in oxygen concentration at the interface for the BHF solutions can possibly be explained by a difference in the concentration of fluorine termination on the silicon surfaces after the BHF dip etches.

Each GaP epilayer grown was single crystal, however, high densities of stacking faults and microtwins were found in the epilayers as shown in figure 3.7. These planar defects are believed to arise from the use of on-axis wafers, residual surface impurities, stacking errors, and the roughness of the ESS wafers. Stacking fault formation has been shown to not be a strong function of lattice mismatch [99]. Residues from improper

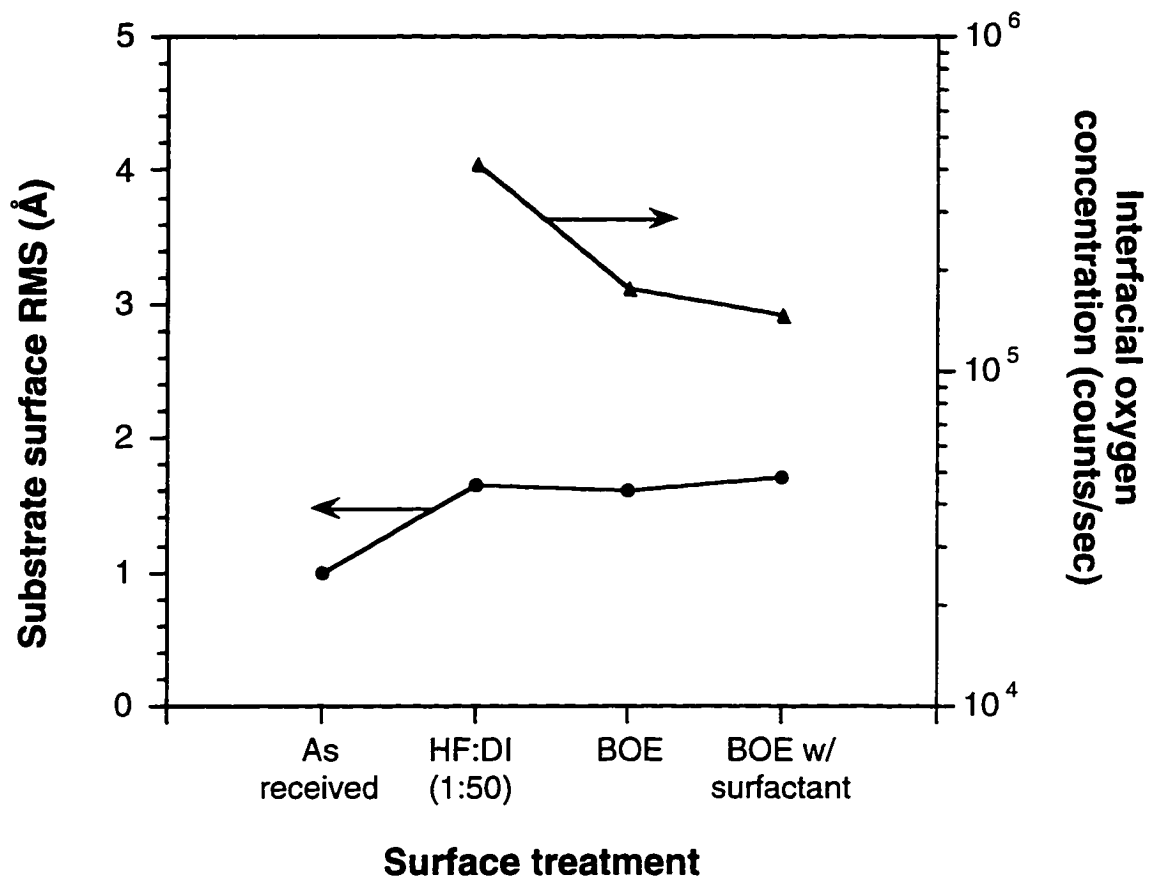


Figure 3.6. Surface roughness and interfacial oxygen concentration comparisons for selected silicon wafer wet etch treatments.

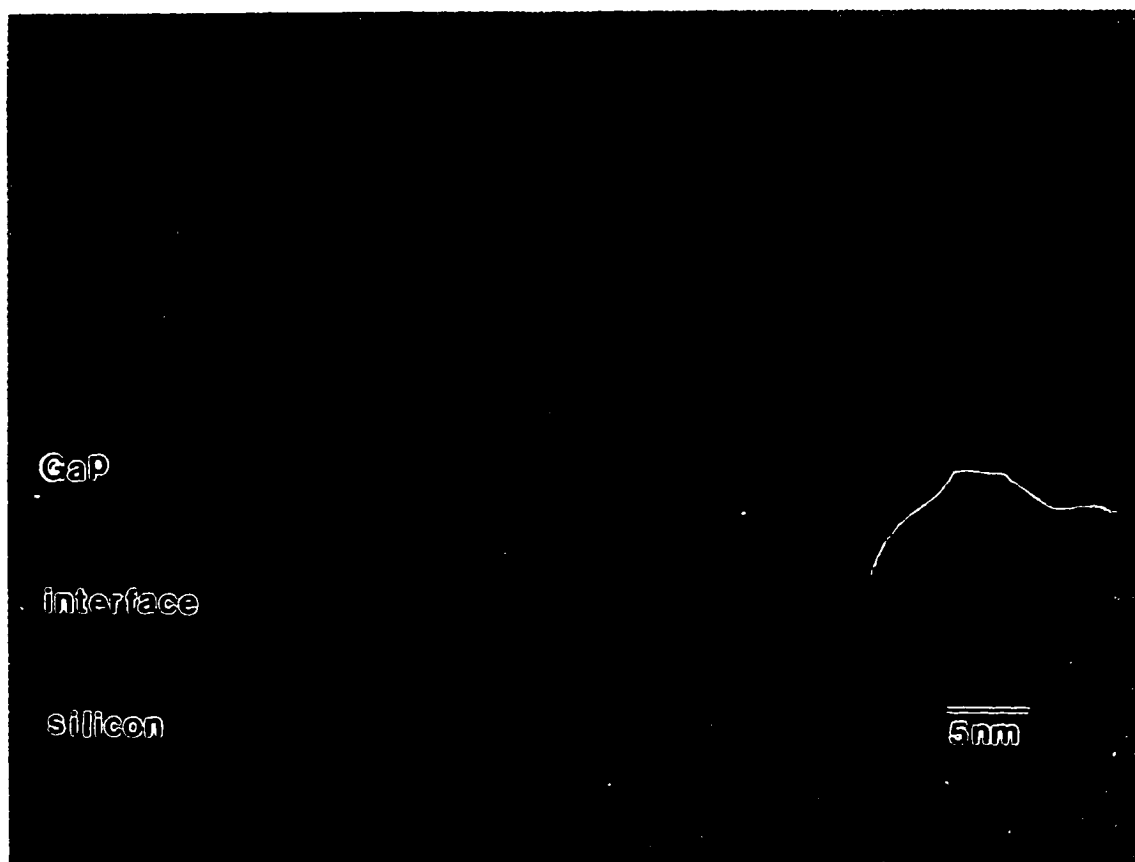


Figure 3.7. HRTEM cross-sectional image of GaP/Si (2.2MX) after surface preparation process #2 (1:50 for 30s). Planar defects are abundant and areas of disorder can be found at the heterointerface.

cleaning are reported to give rise to twinning, dislocations, stacking faults and other crystal defects [68]. The planar defect densities of the epilayers were calculated from plan-view TEM and were on the order of $>5 \times 10^8/\text{cm}^2$. A trend in planar defect density with the etchant process parameters could not be found. This could be due to the difficulty in the quantification of the density data. Many of the stacking faults were annihilated very near the interface and did not extend to the surface of the epilayer making them difficult to count. Only the stacking faults extending through the epilayer were counted leading to errors in the density data. There was excellent registry across the interface which led to the single crystal nature of the GaP epilayers. Some areas of disorder were found at the interface and are a result of either residual oxides [100] or carbon impurities [34], or strain in the lattice from interfacial defects. HRTEM revealed no evidence of variations in microstructure or interfacial quality as a function of etch processes.

3.4 Summary

In conclusion, it has been shown that HF:DI and BHF solutions have a slight surface roughening effect on the ESS substrates. The trend in surface roughness data for the different etch processes was mirrored in the SIMS data for the oxygen concentration at the GaP/Si heterointerface. However, the microstructures of the single crystal GaP epilayers were indistinguishable and did not appear to be affected by changes in the substrate cleaning processes. The epilayers contained many stacking faults and microtwins especially near the interface. Formation of these planar defects are believed to be assisted by the use of on-axis wafers, surface roughening, nucleation mode, and the incomplete removal of surface impurities such as oxygen or carbon.

CHAPTER 4

NUCLEATION OF AlGaP ON SILICON

4.1 Introduction

As discussed in the literature review section, experimental studies conducted on the $\text{Al}_x\text{Ga}_{1-x}\text{P}/\text{Si}$ system grown by MOCVD have shown that increasing the aluminum concentration in the ternary has contributed to a surface smoothening effect of the $\text{Al}_x\text{Ga}_{1-x}\text{P}$ layer. This is beneficial for the growth of III-Vs on silicon as smooth buffer layers have been shown to improve the surface and film quality of subsequently grown III-V layers [39]. However, reasons for the improvement in planarity of $\text{Al}_x\text{Ga}_{1-x}\text{P}$ epilayers is not fully understood and studies of the early stages of growth of $\text{Al}_x\text{Ga}_{1-x}\text{P}$ on silicon have not been conducted. In this chapter, the results of an extensive nucleation study are detailed and are found to contrast with the results of MOCVD grown materials. In addition, a model is presented to explain island evolution in the $\text{Al}_x\text{Ga}_{1-x}\text{P}/\text{Si}$ heteroepitaxial system in MOMBE.

A set of $\text{Al}_x\text{Ga}_{1-x}\text{P}/\text{Si}$ samples was grown by MOMBE with AlP mole fractions of $x=0, 0.15, 0.3$, and 0.45 . Approximately 50\AA of $\text{Al}_x\text{Ga}_{1-x}\text{P}$ was deposited on the silicon substrates to examine the early stages of growth. Cross-sectional transmission electron microscopy and atomic force microscopy analysis were performed on the $\text{Al}_x\text{Ga}_{1-x}\text{P}/\text{Si}$ samples in order to observe the growth mode, feature densities and geometries, and defects, as a function of several growth parameters including composition and growth temperature.

The following chapter is divided into two sections. In the first section (4.2), the experimental results concerning the growth mode and deposition characteristics of $\text{Al}_x\text{Ga}_{1-x}\text{P}$.

x P are presented, and in the second section (4.3) a discussion of the results is given which contains the proposed nucleation model based on MOMBE precursor deposition mechanisms and surface kinetics used to explain island evolution in the $\text{Al}_x\text{Ga}_{1-x}\text{P}/\text{Si}$ system.

4.2 AFM and TEM Analysis of AlGaP/Si Early Stages of Growth

Examination of the $\text{Al}_x\text{Ga}_{1-x}\text{P}$ deposits by AFM and TEM revealed that the growth mode for the ternaries was island (3D) type for every growth condition studied. Quantitative analysis of the islands was therefore necessary in order to examine the effects of composition and growth temperature for the establishment of suitable nucleation conditions for buffer layer growth. Island densities could not be obtained accurately from XTEM micrographs due to both island overlap and unknown specimen thickness. PTEM also posed a challenge as the smaller island heights were in the range of several tens of angstroms making them difficult to resolve. Therefore, island distribution data was collected by AFM imaging. Distribution data was obtained by defining height thresholds for planes that sectioned the three-dimensional data from the AFM scans at defined heights above the substrate surface resulting in planes of sectioned features (islands). The number of the sectioned islands within the planes was calculated by the accompanying computer and software for each height threshold.

As discussed in Chapter 3, each of the silicon wafers was exposed to a diluted HF solution to remove the native oxide prior to growth which caused a finite amount of surface roughening. AFM scans of etched wafers revealed many surface features that may interfere with data taken from scans of 50Å $\text{Al}_x\text{Ga}_{1-x}\text{P}$ deposits. Figure 4.1 shows a feature height histogram of an etched silicon wafer which was used to establish a surface roughness background for all of the subsequent deposits. As can be seen from the figure, the majority of the features on the surface of the etched wafer were less than 10Å in height. Therefore, to minimize error in the $\text{Al}_x\text{Ga}_{1-x}\text{P}$ island histograms, data below 10Å was discarded.

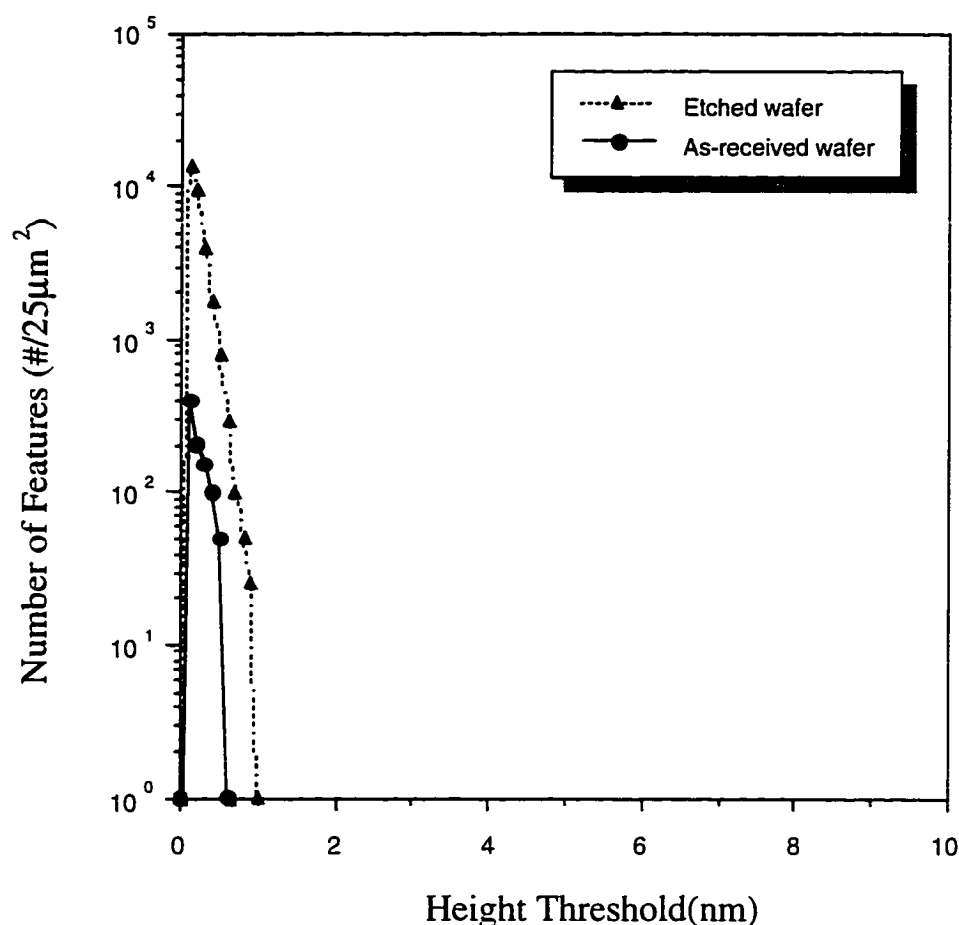


Figure 4.1 AFM feature height histogram of as-received and etched wafer.

In figure 4.2, normal incidence AFM images of the main set of $\text{Al}_x\text{Ga}_{1-x}\text{P}$ specimens are shown for $x=0$ to 0.45 and growth temperatures of 450°, 500° and 550°C. These AFM images were used in collaboration with the HRTEM to better understand and view the nucleation processes. As can be seen from figure 4.2, changes in composition and growth temperature alter the island geometries and density. GaP deposited on silicon led to island growth that had a fairly narrow distribution of island heights at low temperatures and an expanded distribution for higher growth temperatures (T_G) as shown in the AFM distribution plots in figure 4.3. As the growth temperature was increased, the

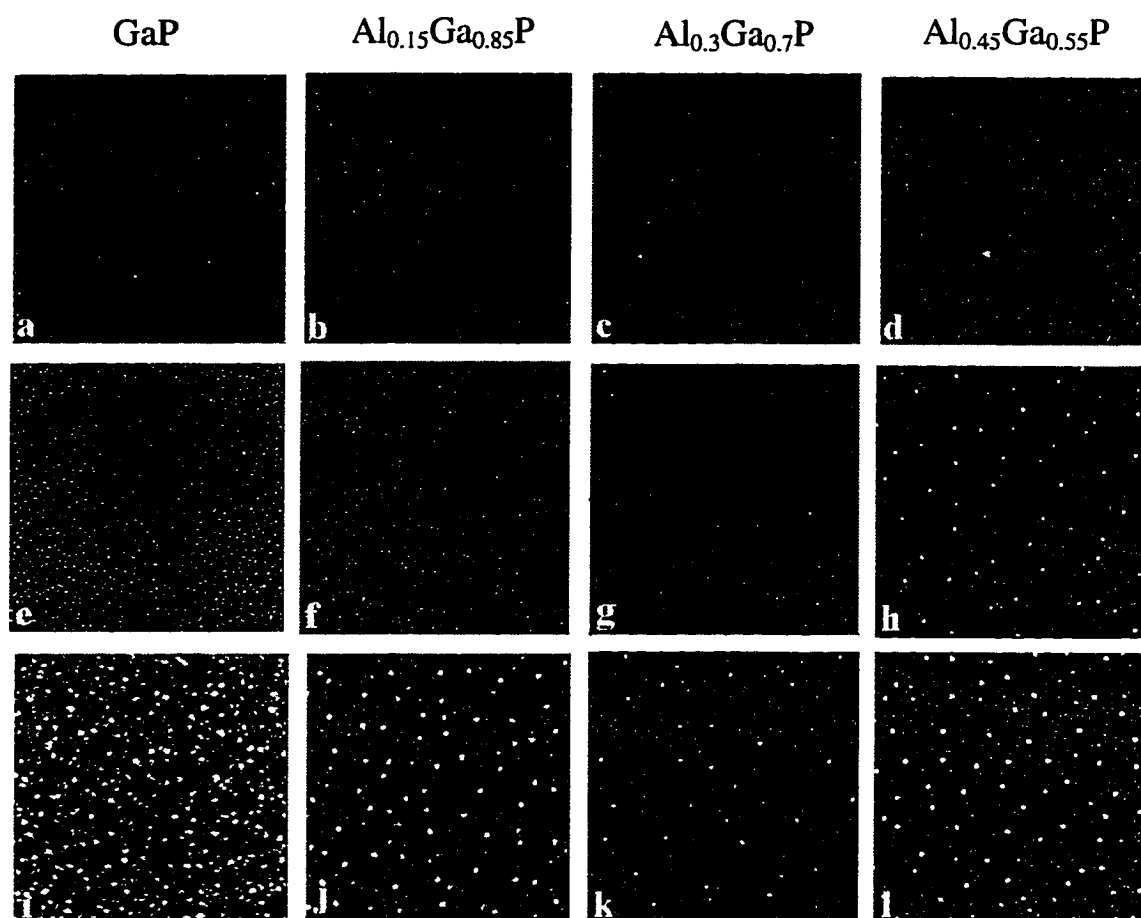


Figure 4.2 AFM top-view images of $\text{Al}_x\text{Ga}_{1-x}\text{P}$ sample matrix for growth temperatures of 450°(a-d), 500°(e-h), and 550°C(i-l).

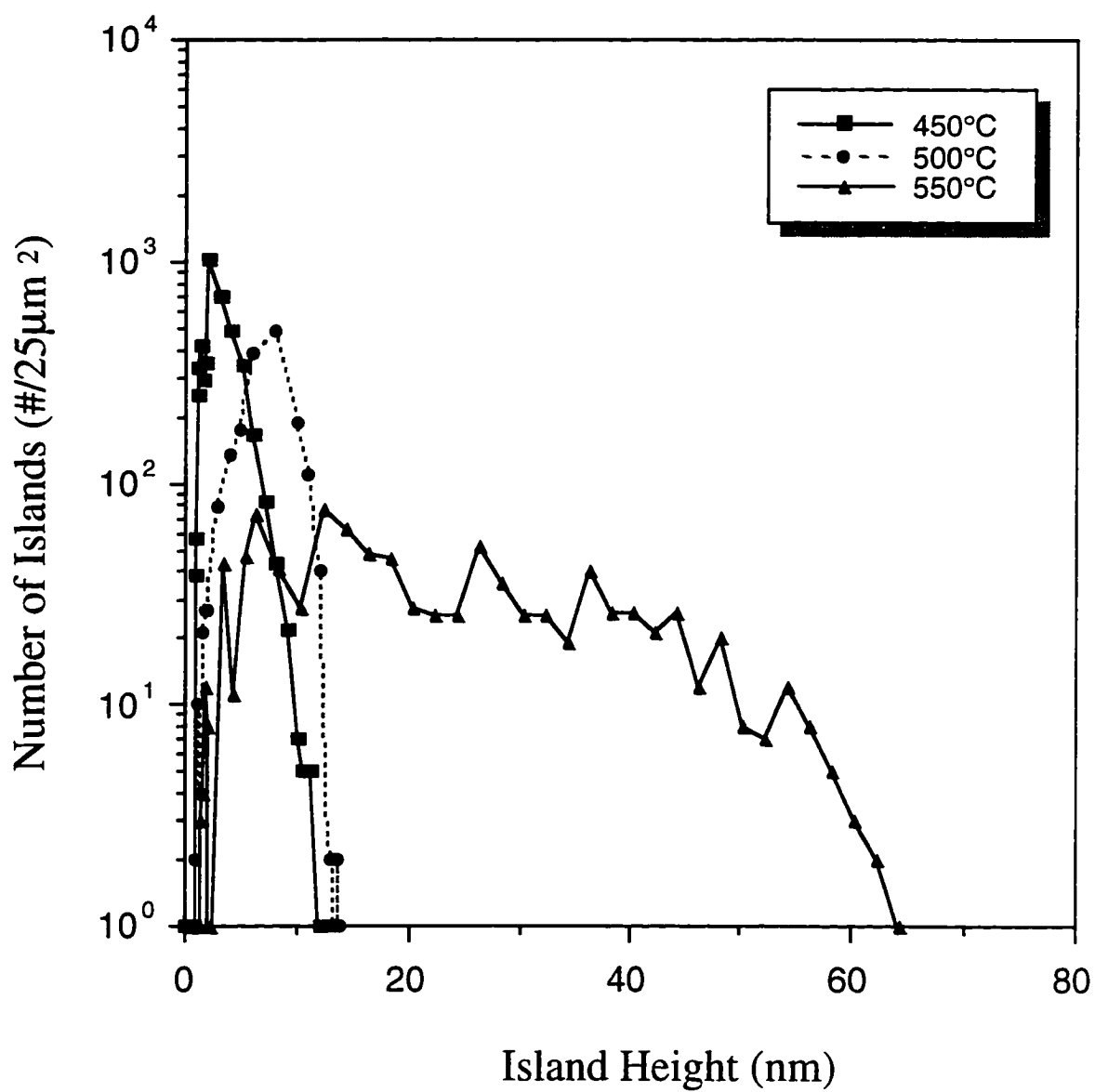


Figure 4.3 Island height histograms for GaP/Si islands deposited at 450°, 500° and 550°C.

GaP islands were found to increase in both size and distribution. {111} faceting of the GaP islands occurred at each growth temperature and was especially pronounced at $T_G=550^\circ\text{C}$ as shown in figure 4.4b. Defects existed in the islands even at these early stages of growth and were identified to be stacking faults and microtwins.

Addition of aluminum to the GaP at $T_G=450^\circ\text{C}$ was found to cause the island height distribution to narrow as shown in figure 4.5 for 15% aluminum. The island height distribution for the ternary composition of 30% aluminum at $T_G=450^\circ\text{C}$ showed a slight broadening as well as a slight peak splitting as seen in figure 4.6a. With a further increase in aluminum concentration, a more visible change in height distribution was marked by the onset of two distinct peaks in the distribution data. The coexistence of two distributions of island sizes is referred to as a bimodal distribution throughout the remainder of this dissertation. An additional growth run was conducted at $T_G=450^\circ\text{C}$ with $x=0.7$ to determine if the bimodal distribution persisted with increasing concentrations of aluminum. The island height distribution for the 70% aluminum sample is shown in figure 4.7 and was found to be bimodal.

Nucleation of $\text{Al}_x\text{Ga}_{1-x}\text{P}$ at $T_G=500^\circ\text{C}$ also showed a transition from a single distribution of island heights to a bimodal one with increases in aluminum composition. The onset of the bimodal distribution however occurred at $x=0.3$ (see figure 4.8) instead of $x=0.45$ as was found at $T_G=450^\circ\text{C}$. The bimodal distribution was clearly evident for $x=0.45$ as a large population of short islands coexisted with a smaller population of taller islands (figure 4.9). XTEM of the two distinct island heights found in the bimodal distributions is shown in figure 4.10. Imaging of the larger islands in HRTEM was difficult because of their scarcity. AFM data revealed that the large island population was approximately an order of magnitude less than that of the smaller islands. In thicker areas of the XTEM specimens, the deposits resembled continuous $\text{Al}_x\text{Ga}_{1-x}\text{P}$ films with a few scattered large islands. Individual small islands were not discernible in the thicker regions of the XTEM samples due to island overlap. The large islands were also found to be



Figure 4.4 HRTEM images of GaP islands on Si at $T_G=450^\circ$ and 550°C .

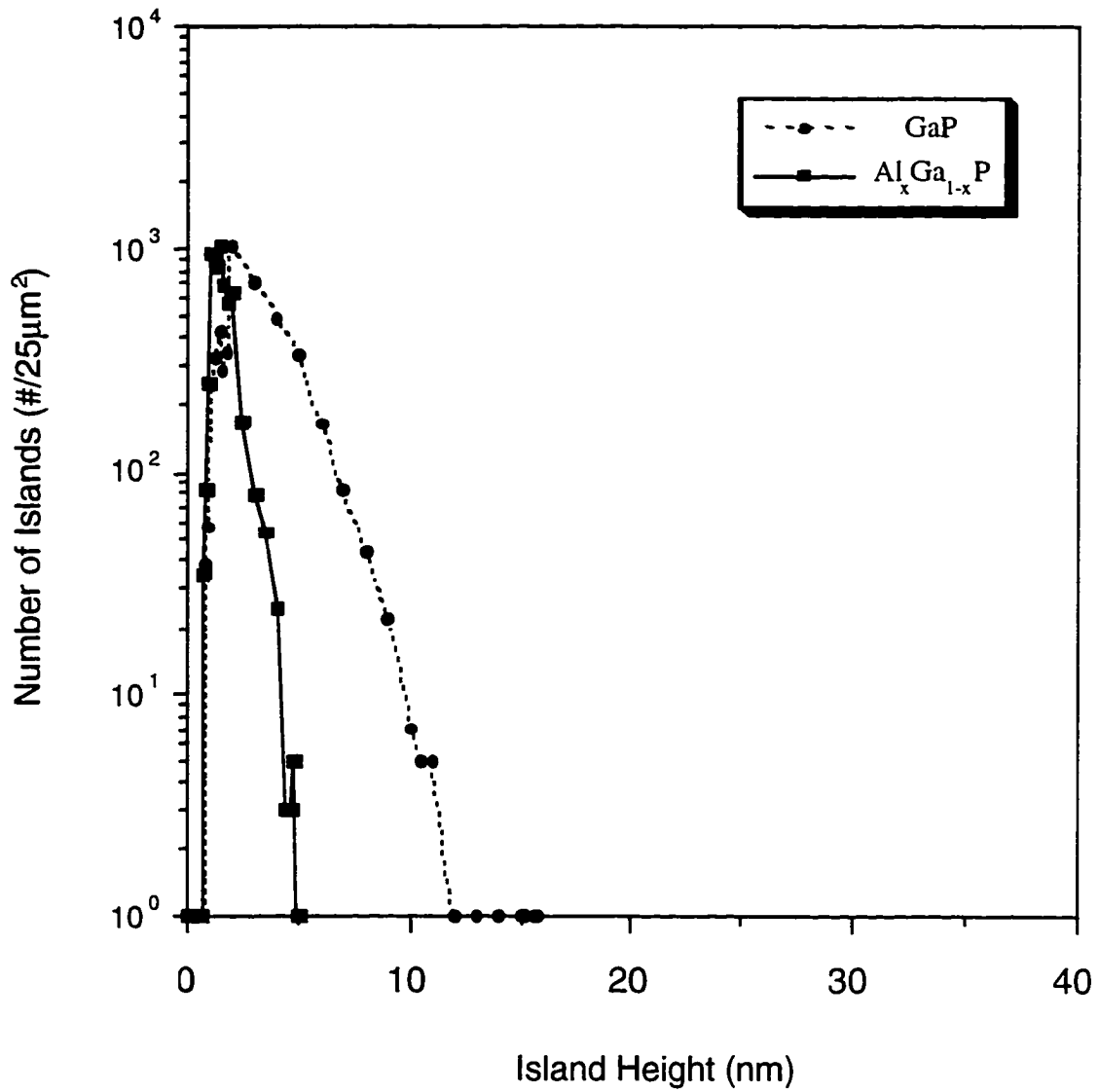
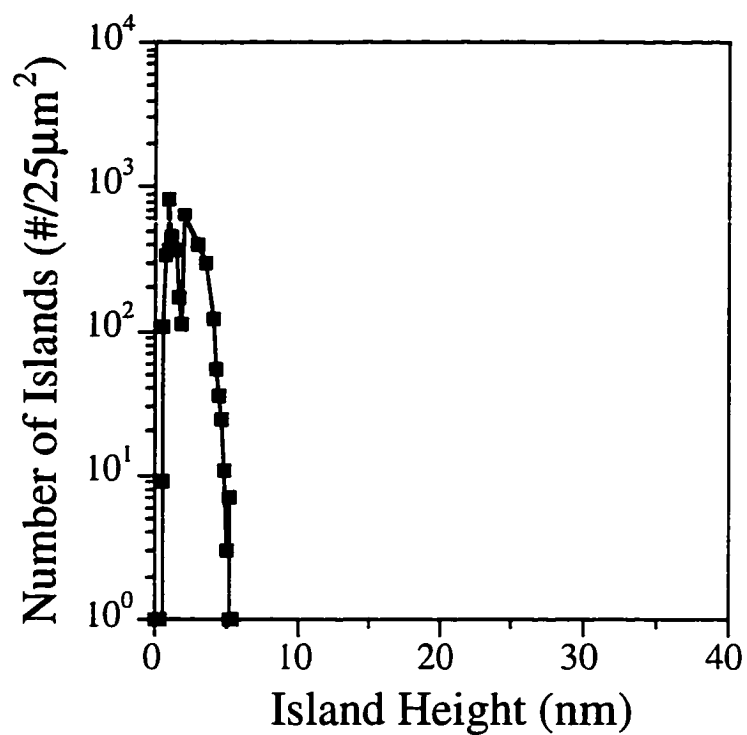
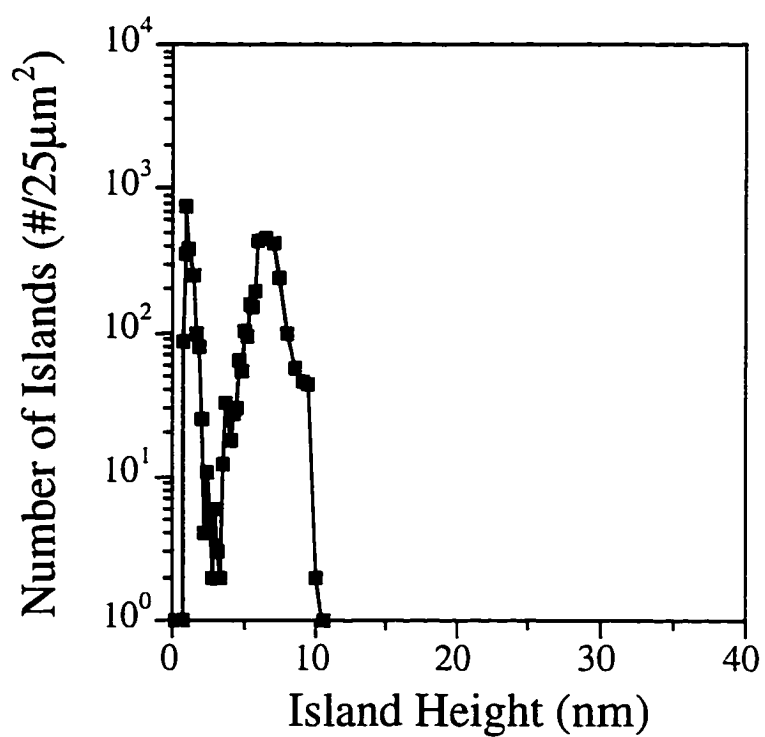


Figure 4.5 Island height distribution for $\text{Al}_x\text{Ga}_{1-x}\text{P}$ with $x=0.15$ and $T_G=450^\circ\text{C}$.



a)



b)

Figure 4.6 Island height distribution for $\text{Al}_x\text{Ga}_{1-x}\text{P}$ at $T_G=450^\circ\text{C}$ a) $x=0.3$ and b) $x=0.45$.

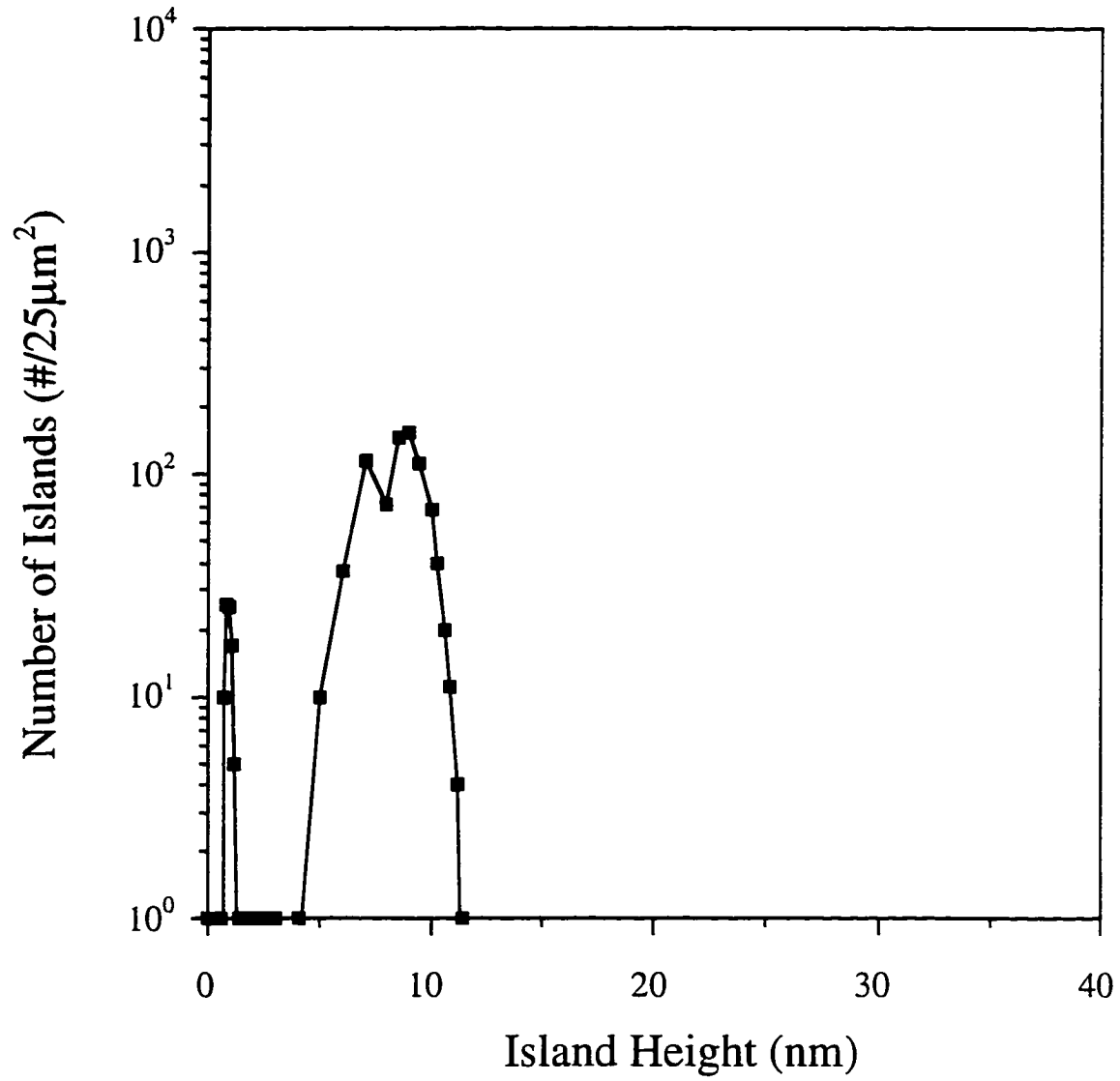
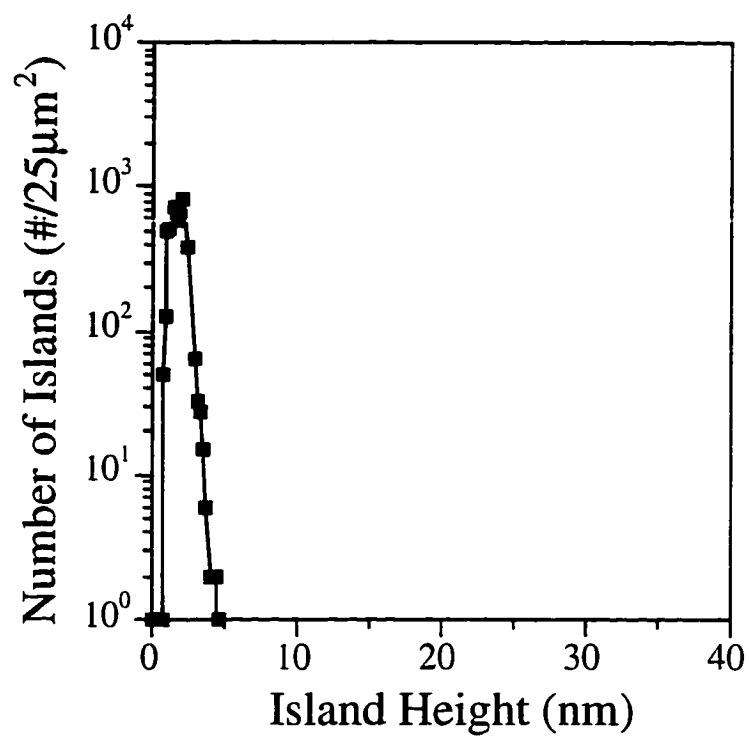
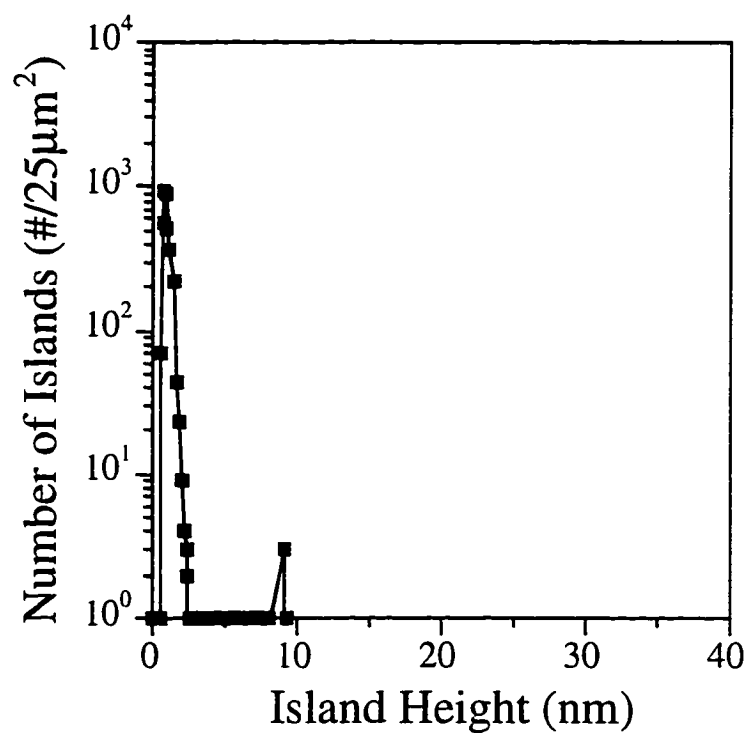


Figure 4.7 Island height distribution for $\text{Al}_x\text{Ga}_{1-x}\text{P}$ with $x=0.7$ and $T_G=450^\circ\text{C}$.



a)



b)

Figure 4.8 Island height distribution for $\text{Al}_x\text{Ga}_{1-x}\text{P}$ for $T_G=500^\circ\text{C}$ and a) $x=0.15$ and b) $x=0.3$

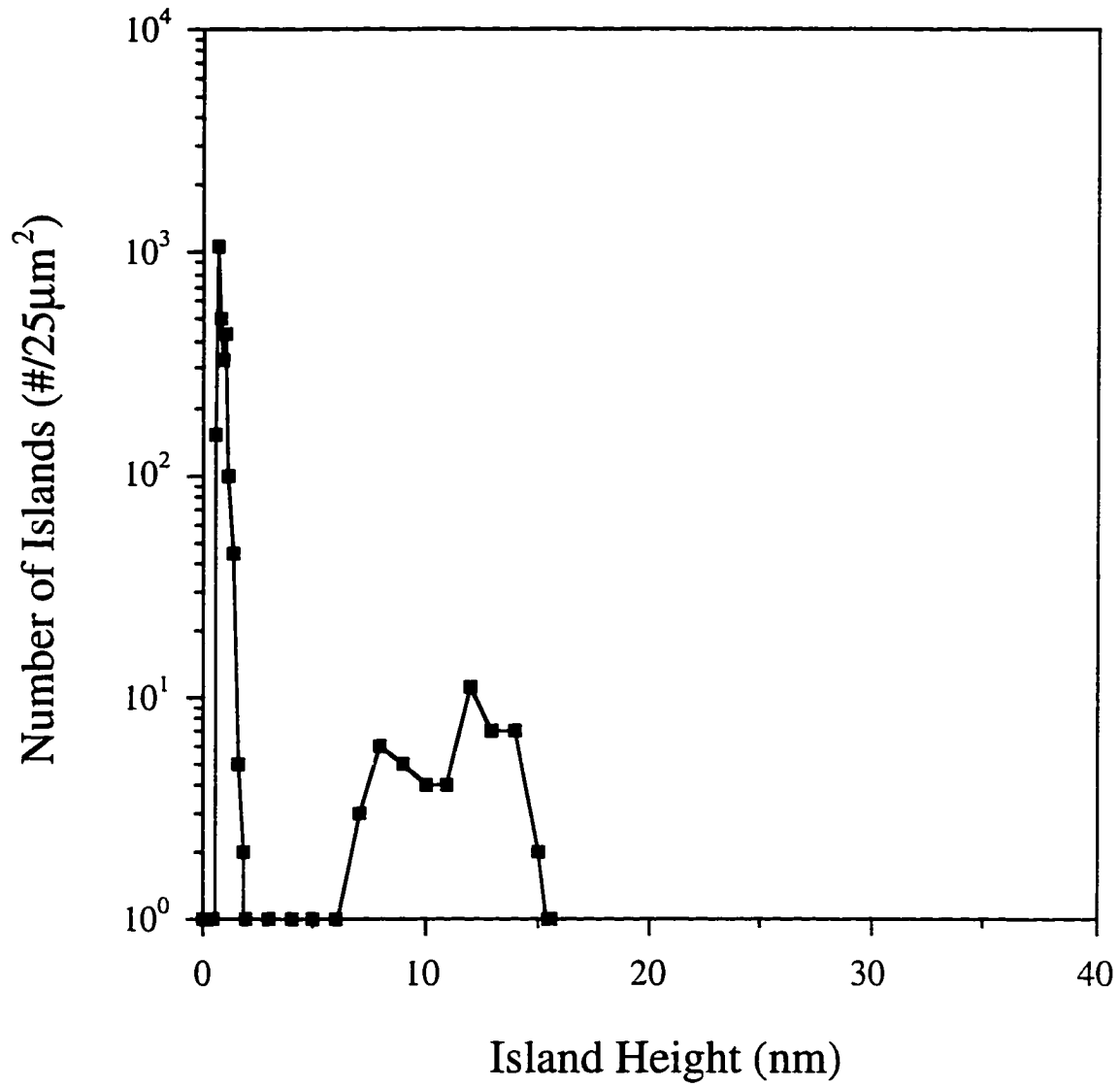


Figure 4.9 Island height distribution for $\text{Al}_x\text{Ga}_{1-x}\text{P}$ with $x=0.45$ and $T_G=500^\circ\text{C}$.

separated from the smaller islands by areas of apparent bare silicon substrate as seen in the XTEM micrograph of figure 4.10 and in a top-view AFM image in figure 4.11.

At $T_G=550^\circ\text{C}$, there was no transition from a single distribution to a bimodal one as the bimodal island height distribution was found for each composition as shown in figure 4.12. The distribution of island heights did not appear to be influenced by changes in composition at 550°C as found for both 450° and 500°C . Therefore, the bimodal growth mode appears to be a function of both composition and growth temperature.

Separation distances between large islands and large-island densities were calculated by visual examination of AFM top view images. The large-island density was obtained by counting the number of islands per $25\mu\text{m}^2$ scan, and the island separation distances were measured by taking into account the distance to the first three nearest island neighbors. The values for the counts are shown in table 4.1. The island separation distance was found to depend on the island density N which followed a simple geometric law of $1/\sqrt{N}$, as expected for a random distribution [101]. Therefore, the large islands are randomly distributed on the surface with no indication of preferential nucleation.

Table 4.1 Calculated large-island density and island separation values from AFM images.

Growth Conditions	Measured Island Density ($\#/\mu\text{m}^2$)	Measured Island Separation Distance (μm)	Calculated $1/\sqrt{N}$ (μm)
450°C , 45% Al	116	0.10	0.09
500°C , 30% Al	0.12	3.1	2.89
500°C , 45% Al	2.16	0.72	0.68
550°C , 15% Al	3.48	0.56	0.54
550°C , 30% Al	1.24	1.0	0.90
550°C , 45% Al	3.12	0.60	0.57

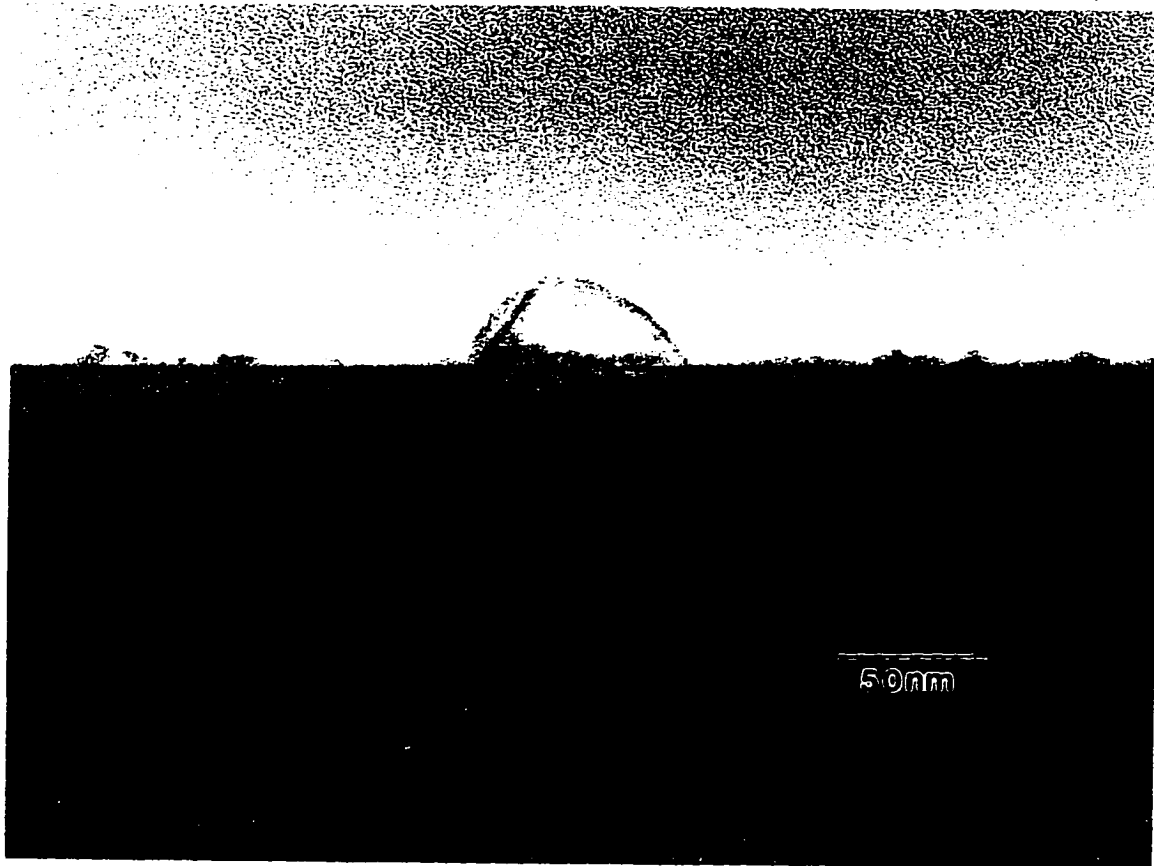


Figure 4.10 HRTEM image of a bimodal distribution in $\text{Al}_{0.45}\text{Ga}_{0.55}\text{P}$ islands at $T_G=550^\circ\text{C}$.

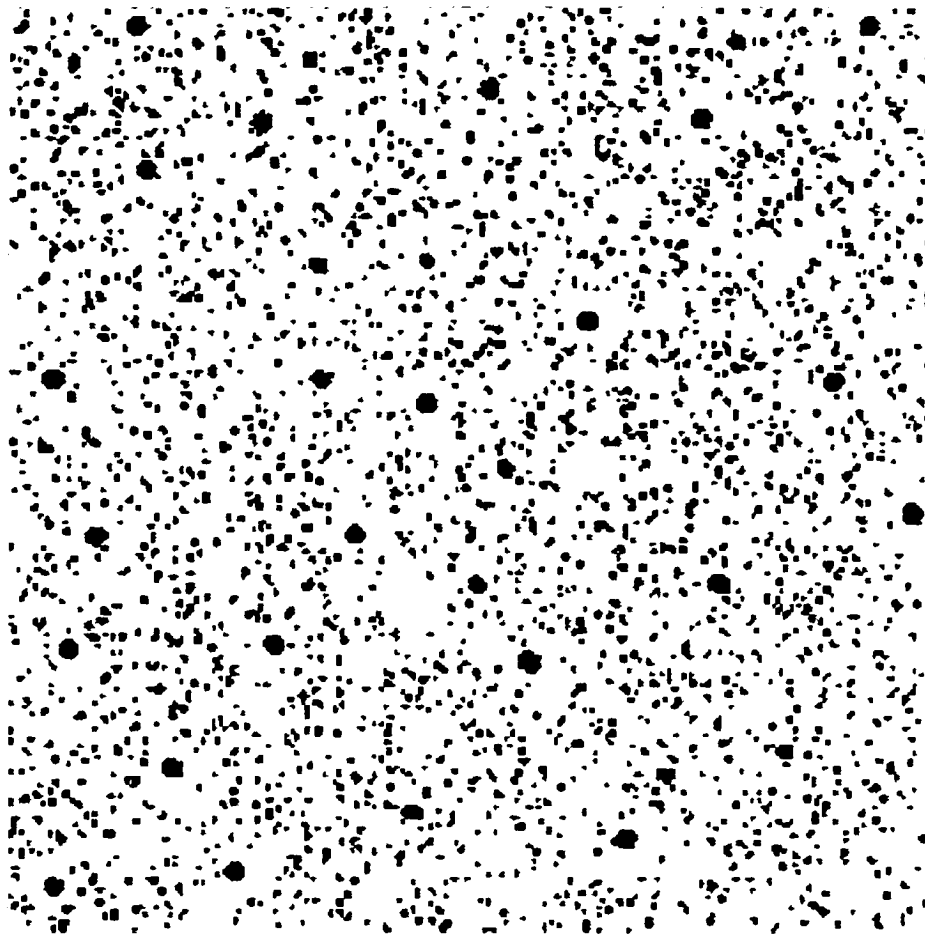
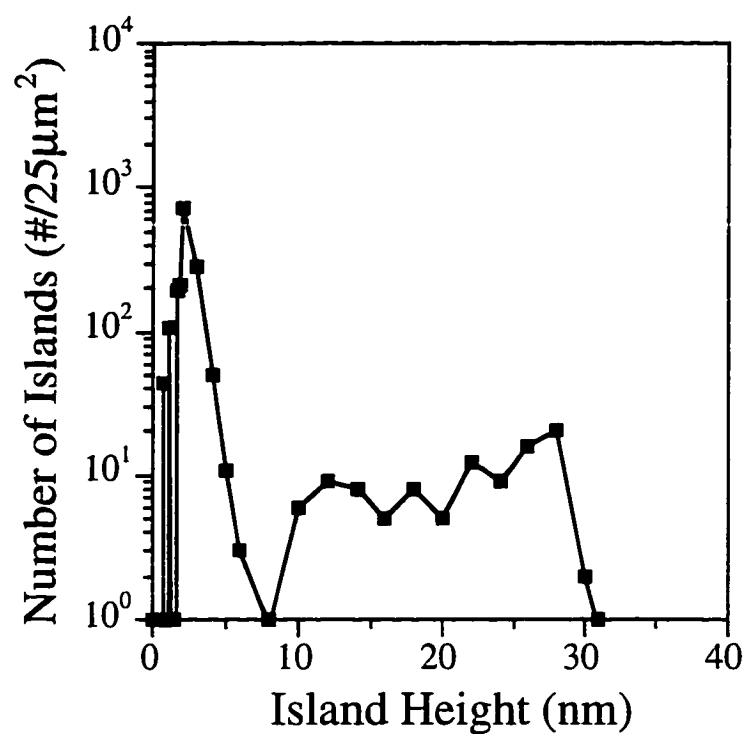
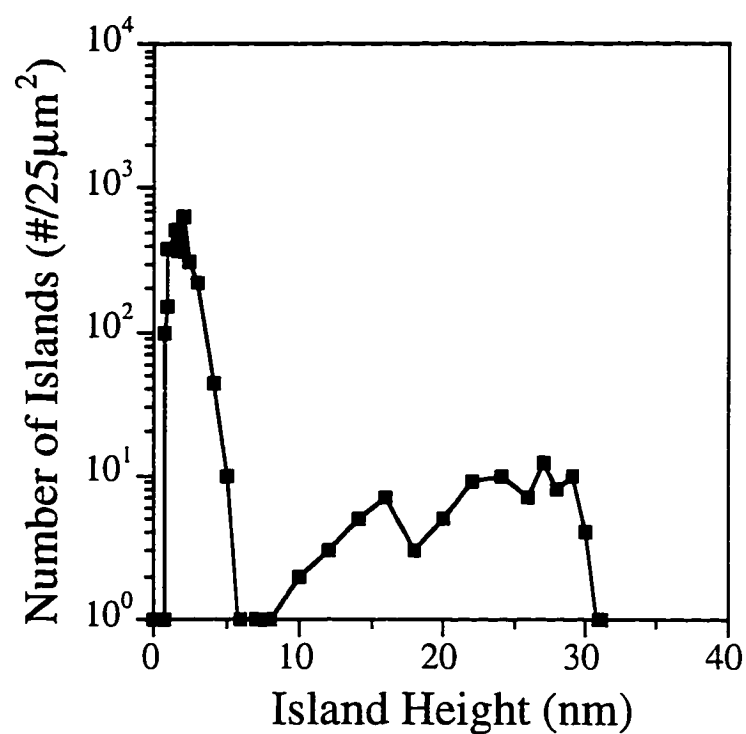


Figure 4.11 Top-view AFM image of bimodal distribution showing the apparent depletion areas around the larger islands in $\text{Al}_{0.3}\text{Ga}_{0.7}\text{P}$ at $T_G=550^\circ\text{C}$.



a)



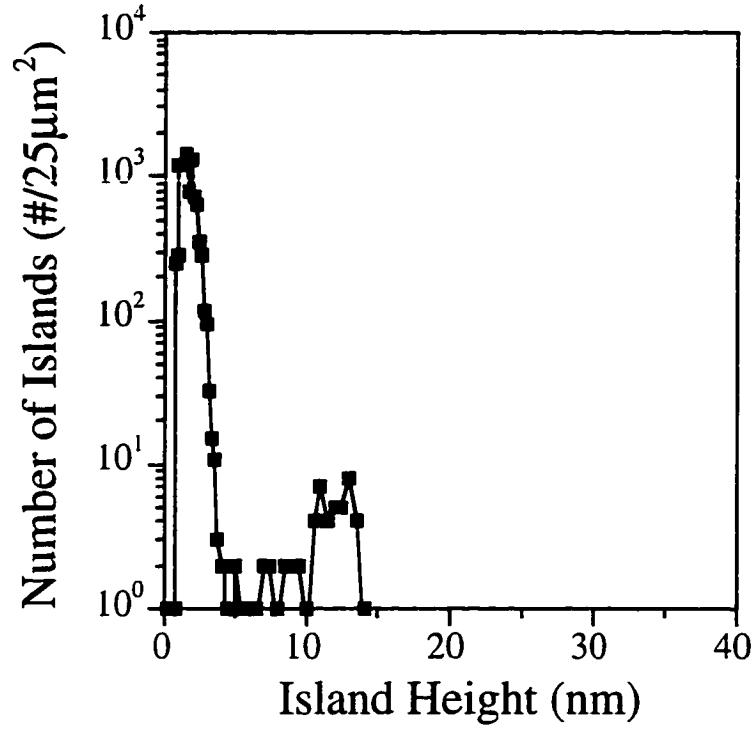
b)

Figure 4.12 Island height distribution for $\text{Al}_x\text{Ga}_{1-x}\text{P}$ at $T_G=550^\circ\text{C}$ for a) $x=0.15$ and b) $x=0.45$.

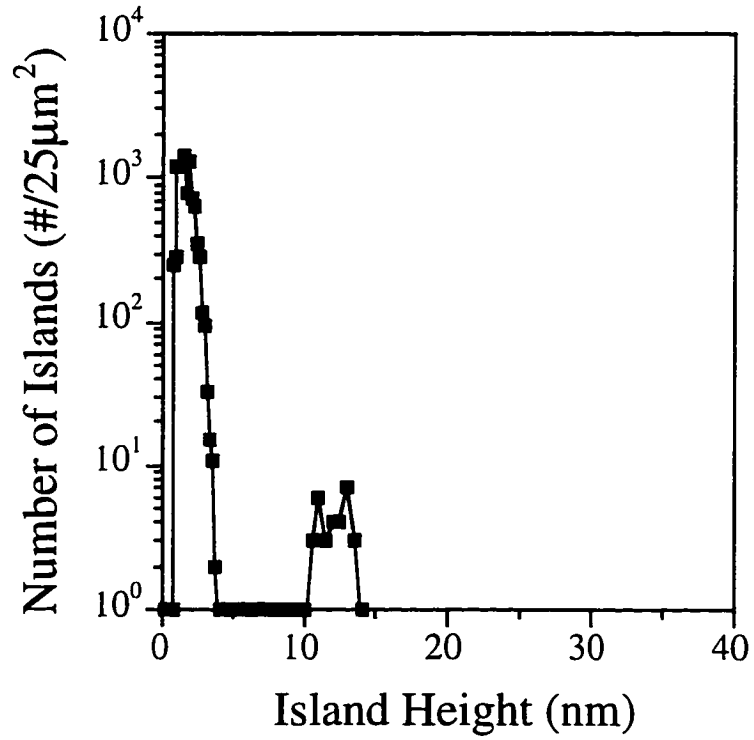
Additional growth runs were conducted with varying growth conditions in order to further understand the effects of each growth parameter on the nucleation of the $\text{Al}_x\text{Ga}_{1-x}\text{P}$. The effects of growth rate were examined by growing samples with the wafer rotation turned off. Rotation of the substrate is necessary during growth runs on the Varian Gen II MOMBE system because the group III source injectors are not perpendicular to the wafer. Due to this slight offset, the part of the wafer closest to the group III source will experience a slightly higher growth rate than the side of the wafer furthest away from the injector. The change in growth rate across the wafer is expected to be approximately 15% while the composition remains constant. Two such samples were grown under identical conditions with the exception of growth time. Figure 4.13 shows the island distributions for a deposit of 100\AA of $\text{Al}_{0.45}\text{Ga}_{0.55}\text{P}$ grown at 500°C for each side of the wafer illustrating each growth rate extreme. Note that the variance in island height distributions is small.

The effects of phosphine flow variations on the $\text{Al}_x\text{Ga}_{1-x}\text{P}$ nucleation were also examined at a fixed growth rate. Phosphine flows of 0.6, 2.8, and 10 sccm were studied in addition to the 2 sccm used throughout the experiments. Figure 4.14 shows the top-view AFM images of the $\text{Al}_{0.45}\text{Ga}_{0.55}\text{P}$ samples grown at $T_G=500^\circ\text{C}$ where a notable difference in nucleation can be seen, and figure 4.15 shows the overlaid island height distributions for each of the four samples. Changes in island height distribution are found to occur with large changes in phosphine flow.

Finally, the effect of hydrogen desorption from the silicon surface on the $\text{Al}_x\text{Ga}_{1-x}\text{P}$ nucleation was examined. After surface preparation, the surfaces of the silicon wafers were hydrogen terminated. Upon exposure to growth temperatures exceeding 450°C , the hydrogen desorbs and a phosphorous terminated (2×1) silicon surface is expected. The effect that this change in surface termination has on nucleation over the temperature range of 450°C - 550°C was not known. Therefore, a single wafer was exposed to a pregrowth temperature of 600°C to insure complete hydrogen desorption, and then cooled down to 500°C for deposition of $\approx 50\text{\AA}$ of $\text{Al}_{0.45}\text{Ga}_{0.55}\text{P}$. The island height histogram for this



a)



b)

Figure 4.13 AFM island height distributions for $\text{Al}_{0.45}\text{Ga}_{0.55}\text{P}$ at $T_G=500^\circ\text{C}$ showing the effects of both a) high and b) low growth rates on the nucleation.

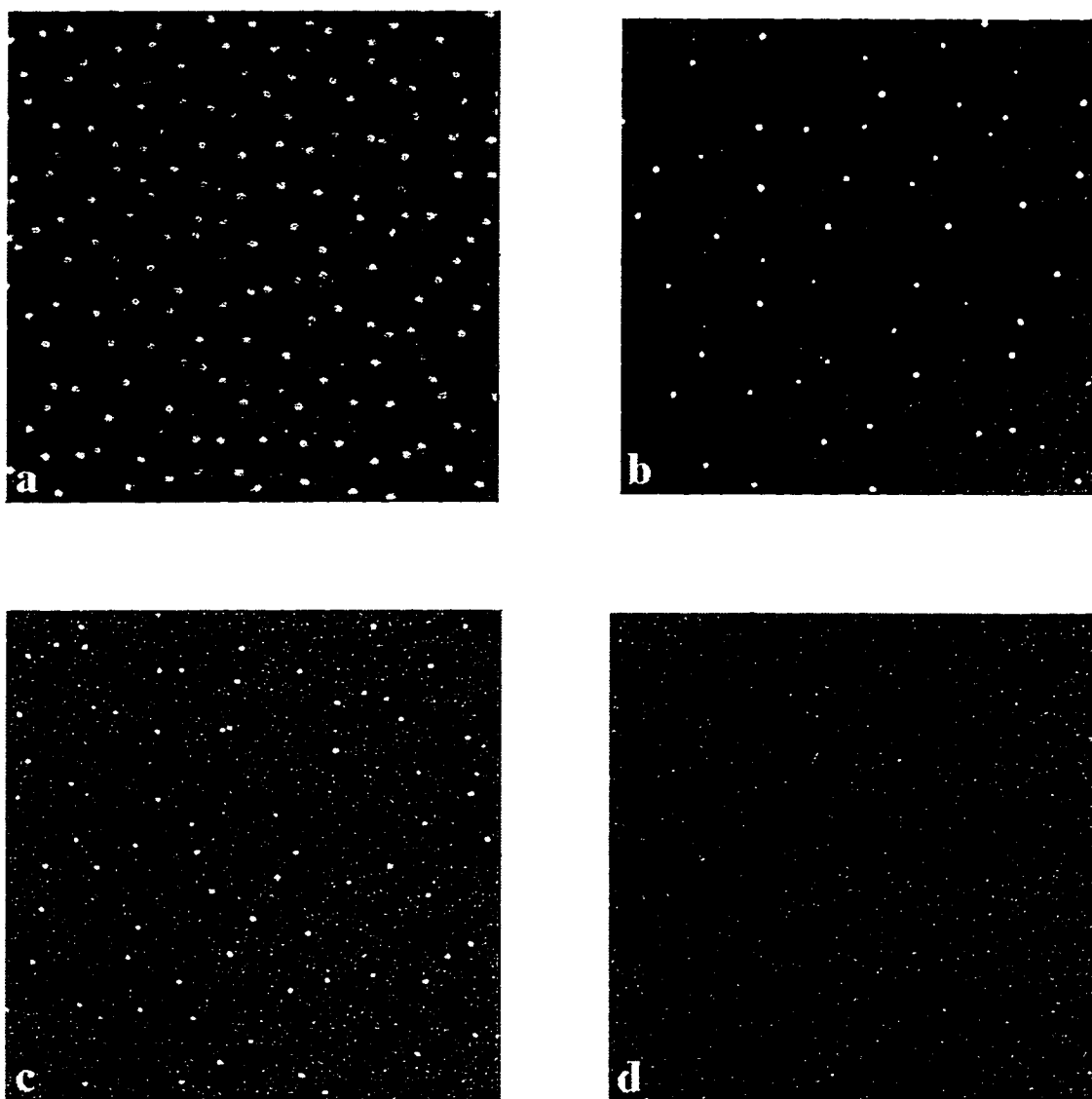


Figure 4.14 AFM top-view images of $\text{Al}_{0.45}\text{Ga}_{0.55}\text{P}$ at $T_G=500^\circ\text{C}$ for phosphine flow rates of a) 0.6, b) 2, c) 2.8, and d) 10sccm.

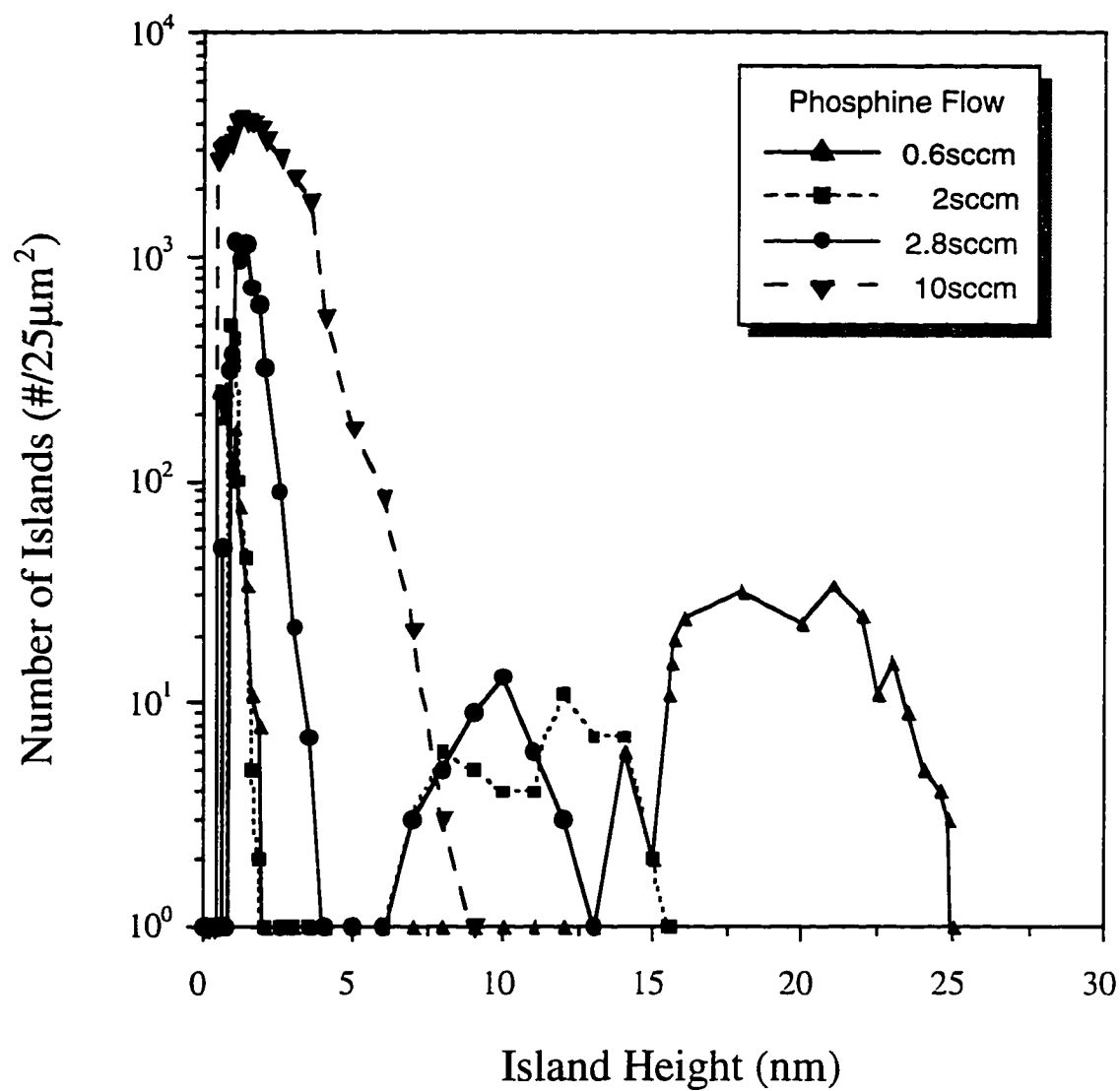


Figure 4.15 Island height distributions of $\text{Al}_{0.45}\text{Ga}_{0.55}\text{P}$ at $T_G = 500^\circ\text{C}$ for phosphine flow rates of 0.6, 2, 2.8 and 10 sccm.

sample is shown in figure 4.16 which still exhibits a bimodal nucleation but with a slightly lower large-island density.

4.3 Discussion of the Initial Stages of Growth

In most cases, depending on the surface energies of the film and substrate, and the lattice mismatch, the islanded film represents the equilibrium state [17]. However, planar film technology has made several advances in deposition which permit layer growth by limiting the surface kinetics in order to fabricate flat nonequilibrium structures. The nucleation and growth of AlGaP islands on the silicon substrates by MOMBE proceeds through many surface processes that are thermodynamically driven and kinetically limited. Identification of each one of the factors affecting growth and their influence on the severity of island formation will help in the understanding of the nucleation process. Therefore, thermodynamics of thin film growth and kinetics of deposition are considered and applied to the discussion of the observed nucleation.

Growth of 50Å of $\text{Al}_x\text{Ga}_{1-x}\text{P}$ on silicon substrates by MOMBE resulted in island formation for every growth condition studied in these experiments. The severity of island growth could be controlled however, such that surface roughness was minimized after island coalescence. Changes in aluminum concentration were found to modify the island size and density distributions but did not induce planar growth. These results contrasted with the findings of Gerooge et al. [4] where they found that increased additions of Al to the $\text{Al}_x\text{Ga}_{1-x}\text{P}/\text{Si}$ system grown by MOCVD had suppressed the tendency for island formation.

An intriguing result of the MOMBE $\text{Al}_x\text{Ga}_{1-x}\text{P}/\text{Si}$ nucleation studies was the formation of bimodal distributions. Bimodal island sizes have been observed previously in GaAs/Si [102], InAs/GaAs [103], and in AlSb/GaAs [104] material systems, but the explanations for their presence are varied. In the growth of MBE InAs/GaAs [103], the existence of the larger islands was attributed to the accelerated growth of relaxed islands. The relaxed islands were believed to act as sinks for surface mobile cations, and due to the

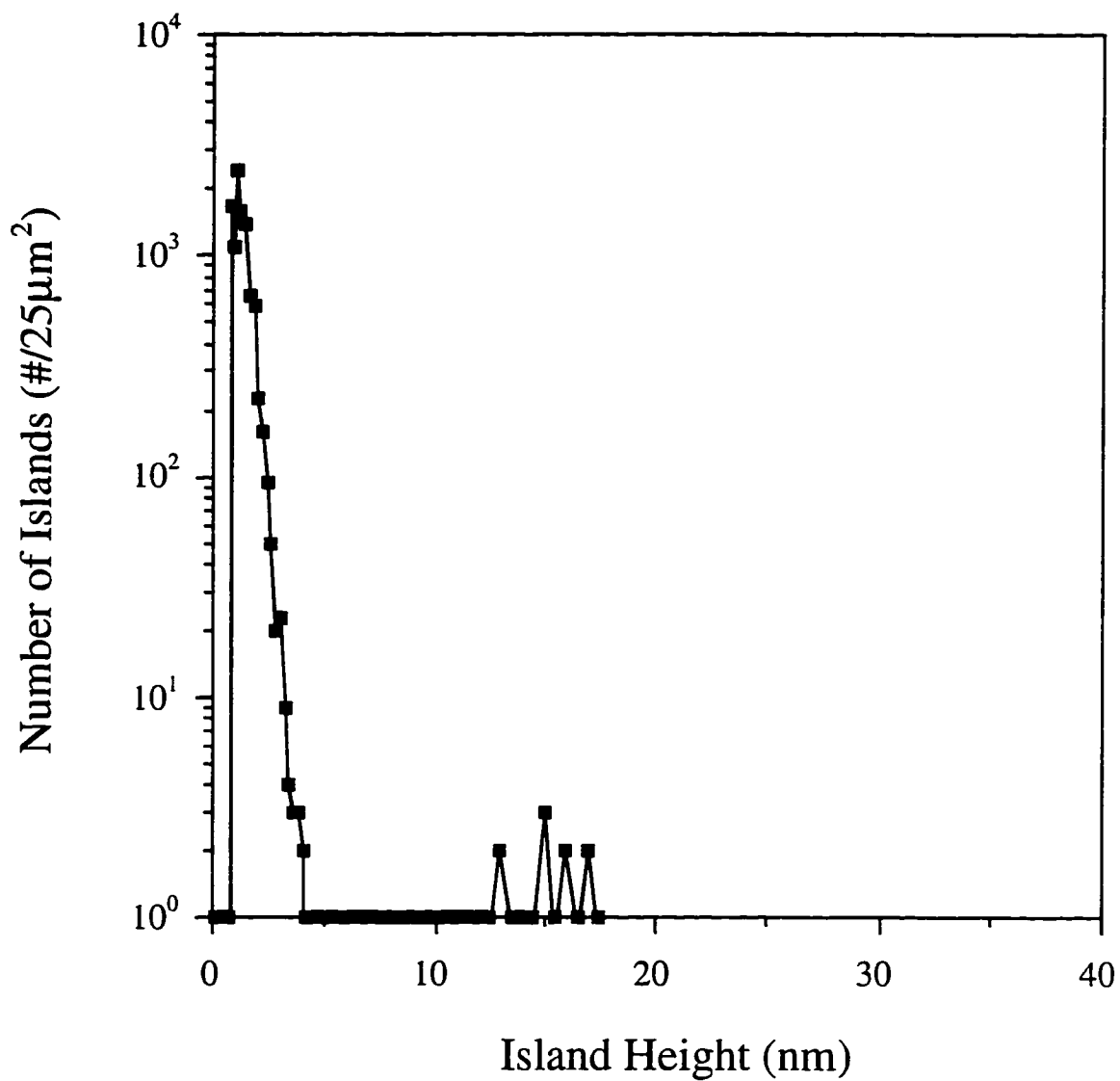


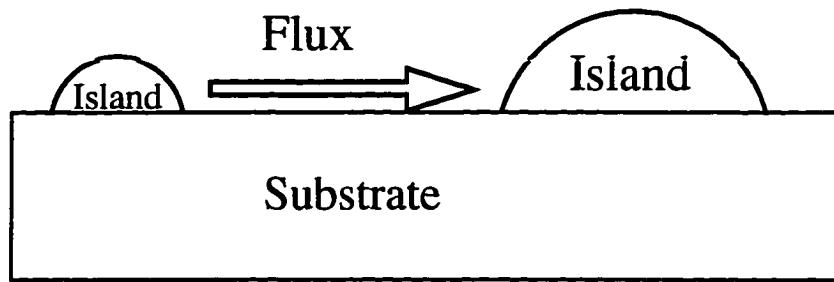
Figure 4.16 AFM island height histogram of $\text{Al}_{0.45}\text{Ga}_{0.55}\text{P}$ at $T_G=500^\circ\text{C}$ with a pregrowth temperature exposure of 600°C .

high surface mobility of In on GaAs, the islands grew without restriction. Yoon et al. [102] observed a bimodal distribution of GaAs islands on silicon in MOCVD. They attributed bimodal island sizes to reoxidation of parts of the silicon substrates resulting in high surface diffusional fluxes of As and Ga for the abnormal growth of larger islands. And lastly, the bimodal growth in the AlSb/GaAs system was simply an observation and not explained. We thus have two very different explanations for two similar observations. In the following discussion, the reasons for bimodal nucleation in the $\text{Al}_x\text{Ga}_{1-x}\text{P}/\text{Si}$ material system are given and the effects of variations in growth conditions on the nucleation are detailed.

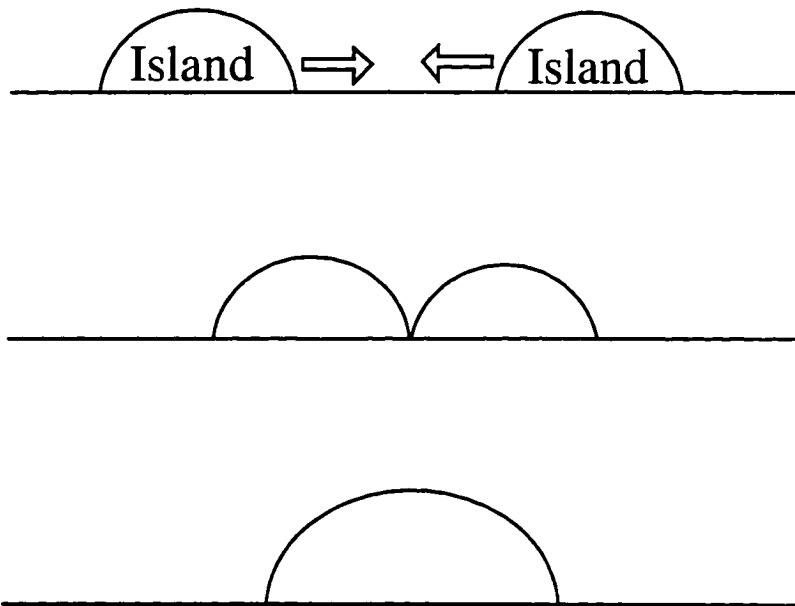
Small island sizes remained fairly constant in the Al containing deposits as the formation of large islands occurred, creating a bimodal distribution of island sizes. The GaP island sizes, however, had large size deviations which led to broad island distributions with increased growth temperatures showing typical nucleation and three-dimensional island growth [101]. GaP did not show the presence of a bimodal size distribution, therefore, the formation of the bimodal distribution is believed to be a consequence of adding Al to GaP.

In order for islands to grow, there must be sufficient transport of surface species and/or existing islands. For a heteroepitaxial system that grows by 3D island nucleation such as $\text{Al}_x\text{Ga}_{1-x}\text{P}/\text{Si}$, the mobility of the precursors on the surface will ultimately determine the morphology of the deposit. Growth conditions and surface species that give rise to easy surface transport will lead to structures that are closer to their equilibrium state. Therefore, to explain the formation of the bimodal distribution, the surface kinetics and growth processes on the silicon substrates in MOMBE must be understood.

Island growth can occur by two possible mechanisms; ripening or clustering as shown in figure 4.17. These processes may occur during deposition (nonconservative state) or when there is no deposition (conservative state). Ripening of islands is defined to be the growth of larger islands at the expense of smaller islands. Mass transport through surface diffusion of atomic species is the mechanism by which the larger islands grow.



a)



b)

Figure 4.17 Schematic of a) a small and large island on a surface with a flux of atomic species to the larger island (ripening), and b) the progression of island coalescence.

The total surface energy of the system decreases with ripening and the surface to volume ratio of the deposit is reduced as well. At a finite temperature, there is a probability for atoms to escape from an island, and through surface diffusion, attach to another island. The flux of atoms from an island is dependent on its size. There is some mass transport away from the large islands, but the major motion of atomic species is from the smaller to larger islands with a net increase in average island size.

The other island growth process is called coalescence and is shown in figure 4.15b. This process is the merging of two existing islands into one and is driven by the decrease in the surface energy where the larger island represents a lower energy state than the two separate islands.

During the early stages of island growth, the density of the islands is expected to increase with deposition time to some maximum value before decreasing through ripening and/or coalescence [13]. The major driving force for ripening is due to a concentration gradient of material associated with the differences in vapor pressure over different sized islands [105]. The vapor pressure over a small island is larger than the vapor pressure over a large island as shown by Kelvin's equation [105]:

$$\frac{p}{p_0} = \exp\left(\frac{2\gamma\Omega}{rkT}\right)$$

where p is the pressure above an island of radius r , Ω is the atomic volume of the island, γ is the surface energy, and p_0 is the equilibrium pressure which is defined as the pressure if there was no island (i.e. $r \rightarrow \infty$).

Table 4.2 shows the effective pressures over small islands at several different temperatures and values of island radius. Note that for a island with a radius greater than 10nm there are only minor enhancements in effective pressure above small islands, however values over islands smaller than 10nm become very large. The small island heights of $\text{Al}_x\text{Ga}_{1-x}\text{P}$ were less than 5nm and the large island heights were $\geq 5\text{nm}$ leading to

a large difference in pressures above the islands. This large pressure difference is a significant driving force for large-island growth.

The enhanced vapor pressure over the different sized islands sets up concentration gradients which provide the driving force for surface diffusion and island growth via ripening. The occurrence of ripening depends on the relative binding energies of the migrating species. The surface diffusion of the migrating species can be enhanced enormously by the presence of impurity adsorbates which can facilitate the ripening process [13]. Increases in temperature lead to a decrease in the driving force for island ripening, however increases in temperature also allow for easier surface transport and atom detachment from smaller islands facilitating the system's approach towards equilibrium.

Table 4.2 Values of p/p_0 using Kelvin's for $\gamma=10^{15}$ eV/cm² and $\Omega=20 \times 10^{-24}$ cm³.

r (nm)	p/p_0		
	300K	600K	900K
1	4.88×10^6	2.2×10^3	5.1
10	4.66	2.16	1.67
100	1.17	1.08	1.05

The chemical potential, which influences the growth mode, is also dependent on the shapes of the islands. The curvature dependence of the chemical potential is given by the following equation [106]:

$$\mu = \mu_0 + V_m \gamma \kappa$$

where κ is the mean curvature and μ_0 is the chemical potential of an atom at a flat interface, V_m is the molar volume and γ is the surface energy. Assuming an isotropic surface energy, it can be seen from the above equation that the atoms will flow from regions of high to low curvature, i.e., from high to low chemical potential regions.

Strain energy can also be a driving force for large-island formation. Incoherent islands have been found to have increased growth rates relative to coherent islands since the relaxed islands act as sinks for surface mobile cations [107]. An island growth model by Drucker [108] predicts an accelerated growth rate for relaxed islands which has been shown experimentally by Krishnamurthy and co-workers [107]. In fact, the relaxed island growth was used to explain the bimodal growth of islands. The extent of relaxation in the MOMBE grown AlGaP islands is not known. However, the majority of the islands have planar defects even at these early stages of growth. In addition, the lattice mismatch of the $\text{Al}_x\text{Ga}_{1-x}\text{P}/\text{Si}$ system is relatively unchanged as x is increased from 0 to 0.45 (mismatch changes less than a tenth of a percent). Therefore, a significant driving force for large-island formation arising from changes in lattice mismatch and/or relaxed island sinks does not appear to explain the presence of the bimodal distribution in $\text{Al}_x\text{Ga}_{1-x}\text{P}$ on silicon in MOMBE.

In order for islanding to occur, facile surface diffusion of the precursor species must exist. Surface diffusion of adatoms is represented by the following equation:

$$D = D_0 \exp\left(\frac{-E_a}{kT}\right)$$

which depends on the activation energy for diffusion and growth temperature. The adatom must first overcome an activation barrier E_a to move which will depend on the surface site and on the binding strength of the adatom to the substrate. From Pauling [109] and Sanderson [110], the binding energy between Al-Si > Ga-Si. The increased binding

strength or interaction between Al and Si has been used to explain the smoothening effect of the $\text{Al}_x\text{Ga}_{1-x}\text{P}$ films grown by MOCVD. However, the extent to which this interaction occurs is only a few monolayers and group V coverage of the substrate should be considered as well. In addition, the activation energy for surface diffusion may be influenced by such factors as substrate surface treatment and surface impurities.

In MOMBE, the overall diffusion coefficient will involve contributions from all possible mobile species.

$$D = \sum_i D_i$$

The surface species present on the wafer surface are determined by the decomposition processes of the DMEAA and the TEG. For the DMEAA, the reaction on the heated substrate is fairly straight forward and leads to very low impurity incorporation [55]. The Al:N bond is broken in the molecule resulting in physisorbed AlH_3 . The hydrogens quickly leave the unstable hydride resulting in an adsorbed Al adatom and a desorbed amine. For TEG, the decomposition process is a little more complicated. Robertson et al. [51] pioneered the model for the decomposition of TEG in the growth of CBE (Chemical Beam Epitaxy) GaAs using As_2 . Figure 4.18 illustrates the reported surface pyrolysis processes from initial adsorption of the TEG molecule to the final incorporation of the Ga atom.

The model assumes the existence of adsorbed triethyl, diethyl, and monoethyl gallium species as well as adsorbed ethyl radicals. All DEG radicals are assumed to go on to produce atomic gallium. In addition, the recombination and desorption reactions of MEG are not included in the model as the cleavage of the last alkyl-gallium bond is assumed to be fast relative to the preceding steps and irreversible.

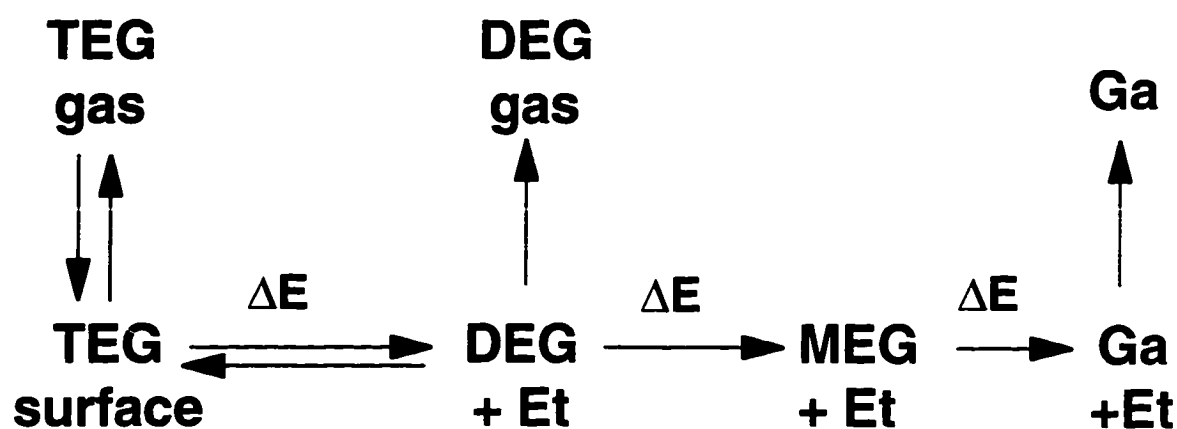


Figure 4.18 Reaction mechanisms for the TEG surface chemical kinetics during CBE growth.

From figure 4.18, the decomposition of the TEG proceeds first through the physisorption of the TEG molecule onto the heated substrate surface. The adsorbed TEG molecule can either overcome the activation energy needed to break the first ethyl-gallium bond producing adsorbed DEG and ethyl radicals, or desorb from the surface. From this point, the adsorbed DEG has three reaction pathways in which it can follow: it may recombine with an adsorbed ethyl radical to form adsorbed TEG, it may desorb from the surface, or it may further decompose into a Ga adatom and ethyl radicals. Note that the population of ethyl radicals on the surface is increased for each breaking of a ethyl-gallium bond. Desorption of the excess ethyl species may occur by the elimination of atomic hydrogen to form ethylene (C_2H_4) which leaves the surface rapidly. Surface ethyl radicals can also be scavenged by other surface species and end up incorporated into the growing film. In CBE, the group III species controlling the growth rate are not necessarily adsorbed gallium atoms since highly mobile alkyl-gallium radicals may also have a role in the epitaxial incorporation process [51]. With this decomposition model in mind, the explanation for the bimodal growth is given.

As noted in the HRTEM data, modified AFM images suggested the existence of depletion zones around the larger AlGaP islands. Figure 4.11 shows an AFM image of $\text{Al}_{0.3}\text{Ga}_{0.7}\text{P}$ nucleated at 550°C with areas around the larger islands that are free of small islands. The formation of the larger islands may be occurring by ripening where large islands grow at the expense of the smaller surrounding islands. The presence of larger islands and depletion regions surrounding them suggest that the surface mobility of group III species may be enhanced with increasing aluminum composition as these areas are not observed with lower Al concentrations at lower growth temperatures. This mobility enhancement is proposed to arise from the gettering of adsorbed ethyl radicals by the Al adatoms as shown in figure 4.19. Ethyl radicals are believed to be adsorbed to the substrate surface as part of the decomposition process of TEG which may be gettered by the Al forming a strong Al-C bond. If this process were indeed occurring, then it would be expected that the carbon concentration in the AlGaP thick films would increase with increasing Al composition. SIMS analysis of thick $\text{Al}_x\text{Ga}_{1-x}\text{P}$ films revealed that the carbon concentration in the films increased with increases in Al concentration as shown in figure 4.20. Carbon incorporation in the GaAs material system has also been shown to increase with the presence of aluminum [111,112]. Therefore, assuming the Robertson model holds true for a silicon substrate, it is proposed that the Al adatoms getter adsorbed ethyl radicals from the TEG decomposition process, weakening the Al-substrate interaction, and allowing the Al to move more freely on the surface towards a more equilibrium state, if such a state exists.

Lee et. al.[111] used quadrupole mass spectroscopy to analyze the desorption mass spectra from the growth of AlGaAs in MOMBE using TEG and elemental Al. They found a large increase in the $m/e=57$ and 85 peaks when the populated GaAs surface was exposed to an elemental Al flux. These peaks were attributed to $\text{H}\cdot\text{Al}\cdot\text{C}_2\text{H}_5$ and $\text{Al}(\text{C}_2\text{H}_5)_2$ and were explained by the transfer of ethyl groups from the gallium species to atomic

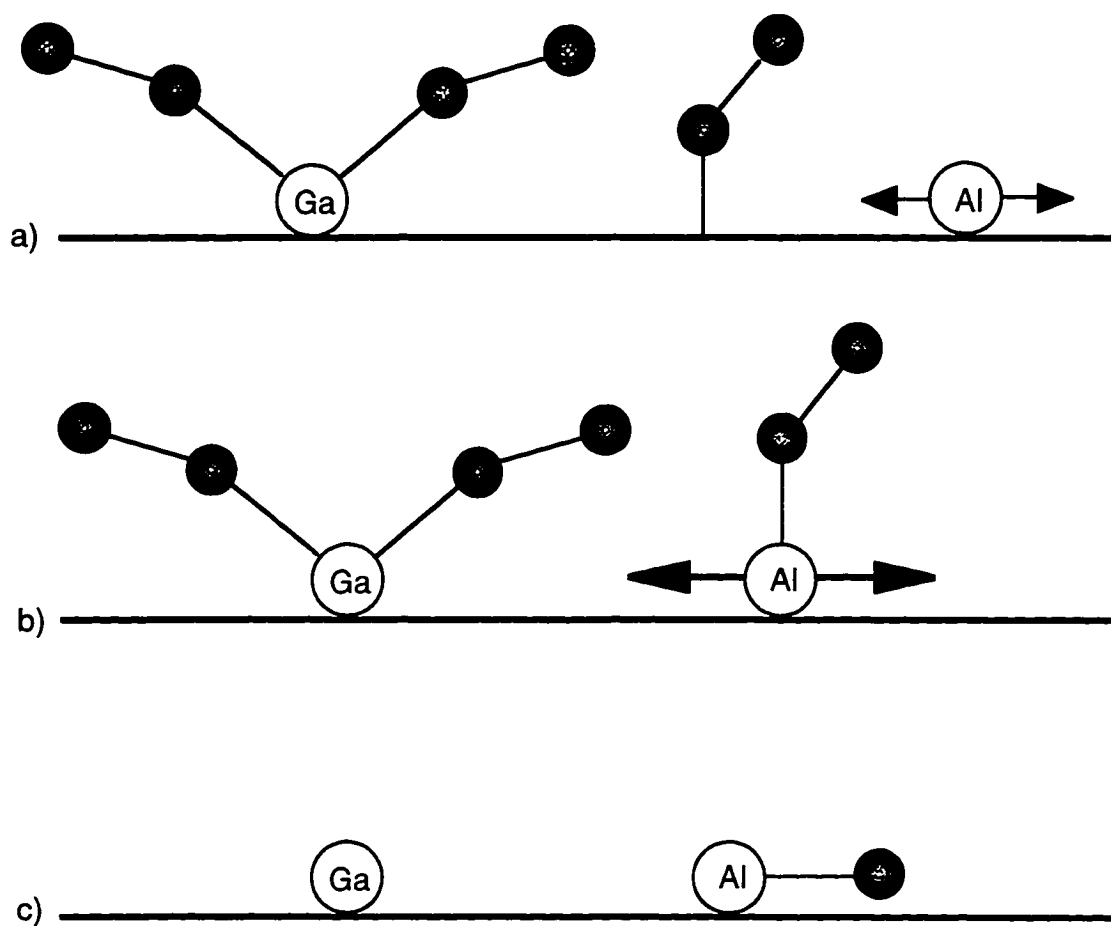


Figure 4.19 Illustration of the proposed model for Al adatom mobility enhancement.
 a) physisorbed DEG, ethyl radical and Al adatom
 b) physisorbed DEG and Al-ethyl species with enhance mobility
 c) incorporation of Ga and Al-C into film

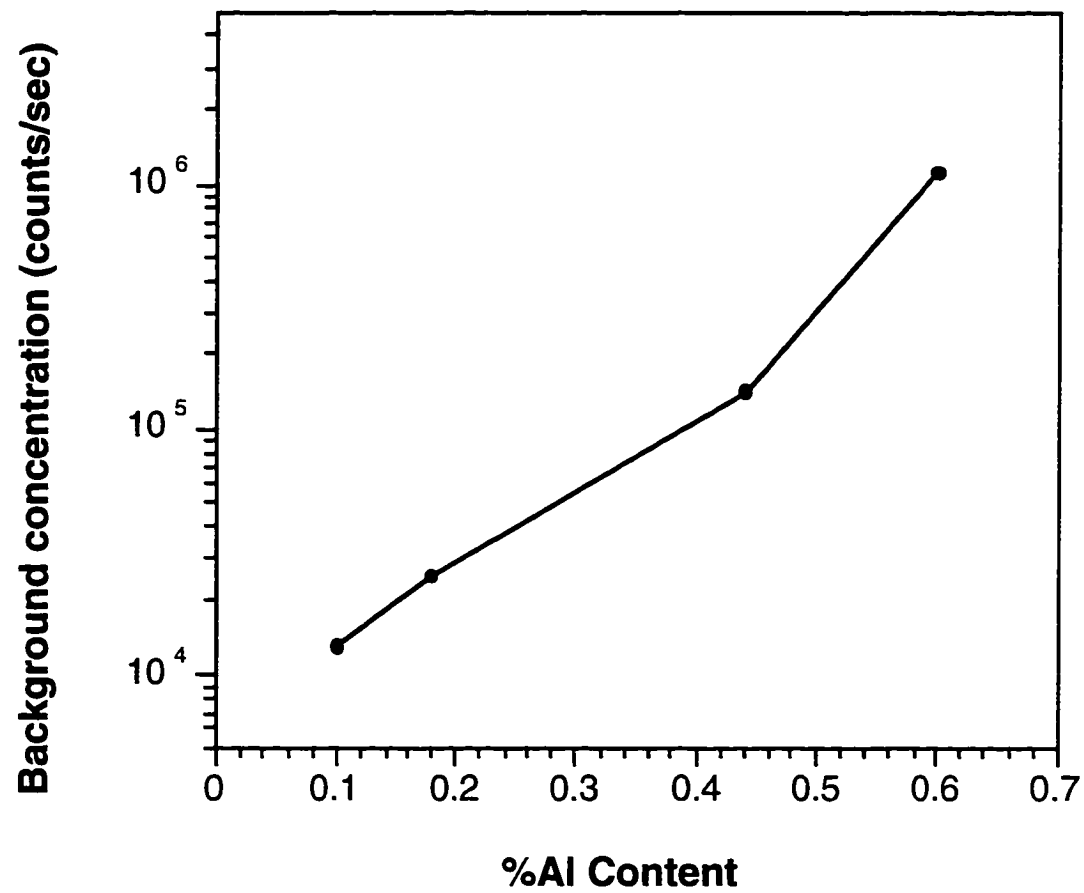


Figure 4.20 Relative carbon concentration in $\text{Al}_x\text{Ga}_{1-x}\text{P}$ films as a function of aluminum content.

aluminum. The gettering ability of the Al may also increase the mobility of the Ga species by decreasing site-blocking effect by ethyl radicals.

For MOMBE grown $\text{Al}_x\text{Ga}_{1-x}\text{P}$ on silicon, the more predominant island growth mechanism is thought to be island ripening due to the presence of depletion regions around the larger islands. Since the growth of $\text{Al}_x\text{Ga}_{1-x}\text{P}/\text{Si}$ occurred by island formation, the driving force for island ripening existed (due to island size variations) for each composition and temperature studied. However, due to the kinetics of the system, the island densities and geometries were found to vary from sample to sample.

Differences in the growth morphologies with temperature indicate the importance of thermally-activated kinetic processes. As the temperature is lowered a greater deviation from equilibrium is manifested into the morphology of the grown layer. At growth temperatures of 550°C , the energy for surface diffusion of the surface species was obtained through kT and the aluminum concentration of the ternary showed no apparent affect on the distribution of the islands. However at lower temperatures, the necessary energy for surface diffusion was limited to those surface species with lower activation energies for diffusion. As the aluminum composition of the ternaries was increased, an increase in the number of large islands was observed which has been attributed to an enhancement in the surface mobility of aluminum. There was also a difference in the large island densities for the samples grown at 450° versus 500°C which demonstrates that the kinetics available to the system plays a vital role in the resulting surface morphology and final film structure.

There are several other considerations that must be taken into account to explain the nucleation of $\text{Al}_x\text{Ga}_{1-x}\text{P}$ on silicon in MOMBE. These include: surface reconstruction, hydrogen desorption, group V flow, growth rate and net volume of deposit. For a clearer understanding of the nucleation of the material system, each of these issues is now addressed.

Surface reconstruction may influence the surface mobilities of the precursor species. In fact, differences in surface reconstruction on a single wafer surface are

attributed to the different orientation of grains in the growth of some thin films [113]. A simple truncation of the bulk Si(001) structure leaves the atoms on the top surface with two bonds directed to the layer below and two dangling bonds on the surface. After exposure of a silicon wafer to HF solutions, the surface is hydrogen passivated and shows a (1x1) bulk-like surface structure. The energy of an unpassivated silicon surface can be reduced if neighboring pairs of silicon surface atoms bond, forming a pattern of surface dimers (2x1 reconstruction). Differences in surface reconstruction amongst silicon wafers used in these experiments are not expected for each growth temperature. However, with increased growth temperatures, there may be a change in reconstruction due to the loss of hydrogen and the gain of phosphorous termination.

Hydrogen passivation of the silicon surface has been shown to decrease the bonding strength of some elements on the silicon surface as well as increase their likelihood to desorb from the surface [114]. Therefore, it may be argued that large-island formation may occur more easily on a hydrogen passivated surface. In the growth of the $\text{Al}_x\text{Ga}_{1-x}\text{P}/\text{Si}$ system in MOMBE on hydrogen passivated surfaces, the diffusion of the group III precursors may effectively be changed at different stages of hydrogen surface coverage. It is expected that at the three different growth temperatures studied, the percent of hydrogen termination on the silicon surface is different due to hydrogen desorption at higher temperatures. Hydrogen loss from the (1x1) terminated silicon surface due to desorption occurs over the temperature range of 450-510°C [80] leading to an unpassivated (2x1) reconstructed silicon surface [71]. However, in the presence of a P_2 beam the surface forms a (2x1) P dimered surface [115] which may influence surface diffusion behavior.

To examine this effect, a hydrogen terminated silicon wafer was exposed to a temperature of 600°C and a P_2 beam, and then cooled down to $T_G=500^\circ\text{C}$ for growth of $\text{Al}_{0.45}\text{Ga}_{0.55}\text{P}$. This composition ($x=0.45$) and growth temperature ($T_G=500^\circ\text{C}$) has already been shown to produce a bimodal nucleation. The effect of hydrogen passivation

was found to result in a higher density of large-islands suggesting a higher surface diffusivity of the group III species as shown in figure 4.16. Therefore, the loss of hydrogen termination with increased temperature cannot be attributed to the formation of bimodal growth although its presence may be an important factor.

Precursor surface interactions may play an important role in determining the MOMBE growth process as well. In MBE, increases in the group V flow to the sample surface have been found to change the nucleation and growth behavior of films [116]. With MOMBE, the chemical reaction mechanisms are a little more complicated than those in MBE and may show different effects. Roberston's model for TEG decomposition in the growth of GaAs assumes the role of the arsenic species to be secondary. However, the influence of increased arsine flow has been reported to decrease the growth rate of GaAs presumably by the so called site-blocking effect in MOMBE using TEG and arsine [117].

The effect of different phosphine flow rates was examined in the growth of $\text{Al}_{0.45}\text{Ga}_{0.55}\text{P}$ at 500°C by MOMBE as shown in figures 4.14 and 4.15. The tendency for bimodal growth became more severe with low phosphine flows and was suppressed with the use of high phosphine flows. The suppression is believed to be a result of a decrease in the effective diffusion length of the group III atoms through the site-blocking effect of the group V. The changes made in the phosphine flow presumably did not influence the composition of the ternary as the stoichiometric alloys are always grown under a surplus of group V species. However, the V/III ratio was changed and this parameter has been reported to influence the nucleation morphology at the early stages of growth [118]. Therefore, we examined the effects of changes in the V/III ratio (i.e. group V flow) on the island height distributions.

The Al concentration of the ternaries was increased by increasing the flow of the DMEAA while maintaining the TEG and phosphine flows. This decreased the V/III ratio for each composition and increased the growth rate. V/III ratios in MOMBE cannot be measured easily by ion gauges in the growth chamber, as they are in MBE, because of the

use of corrosive metal-organics and high hydrogen background pressures [119]. Another problem is that the V/III ratio at the substrate surface depends on the growth temperature, thus it is different from the beam flux ratio. Because of these reasons, an alternative approach was used to compare the effects of the V/III ratio.

In MOMBE, the growth rate of a III-V material is linearly dependent on the flow of the group III for normal growth temperatures[60]. Phosphine flow has been shown only to have a minor effect on the growth rate for GaP [60]. Therefore, a value for the V/III was assumed to be some arbitrary value for one of the $\text{Al}_x\text{Ga}_{1-x}\text{P}$ ternary compositions and compared to the other alloys through calculations involving their respective growth rates. At 500°C, the growth rates for 15, 30 and 45% Al were 1, 1.2 and 1.4 $\mu\text{m/hr}$ respectively. Assuming a V/III ratio of 5 for the 15%Al, the V/III ratios of the other compositions can be calculated and compared as shown in table 4.3. Note that differences in the V/III ratio are small, and from figure 4.15, small changes in the phosphine flow did not significantly change the morphology of the nucleation (i.e. compare 2 and 2.8 sccm). To observe a change from a single island distribution to a bimodal one would require a large change in the V/III ratio which does not occur as the concentration of aluminum in the ternary is increased from 15-45%. Therefore, although large changes in the group V flow have dramatic effects on the island morphologies of the $\text{Al}_x\text{Ga}_{1-x}\text{P}$, the small changes in V/III ratio for each composition are not expected to result in the suppression or enhancement of the bimodal distribution.

Variations in the growth rate can also effect the morphology of heteroepitaxial deposits. Grandjean et al. [120] have shown that large changes (a factor of 3-4 increase) in growth rate can delay the onset of islanding in the InGaAs/GaAs system by effectively decreasing the mass transport on the substrate surface in MBE. Growth rate changes were found to decrease the effective surface diffusion length of the group III adatoms shifting the InGaAs layers further from their equilibrium situation for which a 3D morphology was predicted. Under low growth rate conditions, the InGaAs deposits grew layer-by-layer for

Table 4.3 Calculated values of the V/III ratio assuming an arbitrary value* for $x=15\%$ Al at $T_G=500^\circ\text{C}$

X (Al%)	Growth Rate ($\mu\text{m/hr}$)	V/III
15	1	5*
30	1.2	4.1
45	1.4	3.5

about 3-4 monolayers before islanding was observed and with higher growth rates, this transition was not observed until about 12-16 monolayers of coverage.

Although the layer-by-layer growth mode was not observed in the growth of $\text{Al}_x\text{Ga}_{1-x}\text{P}$ on silicon in MOMBE, the island morphology was found to be influenced by several growth factors. The effect of growth rate was explored because of the small changes (less than a factor of 2 change) in growth rate existing between the different compositions at each growth temperature. With the substrate rotation off, the growth rate across the substrate varies about 15% from one side of the wafer to the other. The results of the growth rate experiment are shown in figure 4.13 where it can be seen that a slight change in large-island density was found but that this degree of growth rate change is not sufficient to suppress or enhance the bimodal nucleation. Therefore, the small changes in growth rate between the different compositions is not believed to play an major role in determining the $\text{Al}_x\text{Ga}_{1-x}\text{P}$ island distributions on silicon in MOMBE.

Another factor that was considered in the nucleation of $\text{Al}_x\text{Ga}_{1-x}\text{P}$ on silicon in these experiments was the total amount of material deposited onto the substrates. Errors in

the total amount of material deposited may arise from the methods used to calculate the growth rate, or from the manner in which the deposition time was measured, or from different MO decomposition reaction rates/efficiencies on the silicon surface versus the $\text{Al}_x\text{Ga}_{1-x}\text{P}$ growing surface. The growth rates of each ternary were calculated using XTEM measurements of $\text{Al}_x\text{Ga}_{1-x}\text{P}$ films with thicknesses greater than $1\mu\text{m}$. Possible errors in these measurements may arise from samples that were slightly tilted away from the $[110]$ zone axis in the TEM, and even more so from the rough $\text{Al}_x\text{Ga}_{1-x}\text{P}$ film surfaces. Thickness measurements from the TEM negatives had a standard deviation on the order of 3% due to surface roughness. The time of deposition was measured using the second hand of a clock. This technique may have been a little crude for obtaining depositions of a constant volume. Errors associated with deposition time variations however are expected to be small. Finally, the decomposition reaction rates of the MO precursors may vary on the silicon wafer as compared to the rate on the $\text{Al}_x\text{Ga}_{1-x}\text{P}$ films due to differences in surface catalytic behavior. Since the XTEM growth rate measurements were taken from thick films, any effects of different decomposition reaction rates at the onset of growth could possibly have been masked.

Variations in material deposited onto the wafers may lead to islands that are at different stages of evolution and growth, which may compromise the proposed model for enhanced mobility of the surface aluminum. The determination of total volume on the surface of the silicon wafers however is fairly difficult. Ideally, one would like to measure the weight of the silicon wafers both before deposition and immediately after, to calculate the total amount of deposited material. However, these measurements were not carried out at the onset of these experiments as a possible total volume discrepancy was not foreseen. Instead, volume measurements have been approximated using AFM data.

To obtain a measurement of the volume of material on the silicon substrates by AFM, the island densities and shapes needed to be known. The island densities were obtained through the island height distribution data and for simplicity, the shapes of the

islands were assumed to be hemispherical. The volume equation of a hemisphere ($\frac{4}{3}\pi r^3$) was used to calculate the volume of every island accounted for in the AFM scans ($25\mu\text{m}^2$) and the island heights were used for the radius values. Calculated volume data is presented in figure 4.21 along with the expected volume for a 50\AA deposit in an area of $25\mu\text{m}^2$.

From this figure, there appears to be a large volume discrepancy from sample to sample as well as from one growth temperature to the next. It was also found that the calculated volume of each sample was below the expected volume for 50\AA thick films in a $5\mu\text{m} \times 5\mu\text{m}$ scan area. These volume discrepancies must be looked at carefully however, due to the nature of the AFM data collection.

The island height distributions were obtained by taking sections of the three-dimensional scan data at selected height threshold values and counting the number of islands that intersected each plane section. Prior to sectioning the data, both maximum and minimum limits of the data were entered. These limits must be values between -32687 and $+32687$, where "zero" is defined as the average value in the height data. Therefore, if data limit values of 0nm (minimum) and 200nm (maximum) are used, the sectional analysis only applies to data within this regime. Since the height value of "zero" is defined as the average value in the height data in a scan, the "zero" cannot be used as a reference point as its actual value will change from scan to scan. Ideally, one would like to set the minimum limit equal to the plane of the substrate surface and the maximum limit equal to that just beyond the tallest island. However, the minimum or substrate value is not known and is very difficult to determine. Therefore, there is error in the volume data especially for those distributions containing a large quantity of smaller islands. In addition, the lateral resolution of the analysis software is not capable of discerning islands very close together and the software algorithms do not distinguish islands when there is intimate contact among them.

This shortcoming in the software analysis does not allow for island counts and therefore volume calculations below a certain height threshold, x , which is located above the substrate surface, y . Thus, a volume of material defined by $(x-y) \times (\text{scan area})$ is not

accounted for in the volume calculations which explains why the volume data points in figure 4.19 are below the expected volume line. The error in the calculated volume decreases as the distribution of the island sizes moves to larger values and the island-to-island spacings increase.

The application of this analysis software for volume calculations has not been recommended as a method for batch processing comparisons [121] due to the lack of a convenient method of defining a reference point. Volume analysis such as the one carried out in these experiments is believed to be beyond the capabilities of this piece of software [121]. Therefore, any volume discrepancies that may exist in the deposited $\text{Al}_x\text{Ga}_{1-x}\text{P}$ on silicon are inconclusive at this time.

4.4 Conclusions

We have investigated for the first time the compositional and temperature dependence of the early stages of growth of $\text{Al}_x\text{Ga}_{1-x}\text{P}$ on Si by MOMBE. For $x=0$ to 0.45 and at a nominal 50Å deposition, $\text{Al}_x\text{Ga}_{1-x}\text{P}$ grows by island formation on the Si surface in the temperature range of 450-550°C. Increases in Al concentration have been shown to influence the nucleation behavior by the formation of a bimodal distribution of island sizes. Increased concentrations of Al in $\text{Al}_x\text{Ga}_{1-x}\text{P}$ were not found to induce planar growth even for $x>0.4$ at any growth temperature studied as was found in the growth of AlGaP/Si by MOCVD. The presence of the bimodal growth has been attributed to the mobility enhancement of the Al adatoms by the gettering of ethyl radicals. This allows the deposit to reach a more equilibrium state of island formation through the ripening of large islands. Volume discrepancy calculations using AFM data have been found to be inconclusive and compromises in the proposed model for bimodal nucleation formation cannot be substantiated at this time.

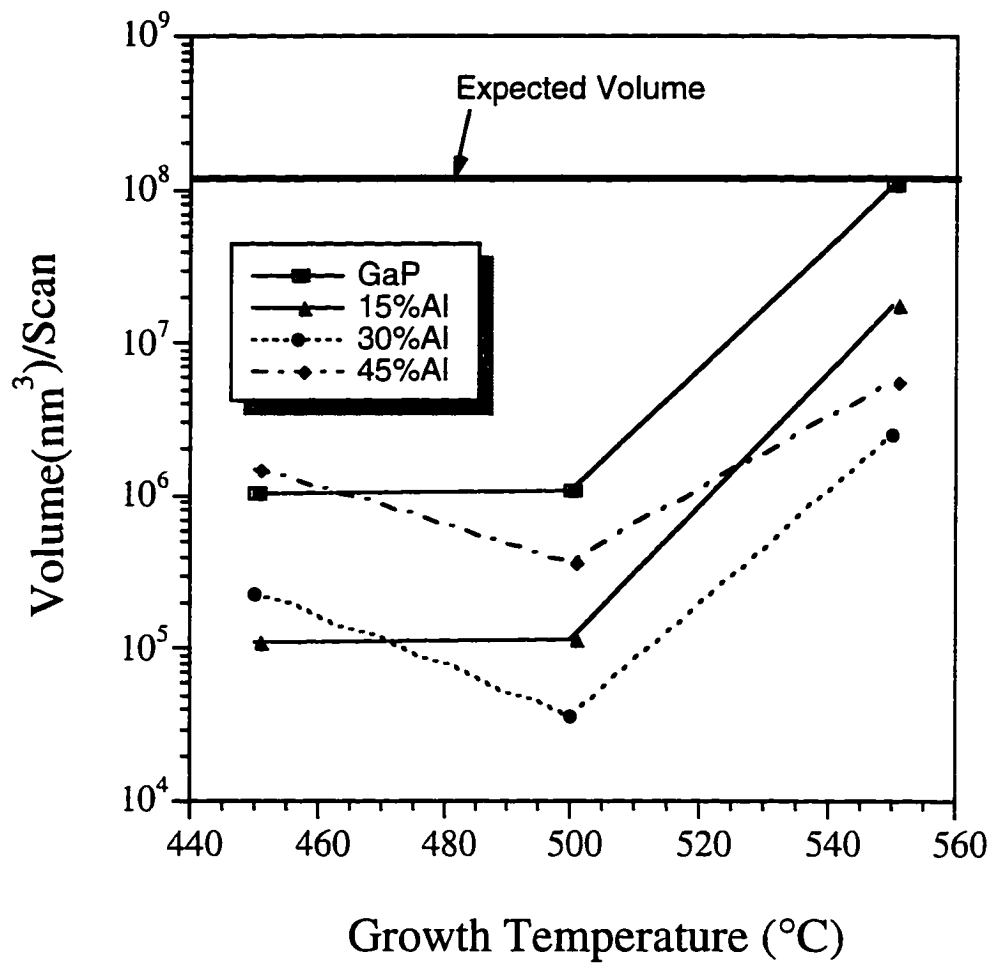


Figure 4.21 Calculated volume of islands deposited onto silicon substrates assuming hemispherical shaped islands.

CHAPTER 5

DEFECT ANALYSIS AND BUFFER LAYER GROWTH

5.1 High Resolution Transmission Electron Microscopy Analysis

Defects may arise in epilayers as a result of a variety of conditions including lattice mismatch, thermal expansion mismatch, growth mode, and surface contamination. Reduction of the strain in an epilayer through the formation of dislocations, twins, and stacking faults can degrade the optical and electronic properties of the deposit and are thus undesirable. Knowledge of the types of defects in the $\text{Al}_x\text{Ga}_{1-x}\text{P}$ films and their densities will help to determine the device potential of this material system. In addition, there is an intimate relationship between the growth mode and the defect formation mechanisms which eventually determine the final film defect structure. It is therefore important to understand the growth characteristics of a material system in order to help resolve potential problems with certain growth defects. HRTEM was used in these studies as it has been shown to be a valuable tool for defect analysis.

All HRTEM images in these experiments were taken under a $[110]$ projection using a selected number of beams within the objective aperture. The micrographs revealed that the dominant defects in the islands and in the thick films were stacking faults and microtwins. In addition, misfit dislocations were observed in the thick films, but they were not common, and vertical defects, believed to be low angle grain boundaries, were found to extend from the heterointerface to the surface of the thick films. The heterointerfaces appeared as bright bands with a width of 1-2nm and contained some areas of possible interfacial disorder. Island faceting and thick film surface facets were also observed.

5.1.1 AlGaP Island Results

Figure 5.1 shows a HRTEM image of GaP islands on silicon grown at 450°C. The height of the larger island is $\approx 90\text{\AA}$ and the width $\approx 200\text{\AA}$. The island already contains planar defects even at this early stage of growth. No misfit dislocations were observed in any islands studied in these experiments, however they cannot be ruled out as the HRTEM viewing area is small compared to the expected misfit spacing. For $\text{Al}_x\text{Ga}_{1-x}\text{P}/\text{Si}$ ($a_{\text{GaP}}=5.4505\text{\AA}$, $a_{\text{AlP}}=5.451\text{\AA}$, $a_{\text{Si}}=5.431\text{\AA}$), the expected spacing for a pure edge misfit dislocation is $\geq 190\text{nm}$. The height of the island is far below the critical film thickness, h_c , necessary for the nucleation of defects by lattice mismatch stresses. Using the expression of People and Bean [122] one obtains a value of $h_c \approx 1500\text{\AA}$. Planar defects were found in approximately 90% of the islands which was fairly constant for each composition and growth temperature studied. The disorder at the interface is seen in the micrograph (marked by an arrow) and is identified by random interfacial contrast. Note that a planar defect appears to originate from this area of disorder.

Faceting of the islands was observed and the most frequent facet angles between the (001) substrate and the $\langle 110 \rangle$ projection were $\approx 55^\circ$, $\approx 15^\circ$ and $\approx 85^\circ$ (assuming that the facets are being observed edge on). These angles correspond to $\{111\}$ facets of epitaxially oriented GaP, first order twins, and second order twins respectively [99]. Island faceting was found to occur for every composition and growth temperature studied. These facets are clearly seen in figure 5.2 in an $\text{Al}_{0.15}\text{Ga}_{0.85}\text{P}$ island grown at 500°C.

At 450°C, low concentrations of Al in the $\text{Al}_x\text{Ga}_{1-x}\text{P}$ did not change the growth mode of the material system but did cause the distribution of island heights to narrow slightly from that observed in GaP. The defects in the aluminum containing compounds were the same as those found in the GaP islands on silicon. Figure 5.3 shows the apparent merging of two $\text{Al}_{0.15}\text{Ga}_{0.85}\text{P}$ islands on the silicon surface resulting in the appearance of a weak band between the islands as marked by an arrow. Twins are present in both islands which again appear to originate at the interface face where there is local disorder.

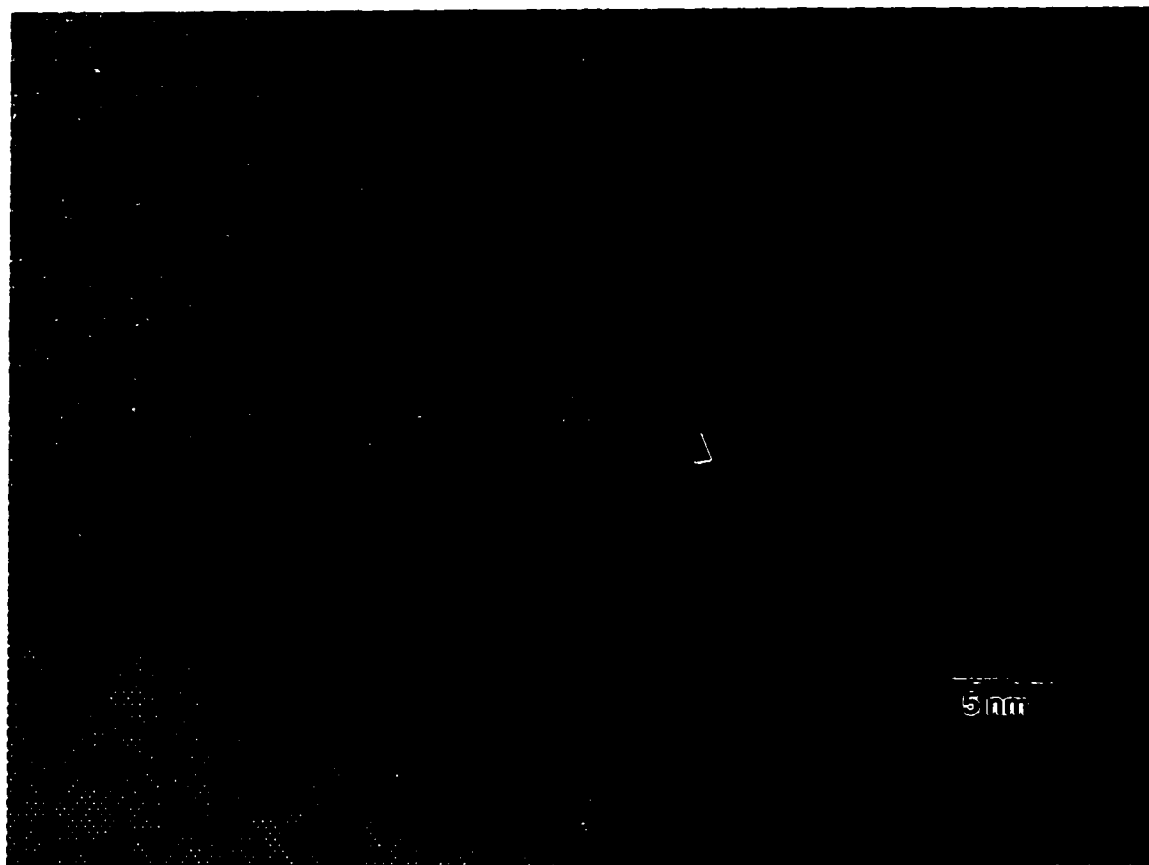


Figure 5.1 HRTEM image of GaP/Si grown at 450°C showing disorder at the interface and planar defects.

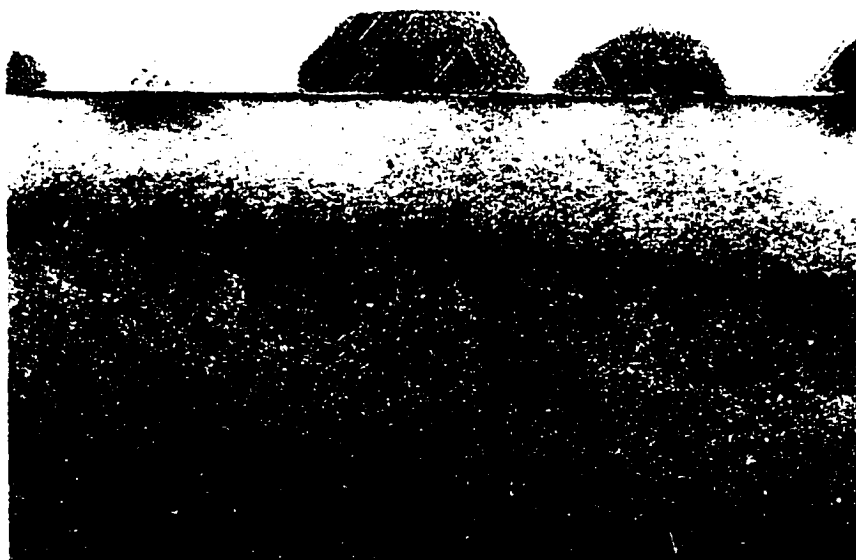


Figure 5.2 HRTEM image of an $\text{Al}_{0.15}\text{Ga}_{0.85}\text{P}$ island grown at 500°C showing $\{111\}$ facets.

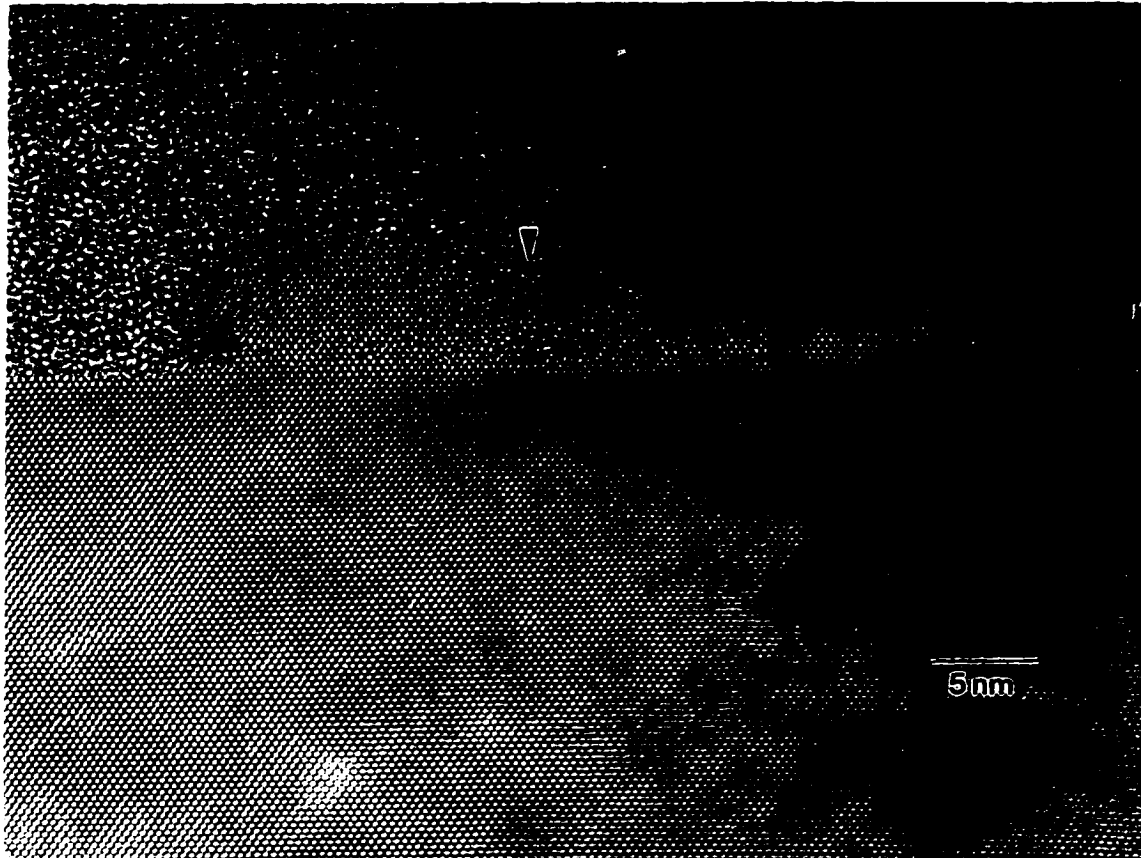


Figure 5.3 HRTEM image of two $\text{Al}_{0.15}\text{Ga}_{0.85}\text{P}$ islands grown at 450° merging into one.

Not all of the islands contained defects as shown in figure 5.4 for $\text{Al}_{0.3}\text{Ga}_{0.7}\text{P}$. An interesting feature of many of the islands was an apparent raised area just under the island and above the substrate. The height of the raised area is about 4-5 monolayers high and extends almost the entire length of the island. The reason that this feature is observable is due to the large contact angle that the rest of the island makes at this point as indicated by the arrow. These raised areas were found for all the compositions and temperatures studied but were only noticeable at very high magnifications.

5.1.2 Thick AlGaP Film Results

The defects observed in the islands were found to exist in the thick films as well. The majority of the planar defects however were found to annihilate close to the heterointerface and the defect densities decreased as the films thickened. The thick films analyzed in this section are calibration runs that had similar or identical compositions to that of the islands.

Figure 5.5 shows a HRTEM image of GaP/Si which illustrates the typical defects found in all of the thick films. The defects consisted of twins, stacking faults, and vertical defects. The vertical defects are indicated in the micrograph by arrows and appear as white bands that extend from the interface to the top of the film. Note that the twin marked T1 terminates at one vertical defect whereas several twins marked T2 pass right through the other vertical defect. Planar defect termination at the vertical defect is shown again at higher magnification in figure 5.6. These vertical defects may arise for two different reasons; they may be low angle grain boundaries that arise from the coalescence of slightly misoriented islands or they may be antiphase domain boundaries (ADBs). Vertical defect identification is discussed in the next section.

The stacking fault densities of some of the AlGaP epilayers were calculated from plan-view TEM and were on the order of $\geq 5 \times 10^8/\text{cm}^2$. Quantification of the stacking fault densities was difficult because many of the defects were annihilated very near the interface.

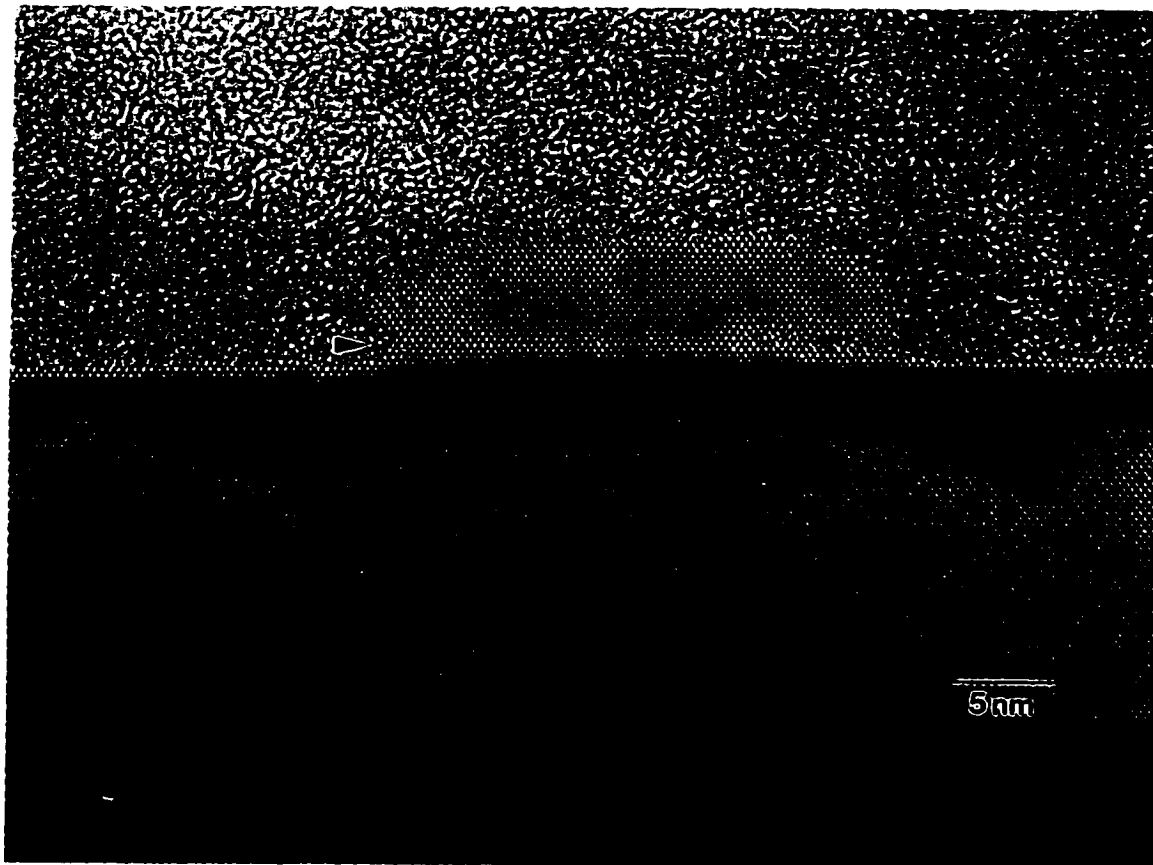


Figure 5.4 HRTEM image of Al_{0.3}Ga_{0.7}P island grown at 450°C showing no defects.

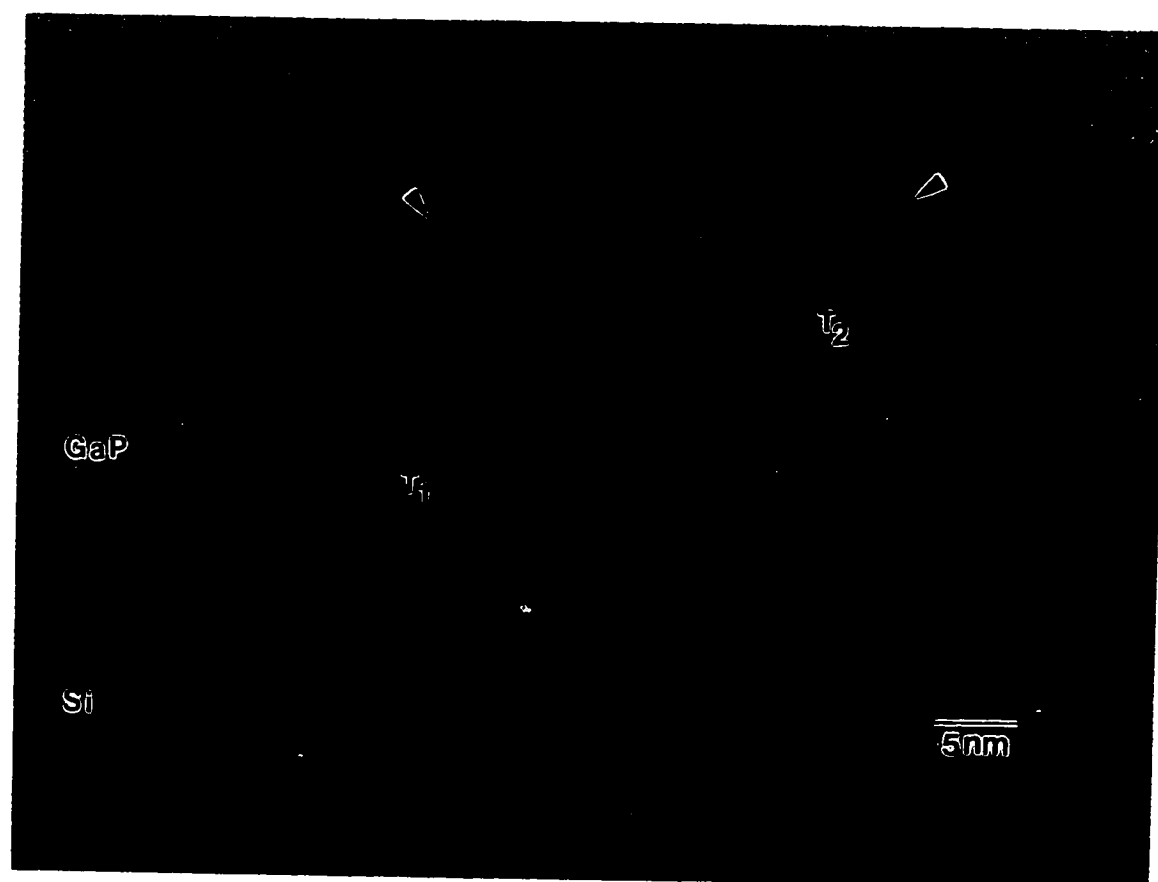


Figure 5.5 HRTEM image of a thick GaP layer on silicon.

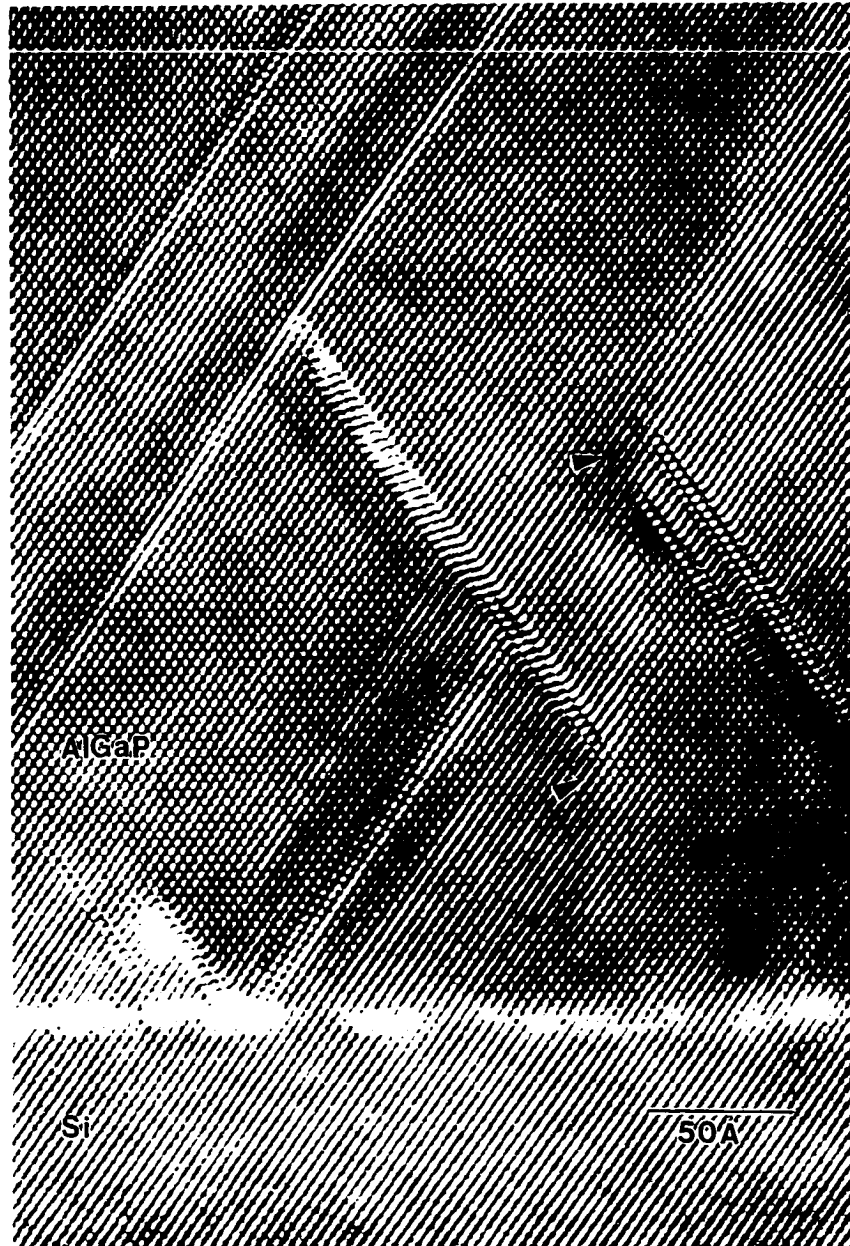


Figure 5.6 HRTEM image of $\text{Al}_{0.1}\text{Ga}_{0.9}\text{P}$ on silicon showing the termination of planar defects at the vertical boundaries.

Only the stacking faults extending through the epilayer were counted leading to errors in the density data. Planar defect densities were also measured from XTEM by counting the number of defects intersecting a line drawn parallel to the interface at a specific height above it. A trend in stacking fault defect density was not found nor could one be found in the thick films with changes in composition. However, higher temperature layers had slightly less planar defects.

Twins were easily viewed in the HRTEM images which were identified by the rotation of the $\{111\}$ lattice planes. Selected area diffraction patterns (SADPs) of the twined areas reveals extra reflections identified as $\{111\}$ twin spots. In the regions of the epilayers where the twin density was low, extra reflections were not found in the SADPs [123]. In addition, no apparent anisotropy could be found in the planar defects.

5.1.3 Discussion of TEM Defect Analysis

The dominant defects in both the islands and the thick films were stacking faults and microtwins. Their occurrence in such numbers was not expected in this material system since the lattice mismatch is small. In addition, planar defects occurred in $\text{Al}_x\text{Ga}_{1-x}\text{P}$ islands with heights of 50-500Å, which is well below the critical thickness of $\approx 1500\text{Å}$ for this material system. Planar defects are commonly attributed to lattice mismatch, low stacking fault energies, and thermal expansion mismatch stresses between the film and substrate. However, many two-dimensional defects observed in these experiments also appeared to originate from areas of disorder at the interface.

Areas of disorder at the interface as observed by HRTEM can be attributed to strain caused by interfacial defects [124], by residual contamination such as an oxide or a carbide [9,34,125] and from HRTEM defocusing conditions [126]. The disordered regions have also been thought to be artifacts of ion milling used in TEM sample preparation and not features inherent to crystal growth however their presence only at the interface is not understood. If such disorder is real, stacking errors resulting from the surface disturbance

are probable and it has been suggested that these areas of disorder are sources of defects [34].

Stacking faults are two-dimensional defects that are formed by the equivalence of removing or inserting an extra plane of atoms between close packed $\{111\}$ planes for intrinsic and extrinsic faults, respectively. In the case of the zinc-blende cubic structure, two sets of atomic planes are extracted or inserted to create these two type of faults which can be represented by the stacking sequences ABCACBCABC for extrinsic and ABCACABC for intrinsic. In $\{100\}$ oriented crystals, the faults lie on inclined $\{111\}$ planes inclined at angles of 54.7° to the surface and lie along orthogonal $\langle 110 \rangle$ directions. Stacking faults can be terminated either by mutual intersection, by partial dislocations, or by interaction with boundaries. They can also react with other stacking faults and dislocations to form a planar defect with a new displacement vector [127] or extend through the entire thickness of the film taking up part of the lattice mismatch.

Because of the presence of planar defects at the early stages of growth, there is some question as to how they are formed. There are several theories on how stacking faults arise which are now discussed. Stacking fault formation has been reported to occur by the nucleation and subsequent separation of Shockley partials from dissociated dislocations as a result of mismatch stresses [128] following:

$$\frac{a}{2}[\bar{1}01] \rightarrow \frac{a}{6}[\bar{2}11] + \frac{a}{6}[\bar{1}\bar{1}2]$$

In the absence of dissociated dislocations, point defect condensation is a possible mechanism of stacking fault nucleation. Stacking faults can be generated at regions of local disorder (surface scratch or contamination) as well as localized nonplanarities on the surface of the wafer [129]. Residues from improper cleaning are reported to give rise to twinning, dislocations, stacking faults and other crystal defects [68].

Stacking faults have also been proposed to nucleate from partial dislocation half-loops that originate at/near the island edges due to stress concentrations [130]. In the growth of ZnSe on GaAs, Hua and coworkers attributed stacking fault formation to surface roughness, growth mode and surface contamination [131].

Recently, Bourret-Courchesne [132] examined the formation mechanisms of stacking faults in the ZnSe/GaAs material system. Their results indicated that a nearly perfect stoichiometric undoped GaAs surface was necessary to prevent the formation of stacking faults and growth conditions leading to an As-stabilized surface were also desired. Excess Zn and/or As on the GaAs surface was found to lead to increased stacking fault densities possibly due to stable Zn-As or Ga-Se compound formations, or from Zn or As dimers.

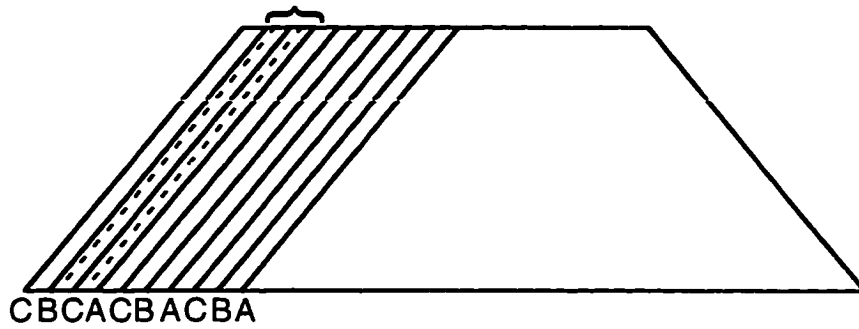
Ernst and Pirouz [99] have reported that the mismatch stresses play only a minor role in the formation of the planar defects and that the dominant formation mechanism is atomic deposition errors on $\{111\}$ island facets in the early stages of growth. To explain the unexpected high density of planar defects in semiconductor films, Ernst and coworkers [99] compared the microstructures of several heteroepitaxial material systems with very different lattice mismatches. TEM was used to examine the defect structure of three compound semiconductors with zinc-blende structures (SiC, GaAs, GaP) on Si(001) and found that the microstructural features were very similar in type and in density showing that the lattice mismatch plays only a minor role. The semiconductors had similar thermal expansion mismatches to silicon but their lattice mismatches covered a wide range: -20% for SiC/Si, 4% for GaAs/Si, and 0.4% for GaP/Si. The comparison of the defect structures in these systems showed the insignificance of the lattice mismatch in the formation of stacking faults and twins. Therefore, Ernst and coworkers set out to explain the formation mechanisms of planar defects which is described here and is believed to be applicable to the $\text{Al}_x\text{Ga}_{1-x}\text{P/Si}$ system as well.

The formation of planar defects in heteroepitaxial films requires sufficient stresses at the interface to nucleate partial dislocations necessary for the generation of the planar defects. Due to the small mismatch of the GaP/Si system however, the coherency stresses at the heterointerface are very low and insufficient to nucleate partial dislocations [133]. In addition, GaP shows little plasticity at temperatures below 800°C and since dislocations have very low mobilities at temperatures $\leq 500^\circ\text{C}$, thermal stresses can not be blamed for the high density of planar defects [133]. Therefore, a model based on stacking errors on $\{111\}$ facets was developed to explain the formation mechanisms of planar defects. The model is illustrated in figure 5.7 in a $[110]$ cross-section of truncated pyramid shaped islands.

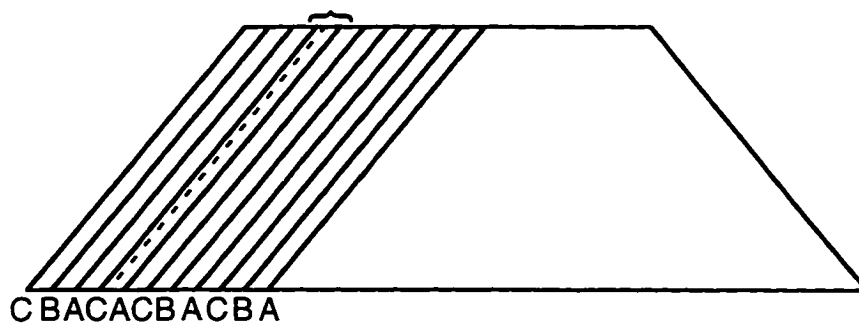
The formation mechanism of stacking faults and twin boundaries proposed in this model is based on the possibility of deposition errors on the $\{111\}$ facets of islands. Thus, the energy difference between the correct and incorrect deposition sites on the facets should be reasonably small when compared with the average thermal energy of the atoms. Using the assumption that the energy associated with a misdeposited atom double layer is 50% of the stacking fault energy ($\gamma = 41 \text{ mJ/m}^2$ for GaP), the deposition fault energy was calculated to be $\approx 0.2kT$ per atom. Therefore, misdeposited atoms on $\{111\}$ facets would be very common. The same arguments also hold true for GaAs/Si and SiC/Si.

The vertical defects observed in both the AlGaP and GaP thick films were believed to be either antiphase domain boundaries or low angle grain boundaries. In the growth of polar III-V materials on nonpolar group IV materials, it is possible, due to single surface step heights, that the group III and group V sublattice are exchanged in neighboring islands. Upon coalescence of the islands the group III sublattice of one island matches up with the group V sublattice of the next island forming a compensated defect. An illustration of antiphase domain boundaries is shown in figure 5.8. ADBs can be minimized through the use of tilted substrates which form double height steps upon high temperature treatment [134]. Utilization of double step surfaces and the introduction of the group V precursor

Extrinsic Stacking Fault



Intrinsic Stacking Fault



Twin

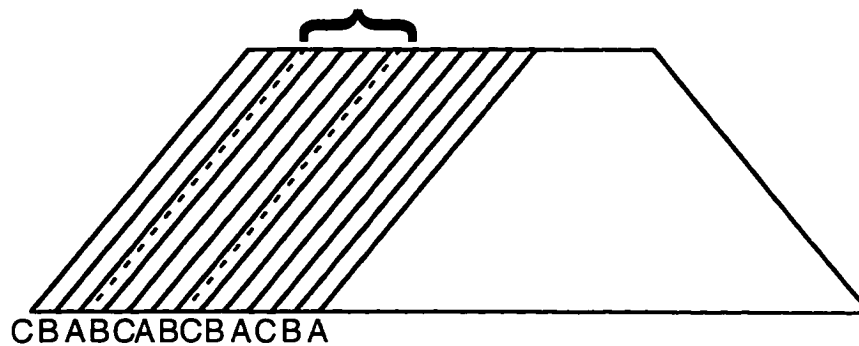


Figure 5.7 Formation of planar defects by misdeposited atomic islands on $\{111\}$ nucleus facets for a) an extrinsic stacking fault, b) an intrinsic, and c) a twin.

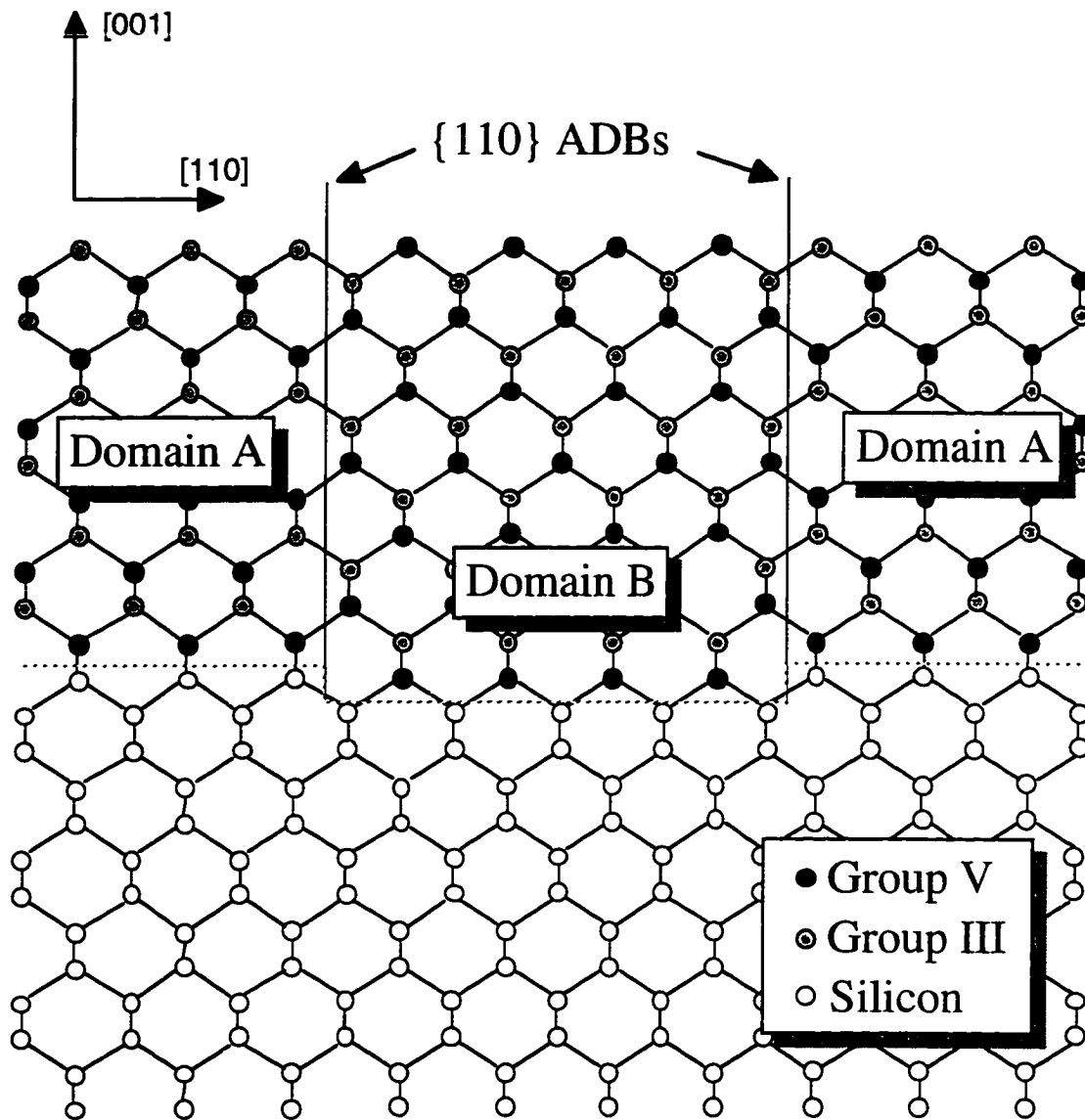


Figure 5.8 Schematic cross section of ADBs which nucleate at single-atom steps

first, insures that the growth will begin with the group V sublattice and growth of only one domain. Confirmation of ADBs can be made through the use of convergent beam electron diffraction (CBED) patterns. According to Taftø [135], contrast within strong 200-type reflections arising from weak odd indexed reflections will depend on the 200 reflection, i.e., one can distinguish between a 200 or a $\bar{2}00$ reflection. Thus, the contrast reversion means that a 200 reflection exists on one side of the ADB and a $\bar{2}00$ reflection on the other side. In addition to CBED, antiphase domains can be evaluated by using dark field TEM [134], observation of etch pit direction [134], and anisotropic etching [136]. Petroff [137] calculated the energy of the antiphase domain boundaries for (100), (110), (111) and (211) planes and found that the (211) and (110) ADBs are more likely to form than for the (111) or (100) planes. Dark field TEM analysis was used to examine the vertical defects in the $\text{Al}_x\text{Ga}_{1-x}\text{P}/\text{Si}$ system, however no verification of ADBs was found.

The vertical defects may also be low angle grain boundaries which could result from the growth mode of the film. Three-dimensional growth may lead to the formation of islands that are slightly offset from one another. As these islands grow, a grain boundary forms between two misoriented islands which extends all the way to the surface of the film. To prove the existence of such a boundary, a diffraction pattern of the boundary area can be taken in TEM using a selected area aperture and a shift in the diffracted spot pattern should indicate the angle of misorientation. However, after diffraction pattern analysis of several boundary areas, misorientation of the grains could not be found possibly due to the extremely low angle between the grains ($<1^\circ$). Another method of verifying a grain boundary is to examine the HRTEM lattice images of the boundaries and look for inconsistencies in the number of lattice planes associated with dislocations. Again, a verification of low angle boundaries was not reached as dislocations were not observed at the boundaries. This can be attributed to a very small angle boundary as well making it difficult to capture the dislocation within the viewing area of the HRTEM micrograph.

The slight contrast difference arising at the vertical boundaries is an interesting observation. Its origin may be related to the contrast seen at heterointerfaces which come from strain variations as well as from surface contamination resulting from substrate cleaning and the impurities in metal-organic precursors. As mentioned in Chapter 4, surface defects are sites of preferred nucleation due to the high energy associated with the defect and the boundaries between the coalesced islands could also represent preferred sites for the surface species to deposit, in particular the ethyl groups. Although it can not be verified, the vertical defect contrast may be due to the collection of surface impurities during growth as the coalescence boundaries act as impurity sinks.

For island growth, dislocations can be introduced directly either at the edges of islands [130] or at the trough between two islands where lattice distortion exists [138]. Island coalescence boundaries are reported to be favorable sites for defect incorporation [130] and proposals for dislocation generation through island merging have been made [4,139]. It should be understood that XTEM is an "after the effect" technique, so that there is always an ambiguity as to whether the defect was actually formed during the coalescence event or not.

A comparison of the planar defects in GaAs using AlGaAs nucleation layers showed that the average size and density of microtwins are reduced when the AlGaAs islands are small and have a high density [123]. The quality of the final III-V layer on silicon reflects that of the initial buffer layer which can be understood by keeping in mind that the size and density of islands and the manner of their subsequent coalescence influence the surface morphology and the defect formation. This result has not been found however, in the growth of GaP/Al_xGa_{1-x}P/Si by MOMBE, as the defect density and structures of the thick GaP layers appear to be unaffected by the species or the smoothness of the buffer layers.

Two types of misfit dislocations induced in III/V on silicon heteroepitaxy have been previously reported [140]. Type I dislocations have Burgers vectors in the interface plane,

while type II dislocations have Burgers vectors which are inclined to the interface. Type II misfit dislocations are only half as effective for the accommodation of the lattice mismatch as pure-edge type I misfit dislocations because of the inclination of their Burgers vectors from the interface by 45° .

Pure-edge misfit dislocations can be identified by the presence of both (111) and $(1\bar{1}\bar{1})$ extra lattice fringes and an extra (111) for the type II misfits in (001) oriented films by HRTEM. The Burgers vector of the two types of misfits can be determined uniquely with the appearance of the extra lattice planes through a Burgers circuit analysis of the HRTEM image as schematically shown in figure 5.9. Burgers vectors of edge dislocations are $1/2[110]$ or $1/2[1\bar{1}0]$, which are parallel to the interface, while the Burgers vectors of type II dislocations are $1/2[101]$, $1/2[10\bar{1}]$, $1/2[011]$ or $1/2[0\bar{1}1]$, which are inclined from the interface by 45° .

Misfit dislocations however are difficult to find in HRTEM images for material systems with small lattice mismatch. For $\text{Al}_x\text{Ga}_{1-x}\text{P}$ where the lattice mismatch is about 0.4% over the entire aluminum composition range, the expected spacings for type I and type II misfit dislocations are 192nm and 96nm respectively. This is compared to values of 18nm (type I) and 9nm (type II) for GaAs on silicon which has a 4% lattice mismatch. In addition, strain relief through formation of planar defects reduces the driving force for misfit dislocation formation and increases the misfit spacings. This irregular spacing makes it difficult to determine the misfit dislocation content of the interface accurately.

Energetically, pure-edge misfit dislocations are preferable to the type II misfit because the burgers vector of the type I misfits are parallel to the interface thus relieving more of the lattice mismatch. However, because of crystallographic constraints, they are more difficult to form (glide on the close-packed $\{111\}$ planes is easier than on the $\{100\}$ planes). Because of these crystallographic constraints, it has commonly been assumed that type I misfits must be formed by some appropriate interaction of type II dislocations. The nucleation mechanism of a pure edge misfit dislocation is commonly suggested to be a

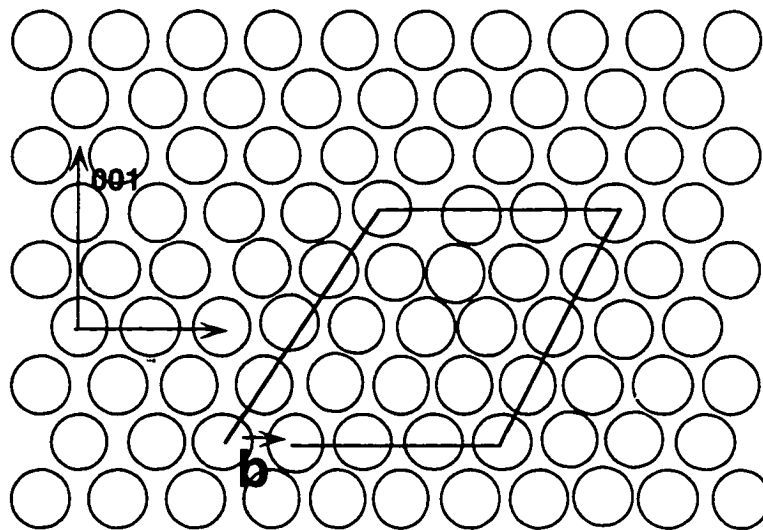
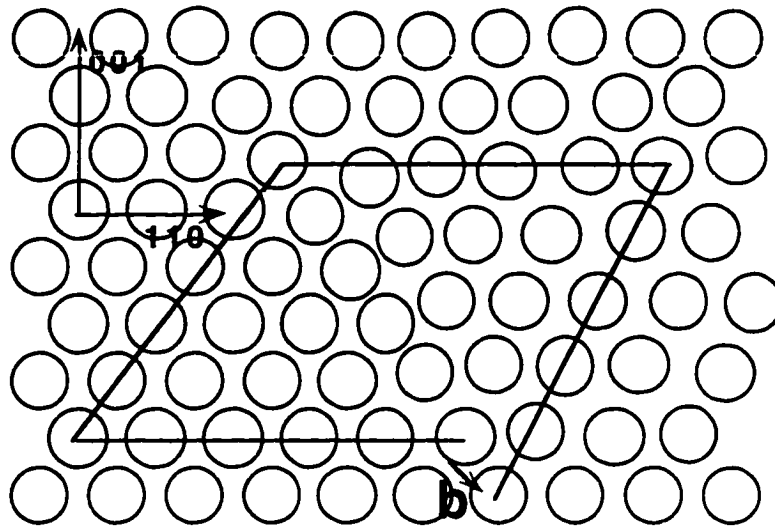


Figure 5.9 Schematic Burgers circuits for a) type II and b) type I misfit dislocations.

result of the combination of two type II misfits moving on opposed $\{111\}$ glide planes [141,142]. In terms of Burgers vectors a typical such reaction may be written as follows:

$$\frac{1}{2}[101] + \frac{1}{2}[\bar{1}10] \rightarrow \frac{1}{2}[011]$$

5.2 Buffer Layer and GaP Thick Film Optimization

For the growth of GaP on silicon substrates, optimal $\text{Al}_x\text{Ga}_{1-x}\text{P}$ buffer layer growth conditions needed to be identified. Several growth parameters may be varied to modify the film quality of buffer layers including ternary composition, film thickness, group V flow, and growth temperature. The effect that each one of these parameters has on the buffer layer quality has also been shown to carry over to the properties of subsequently grown thick films [143]. In general, the requirements for a buffer layer are that it deposits on the substrate surface such that it forms a continuous layer early on to establish a smooth starting surface for the growth of the subsequent III-V material.

Tu et al. [144] found that the best buffer layers for GaP/Si growth are those that have smooth surfaces and are formed by a large density of small islands which coalesce at the early stages of growth. In his experiments, prelayers of group III atoms were utilized in the growth of high island density buffer layers. Prelayers are simply a monolayer coverage of an adsorbate on the substrate surface. Prelayers have been explored by several researchers in order to change the overlayer bonding character and film quality [25,38,145]. Buffer layer island distributions were found to narrow through the use of Ga+Al prelayers on the silicon substrate as compared to the use of a P prelayer.

In addition, Tu et al. [144] grew $2.5\mu\text{m}$ thick layers of GaP on GaP buffer layers using the two-step growth technique and different prelayers. X-ray diffraction was used to determine the FWHM of the thick layers and AFM was used to measure the surface roughness. The results, as shown in table 5.1, indicate that the best quality GaP films were obtained by using a group III prelayer which favored the coalescence of a high

density of small GaP islands at the early stages of growth. Yoon et al. [102] had similar success with high densities of small islands in the growth of GaAs on silicon. They found the FWHMs of the 3 μ m GaAs films decreased as the GaAs islands sizes in the buffer layer decreased and their densities increased.

Table 5.1 X-ray FWHM and AFM surface roughness of 2.5 μ m thick GaP on silicon grown with different prelayers.

Prelayer Species	FWHM (arcsec)	Surface RMS (nm)
Ga	221	9.87
Al+Ga	437	29.42
AsH ₃	394	31.19
PH ₃	628	- -
Al	469	- -

The above results were used in determining the island morphology necessary in the growth of Al_xGa_{1-x}P buffer layers by MOMBE. The growth conditions and aluminum composition best suited for the buffer layer were selected by examination of the island height distributions for each sample grown in MOMBE. From these distributions, the Al_{0.15}Ga_{0.85}P sample grown at 450°C was identified as the best candidate for early coalescence due to its narrow, single-mode, high-density distribution. Similar island profiles of AlGaAs were used in the growth of the GaAs/AlGaAs/Si system [123] where higher densities of AlGaAs islands were found to lead to better GaAs film morphology through the formation of smoother nucleation layers.

The next step in the optimization process was the selection of the thickness of the $\text{Al}_x\text{Ga}_{1-x}\text{P}$ buffer layers. Bi et al. [36] used x-ray diffraction to determine the thickness of GaP buffer layers that lead to the best FWHM of subsequently grown GaP layers. They found that a buffer layer with a thickness on the order of 200Å grown at 400°C provided the lowest FWHM for the thick GaP layers. Other researchers have also used thin buffer layers for heteroepitaxial growth that have ranged from 50-200Å [143,146,147]. To insure complete $\text{Al}_x\text{Ga}_{1-x}\text{P}$ island surface coverage, we examined buffer layer thicknesses of 300, 500 and 700Å grown at 450°C. Determination of the optimum buffer layer thickness was made by AFM measurements of surface roughness and examination of the surface feature distributions. Complete coalescence of the islands was achieved at 300Å as identified by the island height distributions and TEM. The surface roughnesses (RMS) of the three buffer layers were 3.47nm, 3.3nm and 4.03nm for the 300, 500 and 700Å layers respectively. Since there was not a significant change in the roughness values, the 500Å buffer layer was chosen to ensure complete surface coverage of the silicon and to provide a relatively smooth surface for growth.

The optimum growth conditions for GaP thick layers in MOMBE were determined by the deposition of homoepitaxial GaP layers. The surface morphology of the GaP films as observed using AFM and SEM, and the microstructure was analyzed by TEM. The GaP wafers were cleaned ex situ using a 4HCl: 4HNO₃: 5H₂O chemical solution which left the wafer surface oxidized [148]. Desorption of the oxide was carried out in the growth chamber at a temperature of 650°C and 2µm thick GaP layers were grown between 525°-600°C. The microstructures of the homoepitaxial layers were indistinguishable as no defects were observed in TEM. Smooth GaP homoepitaxial layers (RMS=2.3nm) were achieved by using a lower growth temperature of 525°C and precursor flows of 2sccm PH₃ and 0.4 sccm TEG. These growth conditions were used for the growth of GaP on the $\text{Al}_{0.15}\text{Ga}_{0.85}\text{P}$ buffer layers in the thick film studies.

In summary, the optimum buffer layers were composed of $\text{Al}_{0.15}\text{Ga}_{0.85}\text{P}$ grown at 450°C to a thickness of 500\AA . The wafers were then heated to 525°C under a P_2 beam for the growth of approximately $2\mu\text{m}$ of GaP. The quality of the thick films is discussed in the following section.

5.3 Analysis of GaP/AlGaP Structures

The first attempt at growing a thick GaP layer on an optimized $\text{Al}_{0.15}\text{Ga}_{0.85}\text{P}$ buffer layer resulted in a very hazy sample as viewed by the eye. AFM surface roughness analysis of the film showed that the RMS was on the order of 77nm . The rough surface morphology could also be seen in TEM as shown in figure 5.10. The growth temperature of the buffer layer was 450°C and that of the subsequent GaP layer was 675°C , following the successful work of Bi et al. [36] in the growth of GaP/Si by CBE at 750°C . However, these growth temperatures are believed to be too high for the growth of GaP in MOMBE using metal-organic precursors and a phosphine flow of 2sccm . The growth temperature was therefore lowered to 525°C (optimized conditions for GaP/GaP). Figure 5.11 shows the GaP/ $\text{Al}_{0.15}\text{Ga}_{0.85}\text{P}$ /Si structure. Note that all of the aforementioned defects are present in the GaP layers grown on the optimized $\text{Al}_{0.15}\text{Ga}_{0.85}\text{P}$ buffer layers. In fact, the defect density of these layers does not appear to be improved over the films grown without buffer layers. A GaP/GaP(buffer)/Si structure was also grown for comparison and the microstructure was found to be similar to the $\text{Al}_{0.15}\text{Ga}_{0.85}\text{P}$ buffer layer structures. The surface roughness of the GaP/ $\text{Al}_x\text{Ga}_{1-x}\text{P}$ /Si and GaP/GaP/Si structures grown at 525°C were 19.9nm and 20.7nm respectively, showing that the improvement in the use of $\text{Al}_{0.15}\text{Ga}_{0.85}\text{P}$ buffer layers is negligible in MOMBE.

5.4 Secondary Ion Mass Spectrometry Analysis

Uncontrolled impurity incorporation into epitaxial films can be detrimental to the final film properties. It is therefore beneficial to know the amount of contamination in a



Figure 5.10 TEM image of GaP/Al_{0.15}Ga_{0.85}P/Si grown at 675°C.



Figure 5.11 TEM image of GaP/Al_{0.15}Ga_{0.85}P/Si grown at 525°C.

grown film prior to the fabrication of a device so that improvements in source chemistry or compensation of impurities can be made if they are needed. SIMS was used to obtain both relative and quantitative measures of the amount of oxygen and carbon in the $\text{Al}_x\text{Ga}_{1-x}\text{P}$ films and at the $\text{Al}_x\text{Ga}_{1-x}\text{P}/\text{Si}$ heterointerfaces. These impurities were tracked as the growth temperature and composition, x , of the $\text{Al}_x\text{Ga}_{1-x}\text{P}$ films were changed.

The amount of an impurity in a film grown by MOMBE is influenced by the mechanisms of growth. As mentioned in Chapter 2, in MOMBE growth there are no gas phase interactions and as a result impurities in the source materials arrive unimpeded at the wafer surface where they can incorporate readily at the growth front. One of the primary concerns for impurity incorporation in MOMBE is the efficiency of decomposition of metal-organic precursors on the wafer surface. Decomposition efficiency of the precursor molecule plays a large role in the impurity incorporation in epitaxial films. The efficiency is governed by several factors including growth temperature, source chemistry, sticking coefficient and precursor catalytic requirements.

Growth temperature has been shown to have an strong effect on the efficiency of precursor decomposition. There exists a temperature below which there is not enough energy for the decomposition of the parent molecule to occur such that the efficiency falls to zero. TEG pyrolysis begins at approximately 380°C and significant desorption of Ga species, primarily diethylgallium (DEG), occurs at temperatures $>550^\circ\text{C}$.

The implications of decomposition efficiency are most important at low growth temperatures where there is incomplete decomposition of the precursor molecules. Low growth temperatures provide the means for incorporation of partially decomposed molecular species which leads to contamination of the epilayers. Therefore, the growth temperatures used in MOMBE should be selected with the precursor decomposition characteristics in mind. In addition, impurity contamination can be minimized through the use of more weakly bonded precursors and/or sources that do not contain any of the elements causing the impurity problem.

TEG was used as the gallium source in the growth of the $\text{Al}_x\text{Ga}_{1-x}\text{P}$ films because of the lower carbon levels found in the resulting films and the lower growth temperatures that can be used as compared to TMG. Carbon has been observed to be a predominantly p-type contaminant in GaAs and GaP which incorporates into the group V lattice site and is strongly affected by both the growth temperature [54] and the V/III ratio [59]. Abernathy et al. [59] postulated that the reduction in carbon incorporation with increased V/III ratios in the growth of GaAs using TEG was due to the increase of $(\text{C}_2\text{H}_5)_x\text{As}$ formation and subsequent removal from the surface with increasing AsH_3 flow rate.

Deposition of GaP/GaP was studied in order to optimize the MOMBE growth parameters of this material system prior to the growth of $\text{GaP}/\text{Al}_x\text{Ga}_{1-x}\text{P}/\text{Si}$ structures. Various growth temperatures were used to achieve a combination of the best GaP surface morphologies and the lowest impurity concentrations. Figure 5.12 shows the oxygen and carbon dependence as the growth temperature is varied. As can be seen, the impurity incorporation was high for low growth temperatures which then decreased as the growth temperature was raised. The majority of the carbon impurity is a result of the decomposition of the TEG. Lower carbon levels can be achieved through proper selection of the V/III ratio.

The carbon and oxygen background in Al containing films however is higher than those films without aluminum. The large impurity background in $\text{Al}_x\text{Ga}_{1-x}\text{P}$ is due primarily to the strong affinity of aluminum for oxygen and carbon. Replacing the traditional alkyl precursor with a non-carbon bonded source such as DMEAA helps reduce the impurity incorporation. However, because the Al-O and Al-C bonds are strong, the impurities are found to increase as the aluminum composition of the ternary is increased as shown in figure 5.13. The carbon and oxygen primarily come from the TEG. From figure 5.14, it can be seen that the oxygen concentration at the AlGaP/Si interface follows the same trend as the bulk films. Therefore, the quality of the AlGaP buffer layer may be diminished as a result of the high oxygen and carbon background.

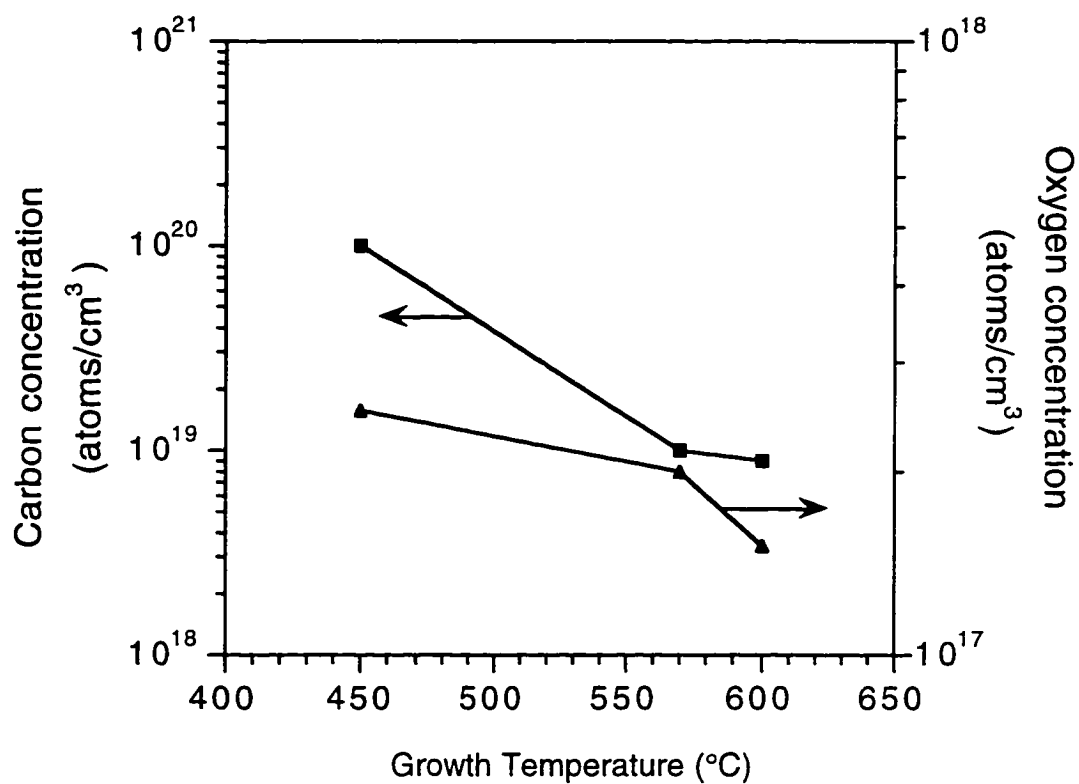


Figure 5.12 Carbon and oxygen concentration in GaP films grown by MOMBE using TEG and PH₃.

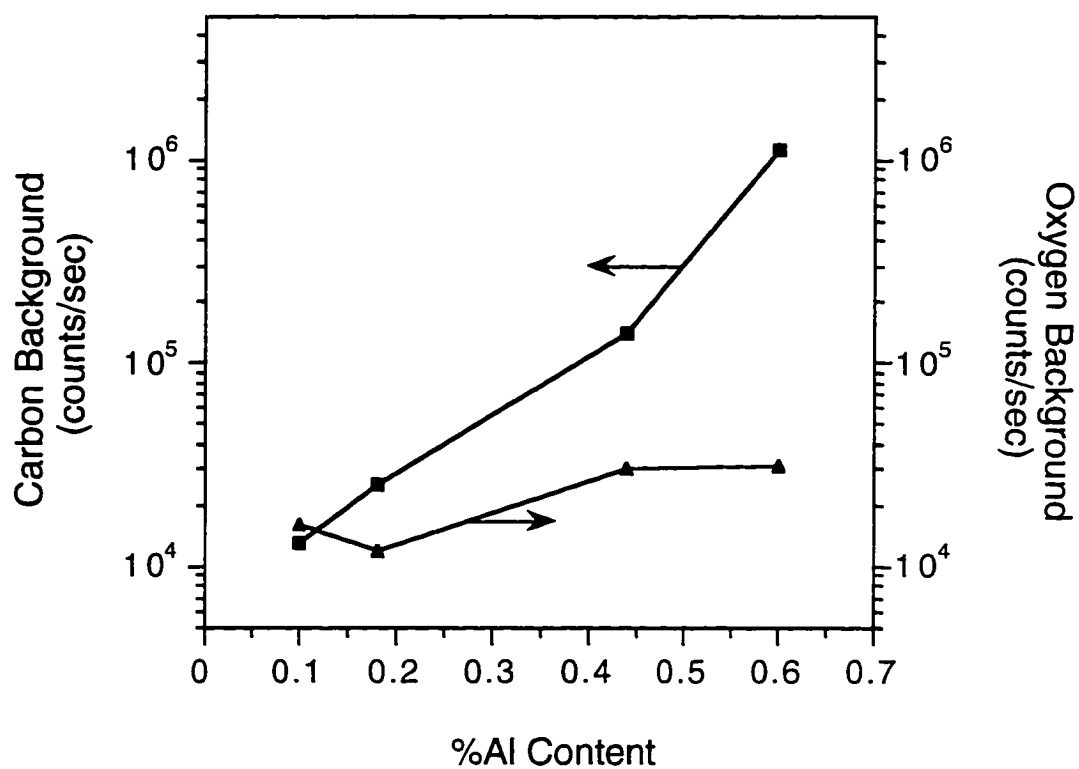


Figure 5.13 Relative carbon and oxygen concentrations in $\text{Al}_x\text{Ga}_{1-x}\text{P}$ grown at 550°C .

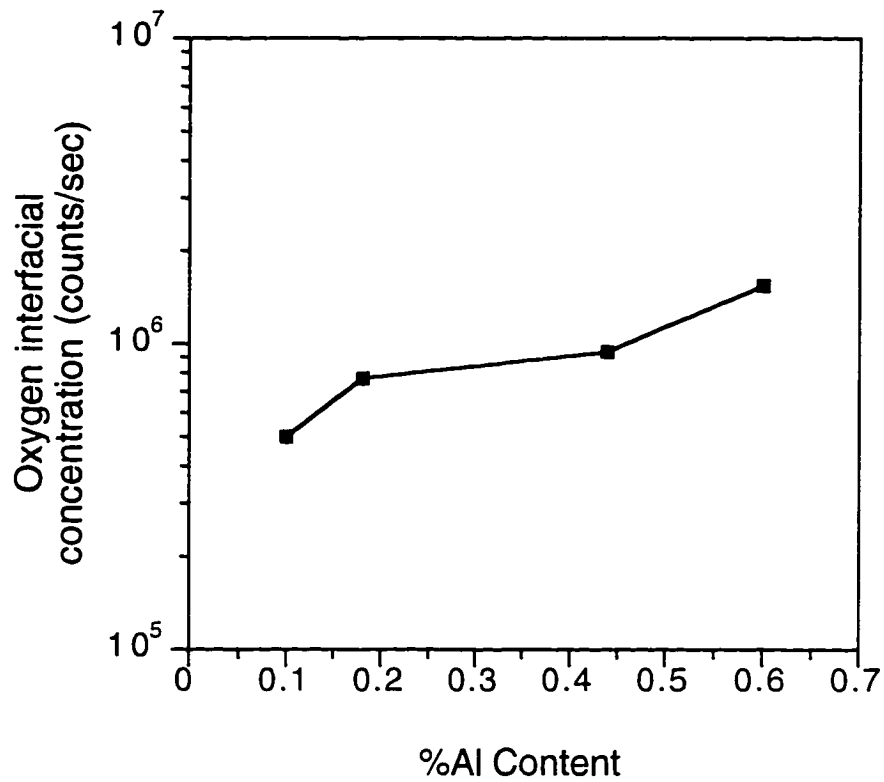


Figure 5.14 Relative interfacial oxygen concentration at the $\text{Al}_x\text{Ga}_{1-x}\text{P}/\text{Si}$ heterointerface at 550°C .

CHAPTER 6

CONCLUSIONS AND RECOMMENDATIONS FOR FUTURE WORK

6.1 Conclusions

$\text{Al}_x\text{Ga}_{1-x}\text{P}$ buffer layers were grown on silicon substrates for the subsequent growth of GaP. Optimization of the buffer layer conditions were identified through a detailed examination of the early stages growth. Nucleation and growth of $\text{Al}_x\text{Ga}_{1-x}\text{P}$ on silicon grown by MOMBE was studied extensively using TEM, to observe island morphologies and defects, and AFM, to determine island densities and height distributions. The compositions examined ranged from $x=0$ to 0.45 and the growth temperatures were varied from 450-550°C.

Epitaxial silicon substrate preparation consisted of ex situ dip etching in diluted HF:DI solutions. Etching time and concentration were found to affect the surface roughness of the wafers and the surface oxygen concentration. Increased etch times and HF concentrations caused increased surface roughnesses and higher oxygen contamination at GaP/Si heterointerfaces.

The nucleation of $\text{Al}_x\text{Ga}_{1-x}\text{P}$ on silicon was found to occur through the formation of discrete three-dimensional faceted islands. Island height distributions changed with ternary composition and growth temperature, and the emergence of a bimodal distribution of $\text{Al}_x\text{Ga}_{1-x}\text{P}$ ($x>0$) islands was found to occur. Bimodal island distributions were explained by the enhancement of the mobility of Al adatoms by the gettering of ethyl radicals on the substrate surface resulting from the decomposition of triethylgallium (TEG).

TEM examination of the $\text{Al}_x\text{Ga}_{1-x}\text{P}$ structures revealed that the dominant defects in the islands and in the thick films were stacking faults and microtwins. Misfit dislocations

were observed but were not common, and vertical defects, believed to be low angle grain boundaries, were found to extend from the heterointerface to the surface of the thick films. There was good registry across the heterointerfaces and some areas of possible interfacial disorder.

Optimized buffer layer conditions were determined by the formation of continuous $\text{Al}_x\text{Ga}_{1-x}\text{P}$ films through the early coalescence of high densities of small islands. $\text{Al}_{0.15}\text{Ga}_{0.85}\text{P}$ buffer layers 500Å thick, grown at 450°C, were used for the growth of GaP/Si. However, $\text{Al}_x\text{Ga}_{1-x}\text{P}$ buffer layers only showed minimal improvement over GaP buffer layers.

6.2 Recommendations for Future Work

a) Use of a "Surfactant" Layer: Fabrication of many state of the art electronic devices, both in elemental and compound semiconductors, requires heteroepitaxial growth of one material onto another. Efforts to grow such structures are frequently complicated by islanding of the growing material due to a mismatch in surface energies, bulk lattice constants, or both. In general, fabrication of electronic materials requires layer-by-layer growth for high quality devices. A reduction in the growth temperature is often used to suppress diffusion of surface adatoms and thus prohibit or suppress island formation. However, low temperatures do not always produce the best quality material. An alternative is to introduce an adsorbate for impurity-mediated suppression of islanding [149]. For example, in the growth of Ge on silicon substrates, the use of group V materials (As, and Sb) has been explored.

The adsorbate lowers the surface free energy, floats at the surface during growth, and thus reduces the Ge diffusion length in the deposition of Ge on silicon. As and Sb termination of the sample is energetically favorable [150], and the growing species will therefore be rapidly incorporated in a subsurface site. The driving force for the local site exchange is lower free energy as the Si(100)/Ge/As configuration is lower than

Si(100)/As/Ge by 1.7eV per (2x1) unit cell [151]. The presence of a group V impurity on the growth front suppresses diffusion of the Ge surface adatoms prohibiting island formation on the silicon. At this time however, an adsorbate for the impurity-mediated suppression of islands has not been identified for the growth of $\text{Al}_x\text{Ga}_{1-x}\text{P}$ on silicon.

b) Alternative Group III Sources: Elemental and other group III precursors should be explored in MOMBE in the study of AlGaP nucleation on silicon to test the proposed model of ethyl radical gettering. The use of elemental gallium will eliminate all ethyl radicals from the substrate surface which should result in a single mode island height distribution.

c) Prelayer Exposure: This technique is slightly different than a surfactant as the prelayer resides at the heterointerface during growth. The introduction of a prelayer prior to growth can affect the nucleation characteristics of the deposit. For future growth of $\text{Al}_x\text{Ga}_{1-x}\text{P}$ on silicon it is recommended that the deposition be preceded by the introduction of a group III species to the silicon wafer if possible, to accelerate the coalescence process of the islands.

d) Silicon Epi: Growth of III-Vs on a silicon epilayers that have been grown in the same growth chamber as the III-Vs will help minimize impurities on the silicon surface and reduce the possibility of planar defect nucleation from areas of surface contamination (areas of disorder). Homoepitaxial growth is commonly carried out in the growth of GaAs based materials on GaAs substrates. Typically, a thin epitaxial GaAs buffer layer ($\approx 0.3\mu\text{m}$) is grown prior to the deposition of subsequent films. The buffer layer is grown to provide a high quality smooth surface and its doping content can also be regulated.

e) Quantum Dot Studies: From the experiments of this dissertation, it has been shown that the $\text{Al}_x\text{Ga}_{1-x}\text{P}$ island distributions can effectively be changed with growth conditions and composition. An application that could utilize the properties of islands on a wafer would of course be of interest. One such novel application for materials that grow in this fashion is found in the emerging field of quantum dots. Material systems that show a

self-assembly process in the formation of islands are being considered for the fabrication of nanometer-scale dots. If such processes are successful, it may be possible to form ensembles of nearly identical quantum systems with little inhomogeneous broadening. These structures have potential applications in basic studies of quantum confinement as well as electronic and optical devices. The advantages of this dot fabrication technique are that no nanolithography, etching or implantation induced processes are necessary. If the sizes of active regions are drastically reduced, the number of dislocations in the active regions can also be potentially reduced in dots grown on a highly mismatched substrate. The inherent problem of growing quantum dots is however, the nonuniformity in size and uncontrollability of the position of these structures for possible device applications. Material systems being explored for quantum dot applications include InAs and InGaAs/GaAs [21,152], as well as InSb, GaSb and AlSb/GaAs [104]. Preferential nucleation sites have been found to play an important role in the distribution and uniformity of dots. Work in the InAs/GaAs system revealed preferential nucleation of the dots at step edges in misoriented substrates[21,103]. Nanometer-scale dots have so far been grown only by MOCVD and MBE.

f) Wafer Bonding Alternative: As seen in Chapter 5, the quality of the GaP films grown on silicon is relatively poor. To date the defect density of III-Vs on silicon has not reached a routinely acceptable level for many applications including lasers and LEDs. For best device performances, defect densities on the order of $\leq 8 \times 10^4/\text{cm}^2$ are desired for lasers, $\leq 4 \times 10^5/\text{cm}^2$ for LEDs, and $\leq 10^6/\text{cm}^2$ for solar cells [153] (although the nitride materials show otherwise). Therefore, for optoelectronic integrated circuits (OEICs) and other devices to become a reality, it may be necessary to find an alternative fabrication technique to heteroepitaxy. One such technique for integration of III-Vs on silicon is through the use of wafer bonding by atomic rearrangement (BAR) [154-156]. Bonding wafers using the BAR process eliminates many of the problems associated with defect

formation in heteroepitaxy and results in relatively good mechanical strength and thermal stability of the films due to covalent bonding.

High performance edge-emitting and surface-emitting lasers on GaAs and Si substrates and high efficiency resonant cavity photodectors have been reported using this wafer bonding technique [155]. During the bonding process, heat and pressure are applied to the adjoined wafers in the presence of hydrogen flow resulting a bonded interface between in the III-V and silicon. Lattice mismatch is compensated for by the formation of interfacial misfit dislocations which do not propagate into the bonded films [155]. Wafer bonding is currently being used successfully in industry. Hewlett Packard has utilized this technique in the fabrication of super-bright AlInGaP double heterostructure LEDs by chemically removing the absorbing GaAs substrates and wafer bonding the devices to GaP (larger bandgap) transparent substrates [157,158]. The growth of high quality AlGaP on GaP substrates has been achieved [159] and through the use of wafer bonding and a properly chosen etch to selectively remove the GaP substrate [160], a mechanically strong thermally stable AlGaP/Si structure with low defect densities is potentially feasible.

REFERENCES

1. F. Shimuar, Semiconductor Silicon Crystal Technology, (Academic Press, Inc., New York, 1989).
2. T. Nishimura, K. Kadoiwa, M. Miyashita, H. Kumabe and Murotani, 112, 791 (1991).
3. N. Noto, S. Nozaki, T. Egawa, T. Soga, T. Jimbo and M. Umeno, (Materials Research Society, San Francisco 1989) 247 .
4. T. George, E. R. Weber, S. Nozaki, A. T. Wu, N. Noto and M. Umeno, J. Appl. Phys. 67, 2441 (1990).
5. T. E. Zipperian and L. R. Dawson, J. Appl. Phys. 54, 6019 (1983).
6. M. Kumagai, T. Takagahara and E. Hanamura, Phys. Rev. B 37, 898 (1988).
7. H. C. Casey and M. B. Panish, Heterostructure Lasers, (Academic Press, Orlando, FL, 1978).
8. G. B. Stringfellow, J. Cryst. Growth 58, 194 (1982).
9. K. J. Bachmann, N. Dietz, A. E. Miller, D. Venables and J. T. Kelliher, J. Vac. Sci. Technol. A 13, 696 (1995).
10. E. Bauer, Z. Kristallogr. 110, 423 (1958).
11. E. Bauer and H. Poppa, Thin Solid Films 12, 167 (1972).
12. I. Markov and S. Stoyanov, Contemp. Phys. 28, 267 (1987).
13. R. W. Vook, Intern. Metals Rev. 27, 209 (1982).
14. I. Markov and R. Kaischew, Thin Solid Films 32, 163 (1976).
15. J. H. v. d. Merwe, in Chemistry and Physics of Solid Surfaces V, edited by R. Vanselow and R. Howe (Springer-Verlag, New York, 1984), p. 365.
16. R. Bruinsma and A. Zangwill, Europhys. Lett. 4, 729 (1987).
17. M. H. Grabow and G. H. Gilmer, Initial Stages of Epitaxial Growth (Materials Research Society, Anaheim, CA 1987) 15 .
18. M. H. Grabow and G. H. Gilmer, Surf. Sci. 194, 333 (1988).
19. B. G. Orr, D. Kessler, C. W. Snyder and L. Sander, Europhys. Lett. 19, 33 (1992).

20. C. W. Snyder, J. F. Mansfield and B. G. Orr, Phys. Rev. B 46, 9551 (1992).
21. M. Kitamura, M. Nishioka, J. Oshinowo and Y. Arakawa, Appl. Phys. Lett. 66, 3663 (1995).
22. F. C. Frank and J. H. v. d. Merwe, Proc. Roy. Soc. Lon. Ser. A 198, 205 (1949).
23. F. C. Frank and J. H. v. d. Merwe, Proc. Roy. Soc. Lon. Ser. A 198, 216 (1949).
24. S. Guha, H. MuneKata, F. K. LeGoues and L. L. Chang, Appl. Phys. Lett. 60, 3220 (1992).
25. K. Kitahara, M. Ozeki and K. Nakajima, Jpn. J. Appl. Phys. 32, 1051 (1993).
26. M. Tachikawa and H. Mori, Appl. Phys. Lett. 56, 2225 (1990).
27. P. S. Peercy, E. G. Bauer, B. W. Dodson, D. J. Ehrlich, L. C. Feldman, C. P. Flynn, M. W. Geis, H. J.P, R. J. Matyi, P. M. Petroff, J. M. Phillips, G. B. Stringfellow and A. Zangwill, J. Mater. Res. 5, 852 (1990).
28. D. K. Biegelsen, F. A. Ponce, A. J. Smith and J. C. Tramontana, Heteropitaxy on Silicon (Material Research Society, Palo Alto, CA 1986) 45 .
29. T. Soga, T. George, T. Jimbo and M. Umeno, Jpn. J. Appl. Phys. 30, 3471 (1991).
30. M. Yamaguchi, T. Nishioka and M. Sugo, Appl. Phys. Lett. 54, 24 (1989).
31. T. Y. Chiang, E. H. Liu and T. R. Yew, J. Cryst. Growth 135, 469 (1994).
32. N. Ohtsuka, K. Kitahara, M. Ozeki and K. Kodama, J. Cryst. Growth 99, 346 (1990).
33. A. Georgakilas, P. Panayotatos, J. Stoemenos, J. L. Mourrain and A. Christou, J. Appl. Phys. 71, 2679 (1992).
34. A. E. Blakeslee, M. M. Al-Jassim and S. E. Asher, Heteroepitaxy on Silicon II (Materials Research Society, 1987) 105 .
35. Y. Kohama, Y. Kadota and Y. Ohmachi, Jpn. J. Appl. Phys. 29, L229 (1990).
36. W. G. Bi, X. B. Mei and C. W. Tu, To be published in J. Cryst. Growth (1996).
37. R. D. Bringans, M. A. Olmstead, R. I. G. Uhrberg and R. Z. Bachrach, Initial Stages of Epitaxial Growth (Materials Research Society, Anaheim, CA 1987) 201 .
38. E. A. Fitzgerald, J. M. Kuo, Y. H. Xie and P. J. Silverman, Appl. Phys. Lett. 64, 733 (1994).
39. T. Egawa, T. Jimbo and M. Umeno, Appl. Phys. Lett. 61, 2923 (1992).
40. T. Soga, T. George, T. Jimbo, M. Umeno and E. R. Weber, Appl. Phys. Lett. 58, 1170 (1991).
41. K. Kitahara, N. Ohtsuka and M. Ozeki, J. Vac. Sci. Technol. B 7, 700 (1989).

42. T. Egawa, Y. Kobayashi, Y. Hayashi, T. Soga, T. Jimbo and M. Umeno, *Jpn. J. Appl. Phys.* 29, L1133 (1990).
43. K. Ozasa, M. Yuri and H. Matsunami, *J. Cryst. Growth* 102, 31 (1990).
44. M. Yoshimoto, K. Ozasa, T. Tsuji, A. Kajimoto and H. Matsunami, *J. Cryst. Growth* 115, 265 (1991).
45. J. N. Baillargeon, K. Y. Cheng and K. C. Hsieh, *J. Cryst. Growth* 105, 106 (1990).
46. H. Asahi, M. Enokida, K. Asami, J. H. Kim, T. Watanabe, R. K. Soni and S. Gonda, *J. Cryst. Growth* 136, 268 (1994).
47. X.-L. Wang, A. Wakahara and A. Sasaki, *J. Appl. Phys.* 76, 524 (1994).
48. C. R. Abernathy, S. J. Pearton, R. Caruso, F. Ren and J. Koválchik, *Appl. Phys. Lett.* 55, 1750 (1989).
49. W. T. Tsang, *J. Cryst. Growth* 81, 261 (1987).
50. C. R. Abernathy, *Mat. Sci. Eng. R* 14, 203 (1995).
51. A. Robertson, Jr., T. H. Chiu, W. T. Tsang and J. E. Cunningham, *J. Appl. Phys.* 64, 877 (1988).
52. T. Martin and C. R. Whitehouse, *J. Cryst. Growth* 105, 57 (1990).
53. M. B. Panish and R. A. Hamm, *J. Cryst. Growth* 78, 445 (1986).
54. Y.-M. Houg, *Crit. Rev. Solid State Mater. Sci.* 17, 277 (1992).
55. C. R. Abernathy and P. W. Wisk, *Solid-State Electronics* 38, 737 (1995).
56. C. R. Abernathy, S. J. Pearton, D. A. Bohling and G. T. Muhr, *J. Cryst. Growth* 111, 574 (1991).
57. K. M. Chen, T. Castro, A. Franciosi, W. L. Gladfelter and P. I. Cohen, *Appl. Phys. Lett.* 60, 2132 (1992).
58. Y. M. Houg, *J. Cryst. Growth* 105, 124 (1990).
59. C. R. Abernathy, S. J. Pearton, F. A. Baiocchi, T. Ambrose, A. S. Jordan, D. A. Bohling and G. T. Muhr, *J. Cryst. Growth* 110, 457 (1991).
60. J. C. Garcia, P. Maurel, P. Bove and J. P. Hirtz, *J. Appl. Phys.* 69, 3297 (1991).
61. A. Wakahara, X. Wang and A. Sasaki, *J. Cryst. Growth* 124, 118 (1992).
62. D. S. Katzer and B. V. Shanabrook, *J. Vac. Sci. Technol. B* 11, 1003 (1993).
63. M. Nouaoura, L. Lassabatere, N. Bertru, J. Bonnet and A. Ismail, *J. Vac. Sci. Technol. B* 13, 83 (1995).

64. S. Guha, Ph.D. thesis, University of Southern California, 1991.
65. G. Binning, H. Rohrer, C. Gerber and E. Weibel, *Phys. Rev. Lett.* **49**, 57 (1982).
66. M. Liehr, *Chemical Surface Preparation, Passivation and Cleaning for Semiconductor Growth and Processing* (Materials Research Society, San Francisco 1992) 3.
67. J. A. Sees and L. H. Hall, *J. Electrochem. Soc.* **142**, 1238 (1995).
68. W. Kern, *RCA Rev.* **31**, 187 (1970).
69. W. Kern, *J. Electrochem. Soc.* **137**, 1887 (1990).
70. S. Verhaverbeke, J. Alay, P. Mertens, M. Meuris, M. Heyns, W. Vandervorst, M. Murrell and C. Sofield, *Chemical surface preparation, passivation and cleaning for semiconductor growth and processing* (Materials Research Society, San Francisco 1992) 391 .
71. S. S. Iyer, M. Arienzo and E. d. Frésart, *Appl. Phys. Lett.* **57**, 893 (1990).
72. H. Mori, M. Tachikawa, M. Sugo and Y. Itoh, *Appl. Phys. Lett.* **63**, 1963 (1993).
73. S. Verhaverbeke, I. Teerlinck, C. Vinckier, G. Stevens, R. Cartuyvels and M. M. Heyns, *J. Electrochem. Soc.* **141**, 2852 (1994).
74. G. W. Trucks, K. Raghavachari, G. S. Higashi and Y. J. Chabal, *Phys. Rev. Lett.* **65**, 504 (1990).
75. V. A. Burrows, Y. J. Chabal, G. S. Higashi, K. Raghavachari and S. B. Christman, *Appl. Phys. Lett.* **53**, 998 (1988).
76. Y. J. Chabal, G. S. Higashi and K. Raghavachari, *J. Vac. Sci. Technol. A* **7**, 2104 (1989).
77. G. F. Cerofolini and L. Meda, *Appl. Surf. Sci.* **89**, 351 (1995).
78. C. H. Bjorkman, J. L. Alay, H. Nishimura, M. Fukuda, T. Yamazaki and M. Hirose, *Appl. Phys. Lett.* **67**, 2049 (1995).
79. Y. J. Chabal, *Chemical Surface Preparation, Passivation, and Cleaning for Semiconductor Growth and Processing* (Materials Research Society, San Francisco 1992) 349 .
80. S. F. Fang, A. Salvador and H. Morkoc, *Appl. Phys. Lett.* **58**, 1887 (1991).
81. M. Miyamoto, N. Kita, S. Ishida and T. Tatsuno, *J. Electrochem. Soc.* **141**, 2899 (1994).
82. K. K. Ko and S. W. Pang, *J. Electrochem. Soc.* **141**, 255 (1994).
83. Y. Z. Hu, P. P. Buaud, Y. Wang, L. Spanos and E. A. Irene, *Appl. Phys. Lett.* **64**, 1233 (1994).
84. T.-R. Yew and R. Reif, *Evolution of Thin-Film and Surface Microstructure* (Materials Research Society, Boston 1990) 401 .

85. L. Suemune, Y. Kunitsugu, Y. Kan and M. Yamanishi, Appl. Phys. Lett. 55, 760 (1989).
86. T. Shibata, Y. Nanishi and M. Fujimoto, Jpn. J. Apl. Phys. 29, L1181 (1990).
87. M. Delfino, S. Salimian, D. Hodul, A. Ellingboe and W. Tsai, J. Appl. Phys. 71, 1001 (1992).
88. W. Tsai, M. Delfino, M. E. Day, T. Sheng, B. C. Chung and S. Salimian, J. Vac. Sci. Technol. A 11, 2525 (1993).
89. P. J. Grunthaner, F. J. Grunthaner, R. W. Fathauer, T. L. Lin, M. H. Hecht, L. D. Bell, W. J. Kaiser, F. D. Schowengerdt and J. H. Mazur, Thin Solid Films 183, 197 (1989).
90. H. Mori and M. Tachikawa, J. Cryst. Growth 143, 349 (1994).
91. J.M. Grant and L.R. Allen, USA Microscopy and Analysis 12, 5 (1995).
92. B. S. Meyerson, Sci. Am. 270, 62 (1994).
93. T. S. Rao, K. Nozawa and Y. Horikoshi, Appl. Phys. Lett. 60, 1606 (1992).
94. E. Yablonovitch, D. L. Allara, C. C. Chang, T. Gmitter and T. B. Bright, Phys. Rev. Lett. 57, 249 (1986).
95. L. Li, H. Bender, T. Trenkler, P. W. Mertens, M. Meuris, W. Vandervorst and M. M. Heyns, J. Appl. Phys. 77, 1323 (1995).
96. D. Gräf, M. Brohl, S. Bauer-Mayer, A. Ehlert, P. Wagner and A. Schnegg, Surface Chemical Cleaning and Passivation for Semiconductor Processing (Materials Research Society, San Francisco, CA 1993) 23 .
97. M. Miyashita, T. Tusga, K. Makiyara and T. Ohmi, J. Electrochem. Soc. 139, 2133 (1992).
98. T. Takahagi, I. Nagai, A. Ishitani, H. Kuroda and Y. Nagasawa, J. Appl. Phys. 64, 3516 (1988).
99. F. Ernst and P. Pirouz, J. Mater. Res. 4, 834 (1989).
100. C. Galewski, J.-C. Lou and W. G. Oldham, IEEE Trans. Semicond. Manufact. 3, 93 (1990).
101. A. Ponchet, A. L. Corre, H. L'Haridon, B. Lambert and S. Salaün, Appl. Phys. Lett. 67, 1850 (1995).
102. E. Yoon and R. Reif, Evolution of thin-film and surface microstructure (Materials Research Society, Boston 1990) 37 .
103. D. Leonard, K. Pond and P. M. Petroff, Phys. Rev. B 50, 11687 (1994).
104. B. R. Bennett, R. Magno and B. V. Shanabrook, Appl. Phys. Lett. 68, 505 (1996).
105. J. B. Hudson, Surface Science An Introduction, (Butterworth-Heinemann, Boston, 1992).

106. P. W. Voorhees, J. Stat. Phys. 38, 231 (1985).
107. M. Krishnamurthy, J. Drucker and J. A. Venables, J. Appl. Phys. 69, 6461 (1991).
108. J. Drucker, Phys. Rev. B 48, 18203 (1993).
109. L. Pauling, The Nature of the Chemical Bond, 3rd (Cornell University Press, Ithaca, NY, 1960).
110. R. T. Sanderson, Chemical Bonds and Bond Energy, (Academic Press, New York, 1971).
111. B. J. Lee, Y. M. Houn, J. N. Miller and J. E. Turner, J. Cryst. Growth 105, 168 (1990).
112. C. R. Abernathy, D. A. Bohling and A. C. Jones, Materials Research Society Symposium Proceedings (Materials Research Society, San Francisco 1992) 3.
113. T. T. Cheng, M. Aindow, I. P. Jones, J. E. Hails and D. J. Williams, J. Crystal Growth 154, 251 (1995).
114. A. P. Mills and H.-J. Gossmann, J. Appl. Phys. 78, 5830 (1995).
115. Y. Wang, X. Chen and R. J. Hamers, Phys. Rev. B 50, 4534 (1994).
116. J. E. Palmer, G. Burns, C. G. Fonstad and C. V. Thompson, Appl. Phys. Lett. 55, 990 (1989).
117. T. H. Chiu, J. E. Cunningham and A. Robertson, Jr., J. Cryst. Growth 95, 136 (1989).
118. M. Imaizumi, T. Saka, T. Jimbo, T. Soga and M. Umeno, Jpn. J. Appl. Phys. 30, 451 (1991).
119. T. P. Chin, B. W. Liang, H. Q. Hou, M. C. Ho, C. E. Chang and C. W. Tu, Appl. Phys. Lett. 58, 254 (1991).
120. N. Grandjean and J. Massies, Semicond. Sci. Technol. 8, 2031 (1993).
121. W. G. Morris, in The Encyclopedia of Advanced Materials, edited by D. Bloor, R. J. Brook, M. C. Flemings and S. Mahajan (Pergamon Press, Oxford, 1994), p. 136.
122. R. People and J. C. Bean, Appl. Phys. Lett. 47, 322 (1985).
123. V. Alberts, J. Cryst. Growth 140, 299 (1994).
124. M. Akiyama, Y. Kawarada, S. Nishi, T. Ueda and K. Kaminishi, Heteroepitaxy on Silicon (Materials Research Society, Palo Alto, CA 1986) 53.
125. J. M. Olson, M. M. Al-Jassim, A. Kibbler and K. M. Jones, J. Crystal Growth 77, 515 (1986).
126. D. Gerthsen, Philos. Mag. A 67, 1365 (1993).

127. Y. R. Xing, R. W. Devenish, T. B. F. Joyce, C. J. Kiely, T. J. Bullough and P. J. Goodhew, *Appl. Phys. Lett.* 60, 616 (1992).
128. P. M. J. Marée, J. C. Barbour, J. F. v. d. Veen, K. L. Kavanagh, C. W. T. Bulle-Lieuwma and M. P. A. Vieggers, *J. Appl. Phys.* 62, 4413 (1987).
129. K. V. Ravi, Imperfections and Impurities in Semiconductor Silicon, (John Wiley & Sons, New York, 1981).
130. S. Guha, A. Madhukar and K. C. Rajkumar, *Appl. Phys. Lett.* 57, 2110 (1990).
131. G. C. Hua, D. C. Grillo, T. B. Ng, C. C. Chu, J. Han, R. L. Gunshor and A. V. Nurmikko, *J. Electron. Mater.* 25, 263 (1996).
132. E. D. Bourret-Courchesne, *Appl. Phys. Lett.* 68, 1675 (1996).
133. F. Ernst and P. Pirouz, *J. Appl. Phys.* 64, 4526 (1988).
134. T. Soga, H. Nishikawa, T. Jimbo and M. Umeno, *Jpn. J. Appl. Phys.* 32, 4912 (1993).
135. J. Taftø and J. C. H. Spence, *J. Appl. Cryst.* 15, 60 (1982).
136. R. Fischer, N. Chand, W. Kopp, H. Morkoc, L. P. Erickson and R. Youngman, *Appl. Phys. Lett.* 47, 397 (1985).
137. P. M. Petroff, *J. Vac. Sci. Technol. B* 4, 874 (1986).
138. Y. Chen, X. W. Lin, Z. Liliental-Weber, J. Washburn, J. F. Klem and J. Y. Tsao, *Appl. Phys. Lett.* 68, 111 (1996).
139. S. V. Ghaisas and A. Madhukar, *J. Vac. Sci. Technol.* B7, 264 (1989).
140. N. Otsuka, Y. N. C. Choi, S. Nagakura, R. Fischer, C.K. Peng and H. Morkoe, *Heteroepitaxy on Silicon* (Materials Research Society, Palo Alto, CA 1986) 85 .
141. X. L. Wei and M. Aindow, *Appl. Phys. Lett.* 65, 1903 (1994).
142. T. J. Gosling, *J. Appl. Phys.* 74, 5415 (1993).
143. G. Bremond, H. Said, T. Benyattou, G. Guillot, J. Meddeb, M. Pitaval, N. Draidia and R. Azoulay, B9, 143 (1991).
144. D. C. Tu (private communication).
145. R. D. Bringans, M. A. Olmstead, F. A. Ponce, D. K. Biegelsen, B. S. Krusor and R. D. Yingling, *J. Appl. Phys.* 64, 3472 (1988).
146. K. Kadoiwa, T. Nishimura, N. Hayafuji, M. Miyashita, H. Kizuki and K. Mizuguchi, *J. Cryst. Growth* 115, 128 (1991).
147. K. Fujita, Y. Shiba and K. Asai, 107, 473 (1991).
148. J. N. Baillargeon, K. Y. Cheng and K. C. Hsieh, *Appl. Phys. Lett.* 56, 2201 (1990).

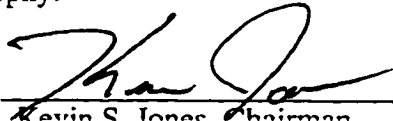
- 149. H. J. Osten, Appl. Phys. Lett. 64, 2356 (1994).
- 150. R. M. Tromp and M. C. Reuter, Phys. Rev. Lett. 68, 954 (1992).
- 151. M. Copel, M. C. Reuter, E. Kaxiras and R. M. Tromp, Phys. Rev. Lett. 63, 632 (1989).
- 152. M. Grundmann, J. Christen, N. N. Ledentsov, J. Böhrer, D. Bimberg, S. S. Ruvimov, P. Werner, U. Richter, U. Gösele, J. Heydenreich, V. M. Ustinov, A. Y. Egorov, A. E. Zhukov, P. S. Kop'ev and Z. I. Alferov, Phys. Rev. Lett. 74, 4043 (1995).
- 153. M. Yamaguchi, J. Mater. Res. 6, 376 (1991).
- 154. A. Salvador, F. Huang, B. Sverdlov, A. E. Botchkarev and H. Morkoc, Electron. Lett. 30, 1527 (1994).
- 155. F. E. Ejeckam, C. L. Chus, Z. H. Zhu, Y. H. Lo, M. Hong and R. Bhat, Appl. Phys. Lett. 67, 3936 (1995).
- 156. Y. H. Lo, R. Bhat, D. M. Hwang, C. Chua and C.-H. Lin, Appl. Phys. Lett. 62, 1038 (1993).
- 157. R.A. Metzger, Compound Semiconductors 2, 22 (1996).
- 158. F. A. Kish, F. M. Steranka, D. C. DeFever, D. A. Vanderwater, K. G. Park, C. P. Kuo, T. D. Osentowski, M. J. Peanasky, J. G. Yu, R. M. Fletcher, D. A. Steigerwald, M. G. Craford and V. M. Robbins, Appl. Phys. Lett. 64, 2839 (1994).
- 159. K. Adomi, N. Noto, A. Nakamura and T. Takenaka, J. Cryst. Growth 124, 570 (1992).
- 160. J. W. Lee, C. J. Santana, C. R. Abernathy and S. J. Pearton, J. Electrochem. Soc. 143, L1 (1996).

BIOGRAPHICAL SKETCH

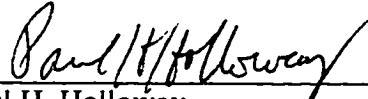
Christopher Joseph Santana was born on August 8, 1967, in Oakland, California. He attended schools in California, Taiwan, and Virginia and graduated from James Madison High School in Vienna, Virginia, in 1985. After two years of education at George Mason University in Fairfax, Virginia, he transferred to the University of Florida to pursue an undergraduate degree in materials science. In May 1990, he graduated with honors from the University of Florida with a Bachelor of Science in Engineering degree in the field of materials science and engineering. He then entered into the graduate school program at the University of Florida in May of 1990 to begin his studies for a master's degree in the Department of Materials Science and Engineering. In December 1992, he completed his thesis entitled "Characterization of Hot Pressed Polycrystalline Silicon Wafers Produced from Waste Silicon Powder for the Application of Solar Cells".

He is a member of the Materials Research Society, the American Solar Energy Society, the American Vacuum Society, Alpha Sigma Mu and several environmental organizations.

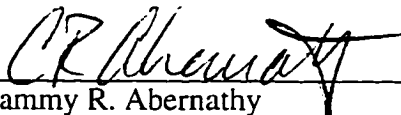
I certify that I have read this study and that in my opinion it conforms to acceptable standards of scholarly presentation and is fully adequate, in scope and quality, as a dissertation for the degree of Doctor of Philosophy.


Kevin S. Jones, Chairman
Associate Professor of Materials
Science and Engineering


I certify that I have read this study and that in my opinion it conforms to acceptable standards of scholarly presentation and is fully adequate, in scope and quality, as a dissertation for the degree of Doctor of Philosophy.


Paul H. Holloway
Professor of Materials
Science and Engineering


I certify that I have read this study and that in my opinion it conforms to acceptable standards of scholarly presentation and is fully adequate, in scope and quality, as a dissertation for the degree of Doctor of Philosophy.


Cammy R. Abernathy
Professor of Materials
Science and Engineering

I certify that I have read this study and that in my opinion it conforms to acceptable standards of scholarly presentation and is fully adequate, in scope and quality, as a dissertation for the degree of Doctor of Philosophy.



Steve J. Pearton
Professor of Materials
Science and Engineering

I certify that I have read this study and that in my opinion it conforms to acceptable standards of scholarly presentation and is fully adequate, in scope and quality, as a dissertation for the degree of Doctor of Philosophy.

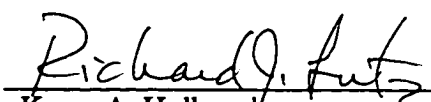

Tim Anderson
Professor of Chemical Engineering

This thesis was submitted to the Graduate Faculty of the College of Engineering and to the Graduate School and was accepted as partial fulfillment of the requirements for the degree of Doctor of Philosophy.

May, 1996



Winfred M. Phillips
Dean, College of Engineering



Karen A. Holbrook
Dean, Graduate School